

FIELD OF SCIENCE: ENGINEERING AND TECHNOLOGY

DISCIPLINE OF SCIENCE: automation, electronics, electrical engineering and space technologies

## **DOCTORAL DISSERTATION**

# Evaluation and control of electromagnetic field exposure from multiantenna systems

Mgr inż. Marcin Rybakowski

Supervisor: dr hab. inż. Paweł Kabacik, prof. uczelni

Keywords: 5G, 6G, actual maximum approach, antenna array, electromagnetic field exposure, beamforming, cellular networks, wireless communication

WROCŁAW 2025

### **Abstract**

Massive MIMO technology is a key enabler for 5G and future generations of wireless communication standards. Base stations equipped with multiantenna systems, capable of spatial multiplexing and beamforming, significantly enhance capacity and coverage. These systems also facilitate the introduction of higher frequency bands in cellular communications by enabling the construction of large antenna arrays that compensate for increased propagation losses.

However, the use of large multiantenna systems presents challenges in evaluating, controlling, and measuring electromagnetic field exposure. The high gain of these arrays can lead to overly conservative compliance assessments based on maximum radiated power, resulting in significantly overestimated distances. Recognizing this issue, the International Electrotechnical Commission developed the actual maximum approach available in IEC 62232 for compliance assessment of multiantenna systems. This approach considers the dynamic nature of beamforming, leading to significantly lower compliance distances.

Accurate evaluation of Massive MIMO systems in terms of EMF exposure and the application of the actual maximum approach require comprehensive research studies considering various factors that influence compliance assessment accuracy. This dissertation aims to evaluate EMF exposure from multiantenna systems in realistic environments. New models and studies, based on more realistic assumptions, have been developed and validated under practical system operating conditions. These studies incorporate diverse parameter distributions, including terminal distribution, real-world radio frequency propagation scenarios, and different beamforming techniques.

This research makes several novel contributions:

- **Moving Terminal Model:** This dissertation introduces a model for moving terminals, a first in the field, to accurately assess EMF exposure in dynamic environments.
- **Beamforming Algorithm Impact:** The impact of different beamforming algorithms on actual EMF exposure is investigated in detail.
- Extreme Massive MIMO Evaluation: Extreme Massive MIMO arrays are evaluated in the context of new frequency bands and the emerging 6G standard.
- **Novel RF Emission Control Methods:** New RF emission control methods, specifically designed for implementation in Massive MIMO base stations, are developed. These methods utilize novel beamforming algorithms, offering an alternative to existing transmit power control methods.

The research findings have been published in peer-reviewed journals and conference proceedings. Moreover, the research outcomes are referenced in the IEC technical report (IEC 62269), providing guidelines for operators of Massive MIMO systems using the actual maximum approach. Feasibility studies will be conducted to evaluate the practical implementation of new beamforming algorithms in base stations.

### Streszczenie

Technologia *Massive MIMO* jest kluczową technologią standardu 5G i przyszłych generacji standardów telekomunikacji bezprzewodowej. Stacje bazowe wyposażone w systemy wieloantenowe, zdolne do multipleksacji przestrzennej i kształtowania wiązki, znacznie zwiększają przepustowość i zasięg. Systemy te ułatwiają również wprowadzenie wyższych pasm częstotliwości w komunikacji komórkowej, umożliwiając budowę dużych ukladów antenowych, które kompensują zwiększone straty propagacyjne.

Jednak korzystanie z dużych systemów wieloantenowych stwarza wyzwania w zakresie oceny, kontroli i pomiaru ekspozycji na pole elektromagnetyczne. Wysoki zysk tych anten może prowadzić do zbyt konserwatywnych ocen zgodności opartych na maksymalnej mocy promieniowania, co skutkuje znacznie zawyżonymi odległościami. Międzynarodowa Komisja Elektrotechniczna (*International Electrotechnical Commission*) opracowała nową metodę ewaluacji zawartą w standardzie IEC 62232 dla systemów wieloantenowych. Podejście to uwzględnia dynamiczny charakter kształtowania wiązki, prowadząc do znacznie niższych bezpiecznych odległości od stacji bazowych.

Dokładna ocena systemów *Massive MIMO* pod względem ekspozycji na pola elektromagnetyczne i zastosowanie nowej metody ewaluacji wymaga kompleksowych badań uwzględniających różne czynniki wpływające na dokładność oceny. Niniejsza rozprawa doktorska ma na celu ocenę ekspozycji na pola elektromagnetyczne generowane przez systemy wieloantenowe w rzeczywistych warunkach. Nowe modele i badania, oparte na bardziej realistycznych założeniach, zostały opracowane i zweryfikowane w praktycznych warunkach pracy systemu. Badania te obejmują różne rozkłady parametrów, w tym rozkład terminali, rzeczywiste scenariusze propagacji częstotliwości radiowych i różne techniki kształtowania wiązki.

Badania te wnoszą kilka nowych rozwiązań:

- **Model ruchomego terminala:** Niniejsza rozprawa doktorska wprowadza model ruchomych terminali, pierwszy w tej dziedzinie, w celu dokładnej oceny narażenia na pola elektromagnetyczne w dynamicznych środowiskach.
- **Wpływ algorytmu kształtowania wiązki**: Szczegółowo zbadano wpływ różnych algorytmów kształtowania wiązki na rzeczywistą ekspozycję na pola elektromagnetyczne.
- Ocena parametrów działania *Extreme Massive MIMO*: Macierze *Extreme Massive MIMO* są oceniane w kontekście nowych pasm częstotliwości i powstającego standardu 6G.
- Nowe metody kontroli natężenia i charakteru promieniowania RF: Opracowano nowe metody kontroli promieniowania RF, zaprojektowane specjalnie do implementacji w stacjach bazowych *Massive MIMO*. Metody te wykorzystują nowe algorytmy kształtowania wiązki, oferując alternatywę dla istniejących metod kontroli mocy nadawania.

Wyniki moich badań przedstawianych w tej rozprawie, zostały opublikowane w recenzowanych czasopismach i materiałach konferencyjnych. Poinadto wyniki badań zostały wymienione w raporcie technicznym IEC 62269, zawierającym wytyczne dla operatorów systemów *Massive MIMO* wykorzystujących nową metodę ewaluacji. Przeprowadzone zostaną studia wykonalności w celu oceny praktycznego wdrożenia nowych algorytmów kształtowania wiązki w stacjach bazowych.

## Acknowledgments

I would like to express my sincere gratitude to the many individuals who contributed to the successful completion of my dissertation research.

First and foremost, I am deeply indebted to my dissertation supervisor, dr hab. inż Pawel Kabacik, prof. uczelni for his support, invaluable guidance, and the extensive assistance he provided throughout my PhD journey.

I extend my heartfelt thanks to Christoph Grangeat who was my thesis supervisor within the company and initiated the topic of my thesis. His insightful comments, stimulating discussions, and collaborative efforts on our publications were instrumental in shaping my research.

I am also extremely grateful to the members of our EMF team at Nokia. I particularly appreciate Kamil Bechta for his valuable discussions on beamforming algorithms and his assistance with publications. My thanks also go to Azra Zejnilagic for her insightful comments and contributions to our articles. I would like to acknowledge the contributions of Piotr Szlosarczyk and Wojciech Silko, who provided essential support with the measurements conducted in the anechoic chamber.

A special thanks are to Andreas Weber for his invaluable assistance with the system level simulations.

Finally, and most importantly, I would like to express my deepest gratitude to my Family, especially my wife Anna. Your unwavering patience and understanding were essential in enabling me to accomplish that Doctoral Dissertation.

## Contents

Al	ostract		1
St	reszcze	nie	2
A	cknowle	edgments	3
Li	st of ac	ronyms and abbreviations	7
1.	Intro	duction	9
	1.1	Motivation	9
	1.2	Multiantenna systems and beamforming	10
	1.3	Primary aspects of electromagnetic field exposure from multiantenna systems	15
	1.4	Actual EMF exposure from Massive MIMO base station	16
	1.5	Research focus and objectives	19
	1.6	Organizations of the thesis	20
2.	Mod	elling of actual electromagnetic field exposure from multiantenna systems	22
	2.1	Introduction to problem of evaluation of EMF exposure from multiantenna systems	22
	2.2	System level simulator of Massive MIMO and EMF exposure	23
	2.3	Beamforming algorithms	29
	2.4	Radio wave propagation and channel modeling	31
	2.5	Statistical analysis of EMF exposure from beamforming antennas	33
3.	Actu	al EMF exposure from multiantenna systems with 'Grid of Beam' beamforming	36
	3.1	Introduction	36
	3.1.1	The analysis of sectoral antennas	36
	3.1.1	.1 Sector antenna with MIMO 2x2	36
	3.1.1	.2 Sector antenna with MIMO 4x4	38
	3.2 operati	The evaluation of actual EMF exposure from various base stations configurations ng in sub-GHz band with GoB beamforming	40
	3.2.1	Simulation assumptions	40
	3.2.2	Simulation results and discussion	42
	3.3 frequer	The evaluation of actual EMF exposure from base station operating in millimeter wave acy band with GoB beamforming	47
	3.3.1	Introduction	47
	3.3.2	Simulation assumptions	47
	3.3.3	Simulation results and discussion	49
	3.4	Impact of averaging time on actual EMF exposure	50
	3.4.1	Introduction	50
	3.4.2	Impact of averaging time for actual EMF exposure in sub-GHz frequency band	51

	3.4.3	Impact of averaging time for actual EMF exposure in mmWave frequency band	53
	3.5	Conclusions	54
4		stical analysis of actual EMF exposure from Massive MIMO base stations serving	-
n	oving te		55
	4.1	Introduction	55
	4.2	Modeling of moving terminals	55
	4.3	Simulations assumptions	58
	4.4	Evaluation of actual electric field of serving and non-serving terminals	62
	4.5	Conclusions	65
5 st	. Impa tations	act of beamforming algorithms on the Actual EMF exposure from Massive MIMC	) base 66
	5.1	Introduction	66
	5.2	Simulation assumptions	68
	5.3	The performance of Massive MIMO with different beamforming algorithms	70
	5.4	The analysis of beamforming schemes impact on actual EMF exposure	73
	5.4.1	Impact of beamforming algorithm on actual EMF exposure	73
	5.4.2	Impact of number of transceivers on actual EMF exposure	76
	5.5	Summary and conclusions	77
6	. Eval	uation of the actual EMF exposure from Extreme Massive MIMO base stations	80
	6.1	Introduction to Extreme Massive MIMO for future wireless systems generations	80
	6.2	Simulation methodology	81
	6.3	The performance of Extreme Massive MIMO systems	83
	6.4	The analysis of actual EMF exposure form Extreme Massive MIMO	85
	6.5	The evaluation of actual electric field from Extreme Massive MIMO	89
	6.6	Conclusions	90
7	. The	experimental study of actual EMF exposure from Massive MIMO	91
	7.1	Objectives	91
	7.2	The measurement setup	91
	7.3	The use cases descriptions	93
	7.4	The analysis of actual EMF exposure for various use cases	94
	7.5	Summary	98
8		al RF emissions control for multiantenna systems with beamforming	99
	8.1	Introduction to EIRP control for actual EMF exposure	99
	8.2	The impact of various techniques of EIRP control for system performance	100
	8.3	The optimal beam broadening method for EIRP control in codebook-based beamform 104	ming

8.3.2	Principles of the effective antenna gain in real propagation environment	104			
8.3.2	Beam broadening algorithm for actual EIRP control	108			
8.3.3	Verification of beam broadening algorithm	110			
8.4	The selective EIRP control in spatial segments for advanced beamforming	115			
8.4.2	Introduction	115			
8.4.2	The method of selective actual EIRP control for advanced beamforming schemes	117			
8.4.3	3 Simulation results	121			
8.5	Summary and Conclusions	125			
9. Sum	mary	127			
9.1	Conclusions on research results	127			
9.2	Achievements	131			
9.3	Outlook for future research on electromagnetic field exposure in multiantenna system 134	ems			
10. References					

## List of acronyms and abbreviations

2D Two Dimensional2G Second Generation

32-Quadrature Amplitude Modulation

3D Three Dimensional3G Third Generation

3GPP 3rd Generation Partnership Project

4G Fourth Generation5G Fifth Generation

64QAM 64-Quadrature Amplitude Modulation

6G Sixth Generation ACK Acknowledge

ADC Analog to Digital Converter

AE Antenna Element

ASD Azimuth Spread of Departure

BCH Broadcast Channel
BF Beamforming
BS Base Station

CDF Cumulative Distribution Function

CSI Channel State Information
DAC Digital to Analog Converter

DL Downlink

EBF Eigenbeamforming

EIRP Equivalent Isotropically Radiated Power

eMBB Enhanced Mobile Broadband EMF Electromagnetic Field Exposure

EZF Eigenbeam Zero-Forcing
FDD Frequency Division Duplex

FR3 Frequency Range 3
GoB Grid of Beams

HARQ Hybrid Automatic Repeat Request

HPBW Half Power Beamwidth

ICNRIP International Commission on Non-Ionizing Radiation Protection

IEC International Electrotechnical Commission
IEEE Institute of Electrical and Electronics Engineers

ISAC Integrated Sensing and Communication

ISD Inter Site Distance

ITU International Telecommunication Union

KPI Key Performance Indicator

L2S Link to System LOS Line of Sight

LSP Large Scale Parameters MBB Mobile Broadband

MIB Master Information Block
MIMO Multiple Input Multiple Output

mMIMO Massive MIMO mmWave Millimeter Wave

MU-MIMO Multi User - Multiple Input Multiple Output

NACK Negative Acknowledgement

NLOS Non-Line of Sight O2I Outdoor to Indoor

OFDMA Orthogonal Frequency Division Multiple Access

PA Power Amplifier

PDSCH Physical Downlink Shared Channel

PF Proportional Fair

PMI Precoding Matrix Indicator
PRB Physical Resource Block
PSS Primary Synchronization Signal

RBW Resolution Bandwidth
RF Radio Frequency

RIS Reconfigurable Intelligent Surface

RMS Root Mean Square

SAR Specific Absorption Rate

SINR Signal to Interference and Noise Ratio

SLS System Level Simulation SNR Signal to Noise Ratio

SSB Synchronization Signal Block SSS Secondary Synchronization Signal

TDD Time Division Duplex

TDMA Time Division Multiplexing Access

TRX Transceiver
UE User Equipment

UL Uplink

ULLRC Ultra Reliable and Low Latency Communications

UMa Urban Macro UMi Urban Micro

WCDMA Wideband Code Division Multiple Access

WHO World Health Organization ZSD Zenith Spread of Departure

## 1. Introduction

### 1.1 Motivation

Wireless telecommunications systems have experienced tremendous progress in the last 30 years. Each successive generation of cellular systems has introduced new technologies, most of which have significantly increased the performance of the deployed cellular networks to meet ever-increasing coverage and capacity requirements [1]. The 2<sup>nd</sup> generation (2G) provided large coverage and enable mobile communication in most of the countries around the world. The 3<sup>rd</sup> generation (3G) introduced data communication and the era of smartphones. The 4<sup>th</sup> (4G) generation enhanced significantly the data communication with and introduced Mobile Broadband Communication services (MBB) on the level of cable and even fiber optics communication. We are now in the era of 5<sup>th</sup> generation (5G) of wireless communication generation which are deployed around the globe and perfected mobile data communication to extreme Mobile Broadband level (eMBB) and introduces new vertical use cases like ultra reliable and low latency communications (ULLRC).

The most important technology introduced by 5G is Massive Multiple Input Multiple Output (mMIMO) introduced by 3rd Generation Partnership Project (3GPP) standardization body to meet the ever-increasing demand for data throughput and coverage in cellular systems [2]. Equipping base station (BS) with large antenna array makes it possible to increase the spectral efficiency of a radio cell significantly, mainly through two complementary techniques: beamforming and spatial multiplexing [2][3]. Using beamforming, the BS concentrates the transmission energy toward a specific User Equipment (UE), which greatly increases the received signal power. With spatial multiplexing, multiple streams are sent by the BS to several active UEs, which are separated using an antenna beamforming algorithm. Due to the significant gains promised by multiantenna technologies, base stations equipped with dozens of antenna elements are deployed in 5G networks. These techniques are to be developed in the next generations of cellular systems even towards extremely large multiantenna systems where antenna systems will be built with hundreds or even thousands of antenna elements [3][4][5].

However, the use of complex antenna beamforming algorithms complicates how to assess and model electromagnetic field exposure from such systems [6]. Limiting electromagnetic field exposure (EMF) in modern mobile telecommunications systems, plays an increasingly important role. Previous EMF exposure assessment techniques for cellular systems with sectorized base stations, as specified by the International Electrotechnical Commission (IEC), employed simplified models that relied on the rated maximum radiated power [7]. These methods were overly conservative. It is necessary to provide more accurate methods for objective evaluation of EMF exposure when multiantenna MIMO systems with large antenna arrays and fast beam steering are used. The methods and regulations that have been developed so far have not yet been sufficiently studied in the dynamic operating environment of 5G and mMIMO systems, because the impact of the actual radio wave propagation channel and user distribution is not accurately included in a representative way for these scenarios. However, since the publication of IEC TR 62669:2019 [8] and IEC 62232:2022 [7], IEC methods now

incorporate the temporal and spatial variability of beams, providing a more accurate assessment of exposure levels.

The problems related to the assessment and control of electromagnetic field strength are now becoming central to the development of broadband wireless systems, which need to keep pace with the ever-increasing demands of the information society, while at the same time meeting the requirements of regulatory bodies in this area. The EMF exposure for mMIMO systems is new and very important area for research, industry but also for society. The academia's and industry are obligated to prove to society that that EMF exposure topic is very well understandable and that modern telecommunication systems which are deployed in unprecedented levels close to places with humans generate and can control radio frequency (RF) signals and hence electric field exposure meeting regulations. New applications and planned technologies for wireless telecommunication systems require research and the development of new techniques for the assessment and control of electromagnetic field strength already during their development.

The above challenges motivated me to research in this area. The purpose of this dissertation is to evaluate EMF exposure from multiantenna systems in a realistic environment. New models and studies based on more realistic assumptions have been developed and verified in practical system operating conditions. Different parameter distributions have been considered, such as the distribution of terminals, different real-world RF propagation scenarios and different types of beamforming. The novel electric field strength control techniques have been developed for multiantenna systems under the above assumptions. The proposed new electric field strength control techniques allow their implementation in modern base stations with embedded large antenna systems. My research focused on practical applications and challenges related to EMF exposure within industry and standardization contexts.

## 1.2 Multiantenna systems and beamforming

In the previous generation of cellular standards (2G, 3G and 4G) the sectorized antenna was mainly deployed especially in Urban Macro (UMa) environment. The sector antenna as shown on Figure 1-1 radiates electromagnetic wave in one direction to cover one sector of BS. The fixed beam with large beamwidth in azimuth is generated from the column antenna which consists of many antenna elements in vertical direction. The multiple antenna elements in vertical directions are added to increase antenna gain. The narrower beamwidth in elevation than in azimuth is desirable because User Equipment's are located much more widely in horizontal than in vertical direction. Sector antennas can be equipped with tilt mechanisms to enable the adjustment of beam direction in the elevation plane. Both mechanical and electrical tilt mechanisms are employed for radio network optimization, but they are not typically used in real-time network operations.

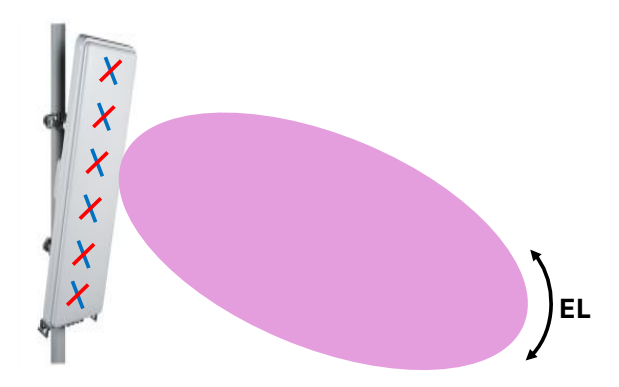


Figure 1-1 Sector antenna with fixed beam and electrical tilt in elevation.

In the 5G network multiantenna systems with mMIMO capability was introduced for the first time [2][3][9]. The mMIMO capable antenna system as depicted in Figure 1-2 can generate many independent beams and control their directions in wide range of azimuth and elevation angles.

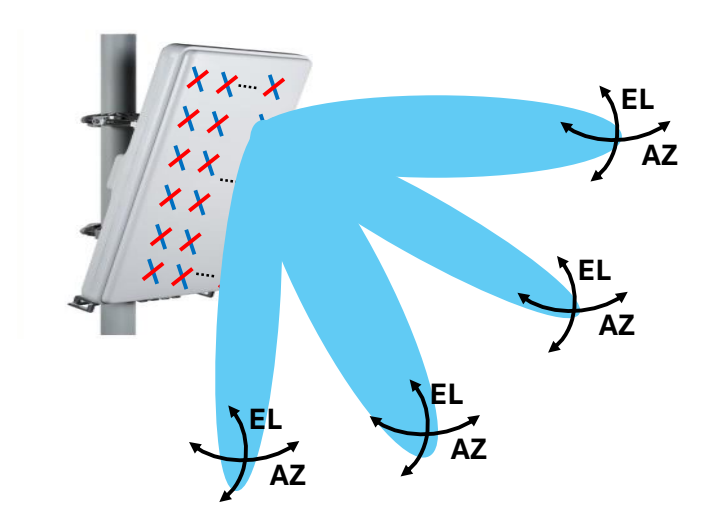


Figure 1-2 A generic drawing depicting principle of operation for Massive MIMO multiantenna in 5G base stations; capability of multi-beam generation by mMIMO antenna is shown for four beams example; each beam has capability to be steered in both elevation and azimuth planes.

By equipping BS with large antenna arrays, the spectral efficiency of a radio cell can be significantly enhanced. This improvement is primarily achieved through two complementary techniques: beamforming and spatial multiplexing. Beamforming enables the BS to focus transmit energy on a specific UE, resulting in a substantial increase in received signal power. Spatial multiplexing allows the BS to transmit multiple data streams to multiple active UEs simultaneously, with each stream separated by an antenna beamforming algorithm as shown on Figure 1-3.

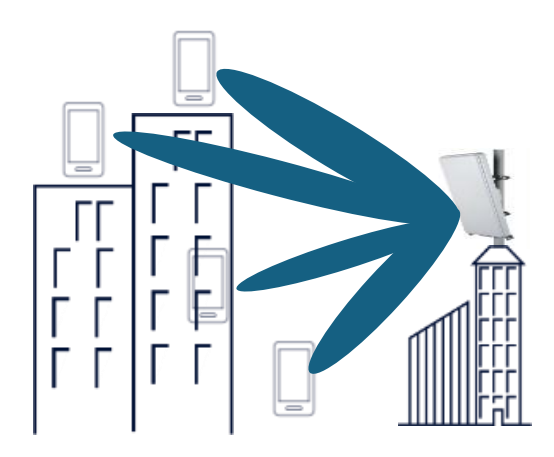


Figure 1-3 Illustration of massive MIMO principles: spatial (angular) separation of four UEs to provide multiplexing gain on orthogonal beams.

A limited beam pointing steering in the antenna array is possible to accomplish by implementing the phase shifter in front of each antenna element in the array, as shown in linear antenna array model with phase shifter in Figure 1-4. The application of the continuous regular phase shift between every antenna element results in delaying of wave radiation from one antenna element to other elements. This results in change of the slope of Equiphase wavefront where all independent electromagnetic waves are constructively summed. The ability to control the tilt of the wavefront causes changes in the direction of the resulting beam. When phase shift is performed in the digital domain of signals, many new technical capabilities open that are out of reach when use is made of analogue phase shifting. In particular, phase shift can be replaced by time domain and much broader bands of modulated signals can be processed by the antenna array.

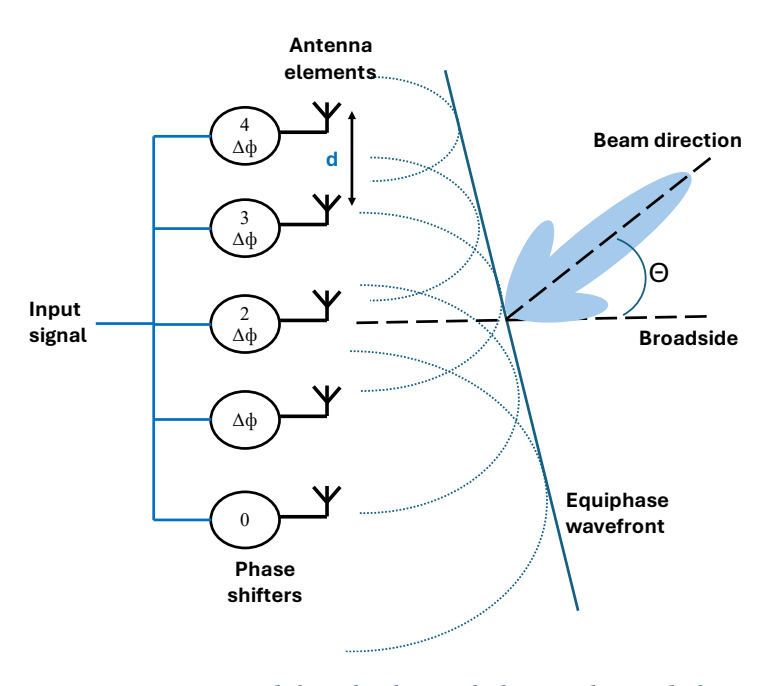


Figure 1-4 Linear antenna array model with phase shifters. Phase shifting is to be made with analogue circuits. However, 5G antenna technology makes use of digital signals inside for the purpose of phase control in arrays.

The practical architecture of antenna array in BS are shown on Figure 1-5 and Figure 1-6. In the Figure 1-5 the analog architecture is shown which is characterized by using analog phase shifters for every antenna element added typically before Power Amplifier (PA). This kind of phase shifter operates in analog domain so full bandwidth of system is affected by regulation of phase shifts. In this case the analog beamforming could change direction only for single beam at a time. If system needs to serve many UEs located in different directions, each UE is served using Time Domain Multiplexing Access (TDMA) where the beam changes directions at each time instance allocated to a specific UE.

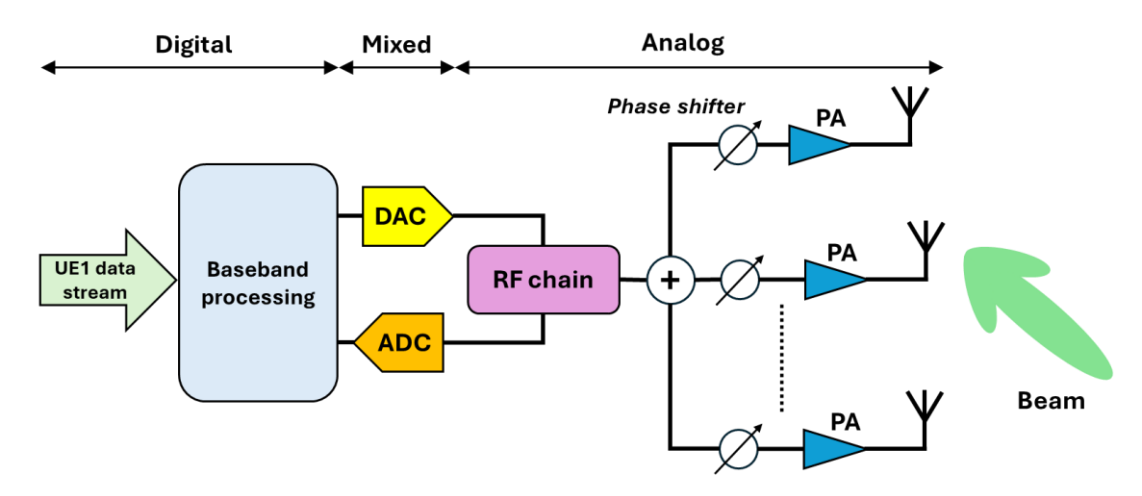


Figure 1-5 Analog beamforming architecture with a distributed power amplification (a major difference to long time used architecture with a single power amplifier).

Many independently controlled beams could be generated only using digital beamforming architecture shown on Figure 1-6. In this architecture we have digital phase shifters independently controlled for signal from each UE. The combined signal after conversion to analog domain is feeding the RF and antenna elements which emits the electromagnetic waves. The implementation phase shifters in digital domain provide many benefits:

- Data streams from each UE are controlled using different precoding weights,
- Frequency selective beamforming is possible which allow to use different beamforming weights for different part of spectrum,
- Digital beamforming makes it possible to use advanced precoding schemes adopted for different optimization criteria (maximizing the signal strength, minimizing interferences, improving multi UEs operations etc.).

The main drawback of digital architecture is significant power consumption due to application of separate transceivers (TRX) to every antenna element. Single TRX contains analog RF chain (transmitter and receiver parts) but also analog to digital (ADC) and digital to analog (DAC) converters. This impact power consumption of BS. In case of analog architecture, we have typically single TRX (per polarization) so power consumption is much lower. Mixed analog-digital (hybrid) architectures are possible and are characterized by better flexibility than analogue architecture and lower consumption than digital and could be used in some moderately demanding applications [3].

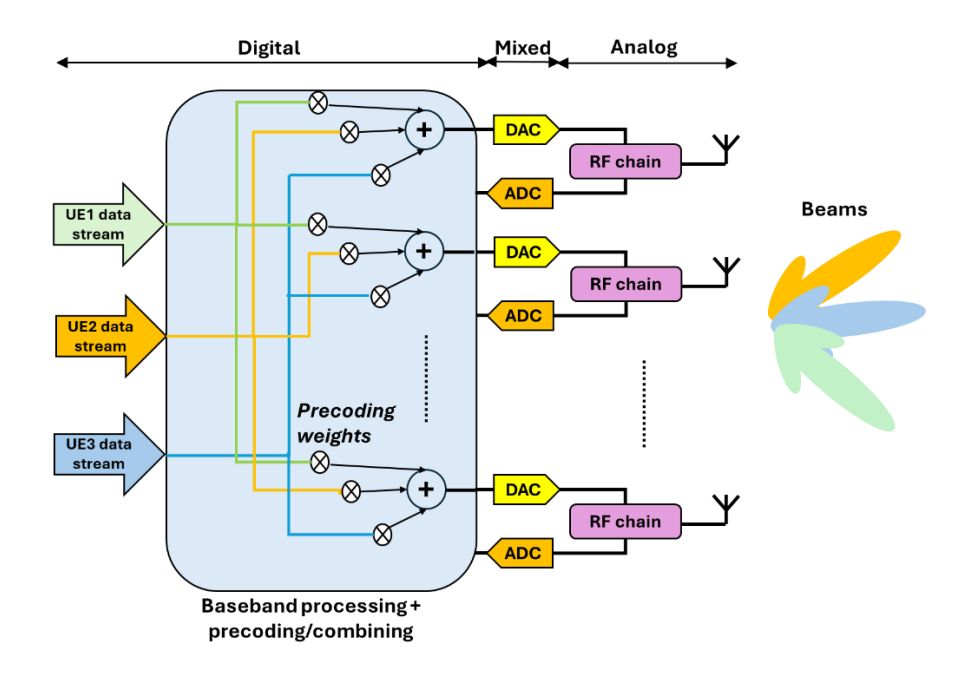


Figure 1-6 Digital beamforming architecture.

Antenna arrays and beamforming are well-established concepts in antenna and radar engineering. However, large arrays with beamforming capabilities have only recently been implemented in 5G networks deployed globally. While the topic was explored during 3G research, the technology and complexity at that time were too advanced for practical network implementation. During the standardization of 3G and 4G, capacity requirements could be met through the introduction of advanced link adaptation mechanisms and large bandwidths, particularly after the introduction of Orthogonal Frequency Multiplexing Access (OFDMA). OFDM, with its superior reliability in multipath propagation environments, proved more advantageous than the Wideband Code Division Multiple Access (WCDMA) method used in 3G.

The potential of mMIMO techniques has been extensively explored in academia, particularly through seminal works presented in [9][10]. The research showed that if the number of antenna elements is several times higher than the number of simultaneously served UEs, it is possible to create orthogonal beams to serve them. This enhanced performance is attributed to the "channel hardening" effect and favorable propagation conditions. The channel hardening effect, observed when numerous antenna elements are incorporated into the array, diminishes the impact of small-scale fading, resulting in a more stable channel. Favorable propagation, characterized by narrow bandwidths, minimizes inter-beam interference, enabling highly effective spatial filtering and beam orthogonality. Theoretically, Massive MIMO systems offer a near-linear increase in spectral efficiency with the number of antenna elements. However, practical implementation presents challenges, necessitating future advancements in MIMO technology to bridge the gap between theoretical potential and real-world performance.

Massive MIMO systems are evolving from simpler beamforming schemes, which rely on codebooks containing a finite set of orthogonal beams selected based on user equipment UE feedback, to advanced beamforming algorithms capable of adapting to time-frequency-space-

varying radio channel characteristics using sounding pilots transmitted from the UE. A more detailed exploration of these concepts is provided in Section 2.3. Multiantenna systems for BS are widely recognized as crucial for ensuring adequate coverage in the newly introduced millimeter-wave spectrum for mobile systems. The increased free space path loss, penetration loss, and vegetation loss at these higher frequencies can be effectively mitigated through the deployment of large antenna arrays.

## 1.3 Primary aspects of electromagnetic field exposure from multiantenna systems

Prior to market release and installation, base stations undergo a mandatory compliance assessment for electromagnetic field exposure. This assessment, conducted by the manufacturer and telecommunications operator, aims to establish compliance areas where EMF intensity remains below the prescribed limits outlined in reference [11].

The International Commission on Non-Ionizing Radiation Protection (ICNIRP) develops human exposure guidelines for non-ionizing radiation [12]. ICNIRP reports provide recommendations for basic restrictions in the form of Specific Absorption Rate (SAR) levels versus frequency. It's crucial to note that SAR levels have a safety factor of 50 applied for general public recommendations. This means that recommended limits of SAR is 50 times lower from the level which can cause a slight increase in human body temperature, approximately 1°C. However, the body's internal thermal regulation mechanisms remain stable and functional. It is challenging to assess the SAR by measurements, especially during field measurements. Therefore reference levels are derived to be able to easily measure exposure and verify compliance. The physical quantities which are provided as reference level:

- Electric field strength E
- Magnetic field strength H
- Power flux density S

The reference levels consider the Root Mean Square (RMS) exposure averaged over a period of 6 minutes for the general public and 30 minutes for workers, as specified in the ICNRIP report published in 1998. More recently, the latest ICNRIP report (published in 2020) recommends even a 30-minute averaging period for reference levels [12]. The averaging period is crucial in evaluating EMF exposure from mMIMO base stations with beamforming. This aspect will be discussed in detail in subsequent sections of this thesis.

The ICNIRP guidelines are supported by the World Health Organization (WHO) and the International Telecommunication Union (ITU). While the implementation of safety limits is a matter for individual nations, the majority of countries utilize the ICNIRP guidelines. Globally, 137 countries adhere to the international limit (ICNIRP 1998 or ICNIRP 2020), 10 follow the FCC 1996 limits, and 37 have established their own limits. The ICNIRP recommends a power density level of 10 W/m² for 5G massive MIMO base stations operating in the frequency range above 2 GHz. However, some countries, including Belgium, Italy,

Switzerland and India have adopted EMF exposure limits that are more stringent than those recommended by the ICNIRP [11].

Traditionally, base station compliance assessments have focused on maximum radiated power, neglecting factors like telecommunications traffic variability and terminal spatial distribution. To facilitate the deployment of massive MIMO base stations, an accurate and realistic assessment of EMF exposure is crucial, utilizing the averaging time specified in relevant exposure limits. The dynamic nature of beamforming necessitates the development of a new method for evaluating RF EMF exposure from multiantenna systems. The traditional approach, relying on the configured maximum Equivalent Isotropic Radiated Power (EIRP), can significantly overestimate compliance distances around the base station. This issue was investigated under the IEC62232 standard [7], "Determination of RF field strength, power density and SAR in the vicinity of radiocommunication base stations for the purpose of evaluating human exposure" and IEC TR 62269 technical report [14].

The actual maximum approach was recommended in the latest IEC 62232:2025 [15] and IEC TR62269:2025 [14], considers the variability of the traffic load and the beam patterns used during BF operations in the evaluation of compliance distances.

### 1.4 Actual EMF exposure from Massive MIMO base station

To determine the minimum compliance distance  $D_{min}$  (in m) from a transmitting antenna, the free space formula (1) can be employed. This formula utilizes the time-averaged transmit power  $P_{tx}$  (in W), the antenna gain  $G_{tx}$  and the maximum permissible power density  $S_{max}$  (in W/m2):

$$D_{min}(\varphi,\theta) = \sqrt{\frac{P_{TX}G_{TX}(\varphi,\theta)}{4\pi S_{max}}}$$
 Equation 1-1

where  $\varphi$  represents the azimuth angle and  $\theta$  denotes the elevation angle.

Regulatory guidelines typically mandate the use of the maximum configured transmit power and antenna gain of the BS under analysis to ensure conservative compliance distances when assessing RF EMF exposure.

In the case of Time Division Duplex (TDD) systems, the transmit power ( $P_{tx}$ ) is calculated using formula:

$$P_{TX} = P_{TX \ max} F_{TDC}$$
 Equation 1-2

where  $P_{tx\_max}$  represents the maximum configured transmit power, and  $F_{TDC}$  is the technology duty cycle factor for downlink (DL).

For frequency-division-duplex (FDD) systems, the  $F_{TDC}$  coefficient is equal to 1, as the downlink (DL) and uplink (UL) channels operate on distinct frequencies separated by a duplex distance. However, in TDD systems, the  $F_{TDC}$  value varies depending on the frame configuration. For instance, an  $F_{TDC}$  of 0.75 indicates that the BS transmits for 75% of the time and receives for 25% of the time within each period.

Evaluating RF EMF exposure using above formulas is relatively straightforward when employing sectoral antennas with a static radiation pattern. This conservative method based on the configured maximum was the only one possible until IEC 62232:2017 [16].

Base stations equipped with multiantenna systems and beamforming capabilities can dynamically adjust beam radiation patterns to match the specific characteristics of the radio channel for each user. The signals emitted from mMIMO BS exhibit significant variability in both direction and amplitude. The high directional gains of mMIMO antennas can lead to an overestimation of compliance distances when the assessment of radio frequency electromagnetic field exposure is based on the configured maximum transmitted power as illustrated on the Figure 1-7 below.

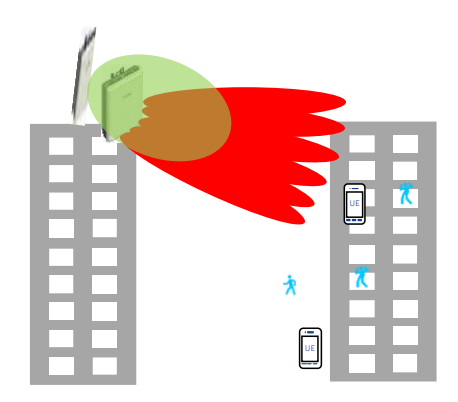


Figure 1-7 Illustration of overestimation in compliance distance calculated using maximum transmit power approach.

To address this inaccuracy, the IEC 62232:2022 standard [7] introduced the "actual maximum approach." This approach considers the realistic operation of mMIMO systems for RF EMF exposure assessment, incorporating time averaging over 6 or 30 minutes, as recommended by the latest ICNIRP guidance [12]. The actual maximum approach accounts for the realistic time-averaged spatial distribution of RF EMF resulting from beamforming and spatial multiplexing techniques employed in mMIMO BS.

Consequently, the actual EMF level is influenced not only by deterministic factors, such as the fixed  $F_{TDC}$  coefficient but also by stochastic coefficients derived from statistical analyses. These analyses typically utilize the Cumulative Distribution Function (CDF) of the average radiated power in a specific direction.

Therefore, a more accurate compliance distance can be determined by employing the actual maximum transmitted power ( $P_{TX\_actual}$ ), calculated using the formula provided below:

$$P_{TX \ actual} = P_{TX \ max} F_{TDC} F_{PR}$$
 Equation 1-3

where  $F_{PR}$  is the power reduction factor [2].

The Power Reduction Factor  $(F_{PR})$  [15] is determined by the 95th or 99th percentile of the CDF of the averaged EIRP. This value is obtained through computational modeling or measurements. The  $F_{PR}$  coefficient is essential for accurately estimating the time-averaged radio frequency electromagnetic field exposure for massive mMIMO base stations.

Consequently, the compliance distance determined using this approach is shorter and more representative of real-world conditions, as indicated in [14] and illustrated on Figure 1-8.

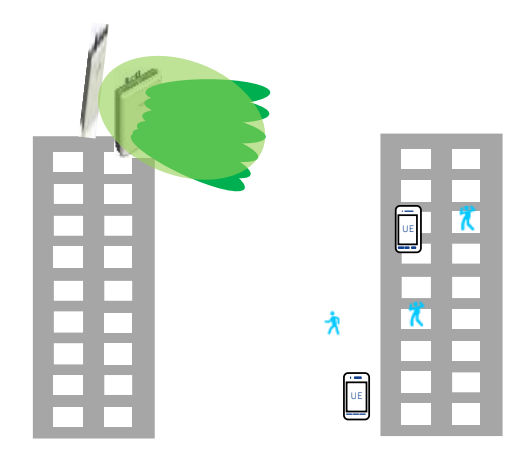


Figure 1-8 Illustration of compliance distance calculated using actual maximum approach for mMIMO Base Station.

The example of calculations for typical sectoral and mMIMO antennas are shown below:

### **Scenario 1: Sectoral Antenna**

• Antenna Gain (G<sub>TX</sub>): 14 dBi

• Transmit Power (P<sub>TX</sub>): 100 W (50 dBm)

Technology Factor (F<sub>TDC</sub>): 0.75

• Permissible Power Density (S<sub>max</sub>): 10 W/m<sup>2</sup>

**Result:** Compliance distance  $(D_{min}) = 3.35$  m using the maximum power approach.

### Scenario 2: mMIMO Antenna

Antenna Gain (G<sub>TX</sub>): 23 dBi

• Transmit Power (P<sub>TX</sub>): 100 W (50 dBm)

Technology Factor (F<sub>TDC</sub>): 0.75

• Power Reduction Factor (F<sub>TDC</sub>): -6 dB

• Permissible Power Density (S<sub>max</sub>): 10 W/m<sup>2</sup>

#### **Results:**

- Compliance distance (Dmin) = 9.5 m using the maximum power approach.
- Compliance distance (Dmin) = 4.7 m using the actual maximum approach.

The calculations demonstrate that for sectoral antennas with a typical gain of 14 dBi, the compliance distance is relatively small. However, for mMIMO antennas with significantly higher gains (e.g., 23 dBi) and the same transmit power, the compliance distance calculated

using the maximum power approach can be significantly larger (almost three times in this example).

When the actual maximum approach is applicable for mMIMO BS, a power reduction factor can be applied. A typical value of -6 dB, commonly used in currently deployed mMIMO BS, can reduce the compliance distance by approximately half.

It is important to note that practical mMIMO antennas can operate with higher transmit power (even 200 W) and larger antenna arrays, leading to even greater antenna gains (30 dBi or more). This can result in very large compliance distances, which may be unacceptable from a deployment perspective.

Therefore, the actual maximum approach is recommended for deploying mMIMO BS, particularly in locations where a small compliance distance is crucial. This approach effectively balances the need for coverage and capacity with the requirement for minimizing the impact on the surrounding environment.

Various statistical models have been developed to determine the  $F_{PR}$  value, as summarized in [17]. However, numerous important topics require further investigation in this field, which served as the primary focus of my research.

### 1.5 Research focus and objectives

This dissertation thesis investigates the electromagnetic field exposure characteristics of 5G base stations employing multiantenna systems with beamforming. The research addresses the following five Key Questions:

- **Q1. Actual EMF Distribution:** What is the spatial distribution of actual EMF exposure in the vicinity of a 5G base station utilizing multiantenna systems with beamforming?
- **Q2. Statistical Channel Modeling:** What statistical model is most suitable for estimating the actual RF EMF exposure near a 5G base station equipped with a multiantenna system?
- **Q3. Beamforming Impact:** How do different digital antenna beamforming algorithms influence the level and spatial distribution of the actual RF EMF exposure?
- **Q4. Power Reduction Factor:** How can the power reduction factor values used for the actual maximum approach be effectively estimated for a given 5G network scenario and base station parameters?
- **Q5. Actual RF Emissions Control:** How can radiation from the base station be effectively minimized in specific directions to meet regulatory requirements and minimize negative impacts on 5G network performance?

### **Three Research Hypotheses:**

- **H1. Antenna Array Size:** As the size of the antenna array increases, the actual EMF exposure in the vicinity of the base station decreases under real propagation conditions and a random distribution of users.
- **H2. Advanced Beamforming:** Advanced beamforming algorithms that adapt to the instantaneous characteristics of the radio channel result in lower actual EMF exposure levels.
- **H3. Statistical Modeling of Power Reduction Factor:** The power reduction factor can be effectively modeled using statistical methods.

### The significance of the research:

The assessment and control of electromagnetic field strengths are becoming increasingly crucial in the development of broadband radio systems. These systems must balance the growing demands of information society with the regulatory requirements for electromagnetic emissions.

This dissertation focuses on the new (5G) and future generations of mobile networks operating across a wide frequency range, including millimeter waves up to 300 GHz. These networks utilize multiantenna MIMO systems with digital antenna beamforming, requiring interdisciplinary research in electronics, telecommunications, and computer science.

The research findings would contribute to the development of methods for modeling, evaluating, measuring, extrapolating, and controlling EMF exposure in advanced multiantenna systems. These results could refine existing RF EMF exposure standards and regulations, as well as to develop novel methods for controlling EMF exposure with multiantenna systems.

Ultimately, this research could contribute to the formulation and development of the latest standards for wireless mobile telecommunications systems.

The summary of the achievement is elaborated in the Chapter 9.

## 1.6 Organizations of the thesis

That Thesis is comprised of ten Chapters.

Chapter 1 outlines the motivation for this research. It begins with an introduction to multiantenna systems incorporating beamforming, followed by a discussion of the primary aspects of electromagnetic field exposure associated with such systems. Building upon this foundation, the Chapter delves into the definition of actual EMF exposure method for Massive MIMO antennas. Finally, the Chapter concludes with a clear articulation of the research focus and objectives.

Chapter 2 explores the various channel model simulation aspects of radio modeling of electromagnetic field exposure originating from multiantenna systems. The Chapter first examines the challenges associated with modeling RF EMF exposure. Subsequently, it explores the use of system-level simulators incorporating radio channel models. The Chapter also

highlights the significance of statistical analysis in assessing RF EMF exposure from beamforming antennas.

Chapter 3 presents the findings of a study investigating multiantenna systems that utilize 'Grid of Beam' (GoB) beamforming. The Chapter begins with an analysis of EMF exposure from sectoral antennas. It then examines the performance of various antenna and GoB configurations, with a particular focus on the sub-GHz band. Additionally, the Chapter explores the actual EMF exposure from small cell base stations operating in the millimeter wave frequency band. The impact of averaging time on actual EMF exposure is also investigated within this Chapter.

Chapter 4 focuses on the impact of moving terminals on actual EMF exposure. The Chapter introduces and explains a model for moving terminals. It then conducts a statistical analysis of actual EMF exposure from mMIMO BS serving moving terminals, comparing the results to those obtained for static terminals. The Chapter also evaluates the electric field strength levels for both users of mobile phones and individuals within the coverage area of the base station.

Chapter 5 investigates the impact of various beamforming algorithms on EMF exposure. The Chapter begins by describing the beamforming algorithms used in the channel model simulation tool. It then analyzes the performance of cellular systems with mMIMO BS employing various beamforming algorithms. Finally, the Chapter compares and elaborates on the actual EMF exposure resulting from different beamforming schemes.

Chapter 6 concentrates on extreme mMIMO BS, which are being considered for the 6G generation of wireless communication standards and the new 7-15 GHz frequency band. The Chapter analyzes the performance of these systems in terms of capacity and coverage, particularly for very large antenna arrays. It also investigates the impact of increasing the size of the antenna array on actual EMF exposure and evaluates the actual field strength levels experienced by humans.

Chapter 7 presents an experimental study conducted in a specialized anechoic chamber built for testing mMIMO BS with beamforming. The measurement setup is described, and the use cases employed during the measurements are presented. Subsequently, the measurement results for these use cases are presented, and the findings are evaluated.

Chapter 8 presents the research results in the area of actual EIRP control. The Chapter begins with an introduction to various known techniques for actual EIRP control and their impact on system performance. It then presents a novel method developed by the author, based on optimal beam broadening for multipath channels targeted for GoB-type beamforming. The Chapter also describes a novel algorithm for advanced beamforming schemes based on channel reciprocity. Both new algorithms are analyzed in this Chapter.

Chapter 9 concludes the research studies conducted by the author, elaborating on the achievements. This Chapter also provides a perspective on future research directions in in the area of EMF exposure for multiantenna systems.

Chapter 10 contains the bibliography referenced throughout the dissertation.

# 2. Modelling of actual electromagnetic field exposure from multiantenna systems

## 2.1 Introduction to problem of evaluation of EMF exposure from multiantenna systems

The evaluation of EMF exposure from multiantenna systems presents a complex challenge. Measurement studies are not always feasible, particularly for newly introduced mMIMO antenna technologies and novel beamforming algorithms. Therefore, analytical studies and computational modeling are essential in this domain [15][14].

Analytical studies are often impractical for most use cases due to the complexity of evaluating mMIMO systems, which typically involve large antenna arrays embedded in base stations with advanced beamforming schemes, schedulers, and link transmission methods. In such scenarios, computer simulation emerges as a more suitable solution, enabling the modeling of complex wireless systems, a practice that has been successfully employed in research, standardization, and industry since the inception of cellular communication [18].

Computational modeling is recognized in IEC 62232:2025 [15] and IEC TR 62669:2025 [14], alongside measurement methods, as a recommended approach for analyzing the actual maximum approach and estimating the power reduction factor. Therefore, this study utilizes an advanced proprietary system-level simulator for evaluating massive MIMO networks. The core of this simulator is based on the statistical 3D spatial model of radio wave propagation, adhering to the 3GPP technical report 38.901 [19]. This standardized channel model is widely adopted by academia and industry for constructing link-level and system-level simulators.

Various statistical models have been developed for conduction actual EMF exposure studies from mMIMO systems and to determining the power reduction factor levels. A primary references for this topic are in [6][20][26][21], and a comprehensive summary can be found in [17].

A comprehensive statistical model for computational modeling of EMF exposure should encompass the following elements:

- Base station model
- Radio propagation model
- Antenna array model
- Beamforming algorithms
- User equipment model
- Traffic model

This dissertation primarily utilizes computer modeling methods. Advanced computer simulations were conducted using a 5G system level simulator. The system-level simulator employed in this research is detailed in the subsequent Section.

## 2.2 System level simulator of Massive MIMO and EMF exposure

The proprietary system-level simulator (SLS), used by Nokia for evaluating system performance, introducing new features, and designing novel techniques, was adopted for the research required for this doctoral thesis. This SLS tool is fully based on 3GPP assumptions [19] [22], and the simulation results generated by this tool are presented in various 3GPP contributions and research publication.

The BS model utilized in simulator with main functional blocks is depicted on Figure 2-1. In the simulation of EMF exposure, we focused only on DL transmission. Therefore, the DL part of simulator is only described. In the UL only the feedback signals is used in simulation which are require for DL path of BS to operate.

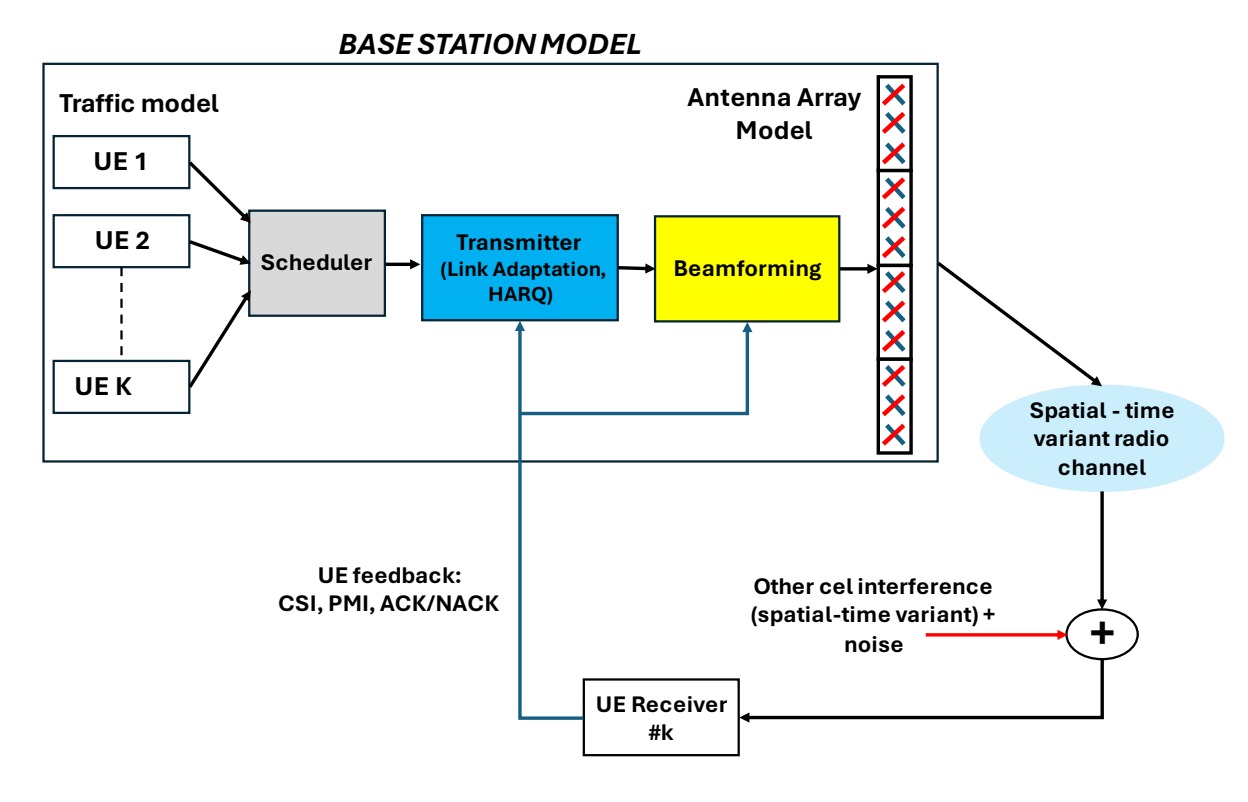


Figure 2-1 The basic block diagram of Base Station model used in SLS tool (Downlink).

#### Traffic model:

Each cell within a BS serves multiple UEs. The traffic for these UEs is generated based on specific traffic models and buffered within the BS until successful transmission. The traffic model generated for each UE is transmitted towards scheduler. In the simulation full buffer traffic model was selected, where each UE is assumed to have a full buffer of data awaiting transmission. The full-buffer model lacks time-variant variables. If at least one UE per cell has

a full buffer, all cells experience constant full load, as they always have an infinite amount of data to transmit.

Full buffer model is a simplification that has limited real-world applicability. However, its simplicity makes it useful for certain types of simulations. In EMF exposure studies, the primary focus is on evaluating the impact of beamforming and UE distribution. The full buffer model, which assumes full transmit power utilization, is rarely encountered in real-world networks. However, this overestimation is frequently employed in EMF studies to analyze worst-case scenarios.

#### The Scheduler:

The scheduler is a critical component in managing the resources of a 5G network, ensuring efficient and equitable allocation of bandwidth and other resources to diverse users and applications. Its key functions include four roles:

- **Resource Allocation:** The scheduler determines which user or application receives access to specific resources, such as frequency bands and time slots, at any given moment.
- Traffic Prioritization: The scheduler prioritizes different types of traffic based on their importance or service requirements, such as emergency calls or video streaming.
- Load Balancing: The scheduler distributes traffic across various cells and sectors to prevent congestion and optimize network performance.
- **Dynamic Resource Allocation:** The scheduler dynamically adjusts resource allocation in response to evolving network conditions and user demands.

Through effective resource management, the scheduler contributes significantly to the overall performance, reliability, and efficiency of the 5G network.

In the SLS tool Proportional Fair (PF) scheduler was used. Its primary objective is to achieve a balance between fairness in resource allocation and maximizing overall system throughput. This includes determining the specific Physical Resource Blocks (PRBs) on which the data will be transmitted.

Three main characteristics of PF scheduler used in simulations are listed below:

- **Resource Allocation:** The PF scheduler dynamically assigns resources, such as bandwidth or transmission power, to users based on their current channel conditions and data rates. Users experiencing favorable channel conditions (stronger signal) or higher data rates are allocated a larger share of resources.
- **Fairness:** The scheduler ensures that resource allocation is proportional to the UEs average data rates. This means that users with lower average data rates receive a larger share of resources to compensate for their lower performance, promoting fairness among users.

• **Throughput Maximization:** By prioritizing users with better channel conditions, the PF scheduler optimizes overall system throughput. This is because UEs with stronger channels can transmit data at higher rates, leading to increased data throughput for the entire system.

### Link adaptation and HARQ:

The link adaptation block optimizes the transmitted signal to ensure reliable propagation through the radio channel. Techniques such as modulation, rank level, or coding can be employed to mitigate the effects of complex radio channel conditions. The Hybrid Automatic Repeat Request (HARQ) block retransmits packets that fail to reach their destination, ensuring reliable data delivery.

### **Beamforming:**

Beamforming weights are applied to the scheduled signal for each user equipment. The beamforming algorithms employed in the simulation are detailed in the next Section.

### Antenna array model:

In the SLS tool antenna model specified in 3GPP [19] is implemented and shown in Figure 2-2.

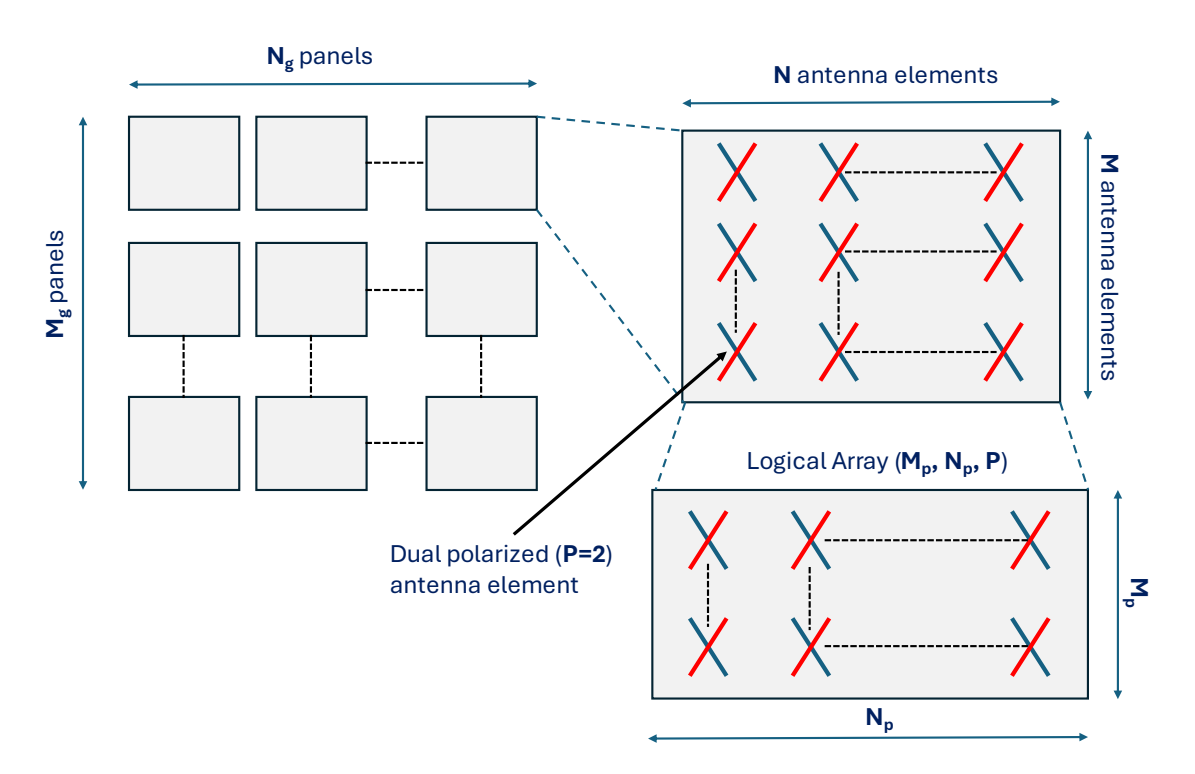


Figure 2-2 Antenna array model.

3GPP employs the following antenna configuration notation:  $(M, N, P, M_g, N_g; M_p, N_p)$ , where:

• **M and N** represent the number of vertical and horizontal antenna elements within a panel, respectively.

- **P** denotes the number of polarizations.
- $M_g$  and  $N_g$  represent the number of panels in a column and row, respectively.
- $M_p$  and  $N_p$  indicate the number of vertical and horizontal TRX (transceiver units) within a panel and polarization, with  $M_p \le M$  and  $N_p \le N$ .

For large antenna systems, the antenna array can be divided into sub-arrays. This is achieved by connecting  $M/M_p$  consecutive vertical antenna elements and  $N/N_p$  consecutive horizontal antenna elements into two TRX (one per polarization). The phase and amplitude of the antennas within each sub-array are then controlled collectively.

### **UE** model

The simulated UEs use a single omnidirectional antenna and are randomly distributed in a cell, where 20% of them are outdoors and 80% indoor, inside the buildings whose heights are uniformly distributed between 4 and 8 floors (model according to 3GPP 38.901 [19]). UEs locations are static but UE positions are randomly rotated every drop. The number of terminals served terminals, K, is 1, 2, 5 or 8 and the drop duration of a single DL connection, D is time period and 10 s, 60 s and 360 s were used. The impact of moving UE is studied in Chapter 4.

### The process of DL transmission:

The link adaptation process in the SLS is based on feedback from the UE, including channel state information (CSI), precoding matrix indication (PMI), and acknowledge/negative acknowledge (ACK/NACK) messages.

After a transmission from the cell to a UE, the SLS calculates the received signal at the UE, considering:

- The transmit antenna array at the BS,
- Beamforming algorithm,
- Radio propagation characteristics,
- The antennas at the UE,
- Interference from other cells in the system on the PRBs of the desired signal.

This includes modeling cross-coupling between the performance of cells in the network.

Based on this, the SLS computes the received signal-to-noise ratio (SINR), often calculated per symbol of the transmitted signal. These SINR values are used to compute the effective SINR of the transmission.

The effective SINR is then mapped to mutual information using a lookup table obtained from link-level simulations. This lookup table determines the probability of correct reception of the transmission.

The combination of these steps, from SINR calculation to probability of correct reception, is referred to as the link-to-system-level (L2S) interface. This interface essentially forms a physical layer abstraction model for the SLS.

#### **Network deployment scenarios**

The BS model described above is deployed in the cellular structure shown on Figure 2-3. Urban Macro (UMa) and Urban Micro (UMi) are used in simulations and both are based on the same regular hexagonal grid structure consisting in 7 BS sites with 3 sector sites. The BS are in specified Inter-Site Distance (ISD) between them.

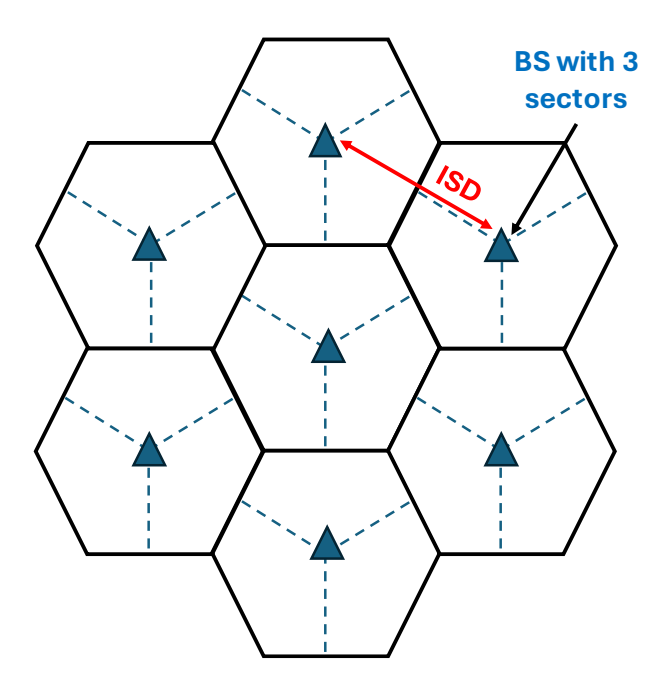


Figure 2-3 Classical mobile network cell layout structure with 3-sector Base Station and the ISD in fixed in that scheme.

The main characteristics of Urban Macro (UMa) and Urban Micro (UMi) deployments are summarized as follows:

#### **Urban Macro (UMa)**

- **Deployment:** Urban environment with gNB antennas located above rooftop level.
- **Site Configuration:** Hexagonal grid of 3-sector sites with an inter-site distance (ISD) of 500 meters.
- **Antenna Heights:** gNB antenna height of 25 meters and UE antenna height of 1.5 meters.
- **UE Distribution:** 80% of UEs are indoor and 20% are outdoor. Indoor UEs are uniformly distributed across different floors, typically assuming buildings with 6 floors.

### **Urban Micro (UMi)**

- **Deployment:** Dense urban environment with gNB antennas located in street canyons.
- **Site Configuration:** Hexagonal grid of 3-sector sites with an ISD of 200 meters.
- Antenna Heights: gNB antenna height of 10 meters and UE antenna height of 1.5 meters.

• **UE Distribution:** 80% of UEs are indoor and 20% are outdoor. Indoor UEs are uniformly distributed across different floors, typically assuming buildings with 6 floors.

Simulating only the pictured hexagonal grid in Figure 2-3 can introduce "border effects," where UEs in outer cells experience less received interference compared to those in central cells. This occurs because outer cells "see" fewer surrounding cells. This non-uniformity can skew statistical analysis.

To mitigate this, wrap-around techniques are commonly employed. This approach replicates the desired cell cluster six times, creating a uniform surrounding for the central cluster, which is explicitly simulated and used for statistical analysis. This is depicted in Figure 2-4 from point of view of UE in the coverage of center BS and on Figure 2-5 from point of view of UE in the coverage of border BS.

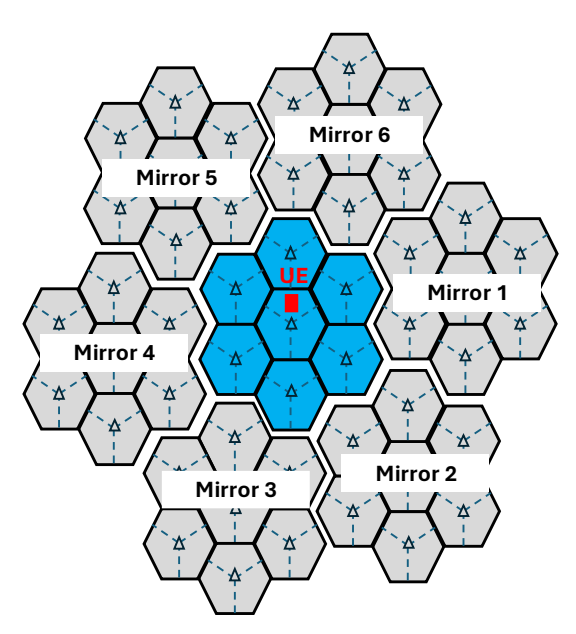


Figure 2-4 "Wrap around" techniques from point of view of UE in the center of grid.

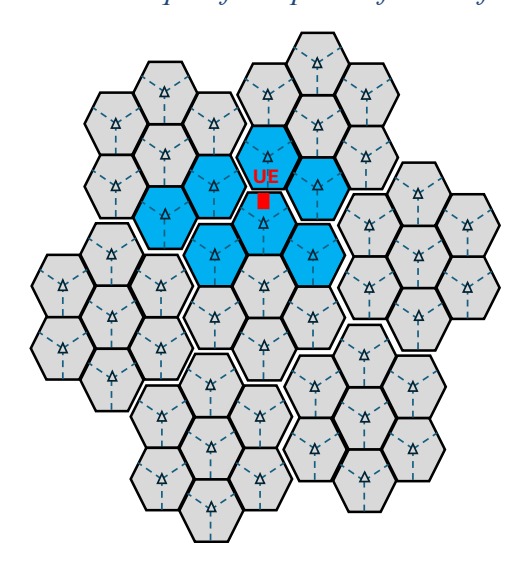


Figure 2-5 "Wrap around" techniques from point of view of UE in the border of grid.

For further details on wrap-around techniques and their implementation in SLS, refer to reference [18].

### 2.3 Beamforming algorithms

In multiantenna systems, beamforming plays a crucial role in enhancing cell coverage and capacity. This technique involves multiplying the scheduled signal for each UE by beamforming weights, effectively directing the transmitted energy towards a specific UE [2][3].

Two primary techniques contribute to the benefits of multiantenna systems: BF and spatial multiplexing. BF focuses the transmitted energy towards a specific UE, maximizing signal strength while minimizing energy transmission in other directions. This approach optimizes power consumption and reduces radio RF EMF exposure in areas without users.

Spatial multiplexing, on the other hand, utilizes BF algorithms to send multiple data streams to spatially separated UEs simultaneously, thereby increasing spectral efficiency.

Channel estimation is essential for enabling BF. Two main approaches exist:

- 1. **UE Feedback:** The UE measures DL reference signals transmitted by BS, identifies the optimal beam from a predefined set, and informs the BS. This robust technique operates under various radio channel conditions. However, beam selection may be suboptimal due to limited channel information and beam resolution.
- 2. **Reciprocity-Based Channel Estimation:** The BS measures the UL sounding reference signal (SRS) sent by the UE, estimates the DL channel, and selects or creates the optimal beam. This approach allows for optimal beam selection and BF weight adaptation due to more accurate channel estimation (eigenbeamforming EBF). It also enables beam shape adaptation to minimize interference, as demonstrated by the eigenbeamforming zero-forcing (EZF) technique.

While reciprocity-based techniques theoretically allow for an unlimited number of beams, they require high-quality channel estimation and sufficient UL link budget due to the limited UE transmit power. This limits the cell coverage range where this technique can be effectively employed.

The EBF (Figure 2-7) and EZF (Figure 2-8) techniques leverage multipath propagation to construct UE-specific beams in multiple directions, including main lobes. These beams can have arbitrary shapes, covering several propagation paths.

Realistic multi-path channels with angular spread introduce small-scale fading effects, impacting the highly phase-dependent beam shape. This dynamic and unpredictable nature of beam shapes raises concerns regarding RF EMF exposure, particularly in the context of power reduction factor estimation for massive MIMO BS, as outlined in IEC 62232: 2025 [15].

In the case of grid of GoB the antenna array generates multiple beams per polarization uniformly distributed within 120 degrees of azimuth opening angle and elevation angles (Figure 2-6). While GoB enables simultaneous service for multiple users through spatial multiplexing, the limited beam resolution results in low Multi-User MIMO (MU-MIMO) gains.

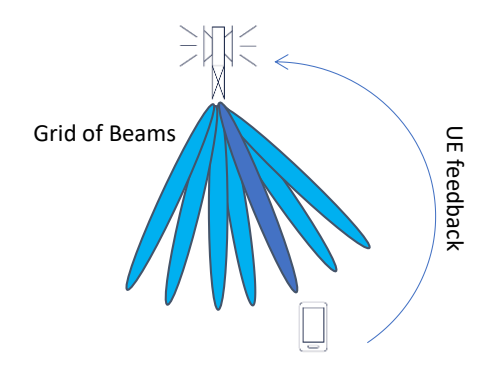


Figure 2-6 Illustration of GoB type of beamforming. UE can be stationary or on move.

EBF utilizes the channel covariance matrix averaged over the full carrier bandwidth. The strongest eigenvectors of this matrix are used as a precoder. Similarly, EZF employs the averaged channel covariance matrix for zero forcing precoding calculations. In simulations, ideal channel state information (CSI) based on UL pilot is assumed, without considering pilot contamination.

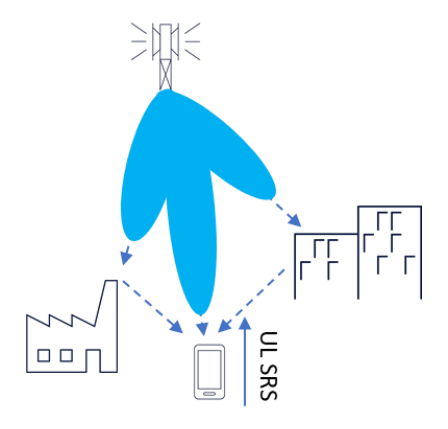


Figure 2-7 Illustration of EBF beamforming. UE can be stationary or on move.

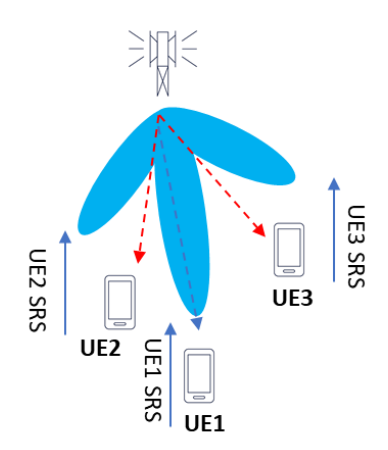


Figure 2-8 Illustration of EZF beamforming. UE can be stationary or on move.

The BF algorithm significantly impacts both electromagnetic field (EMF) exposure and power reduction factor estimation. A dedicated chapter explores this topic in detail, presenting novel and intriguing findings.

### 2.4 Radio wave propagation and channel modeling

Core of the simulator is based on the statistical 3D spatial model of radio wave propagation in accordance with 3GPP technical report 38.901 [19][22]. Accurate modeling of radio propagation effects is paramount for achieving realistic system-level performance results. This modeling influences both the desired signal reception at the receiver and the experienced interference at various receivers within the system.

When analyzing EMF exposure from massive MIMO (mMIMO) systems, accurate radio channel modeling is crucial. This is because the channel significantly influences the beamforming algorithm, ultimately determining the direction and shape of the resulting antenna pattern for a specific channel realization.

3D statistical-spatial channel models are particularly valuable for this analysis. They are constructed based on measurements from diverse deployment scenarios, offering the opportunity to analyze EMF exposure across a wide range of channel characteristics.

In mMIMO antenna systems, the radio channel must be modeled individually between each antenna element (per polarization) and the user equipment, as illustrated in Figure 2-9. This requirement leads to the need for thousands of radio channel calculations within a single simulation run.

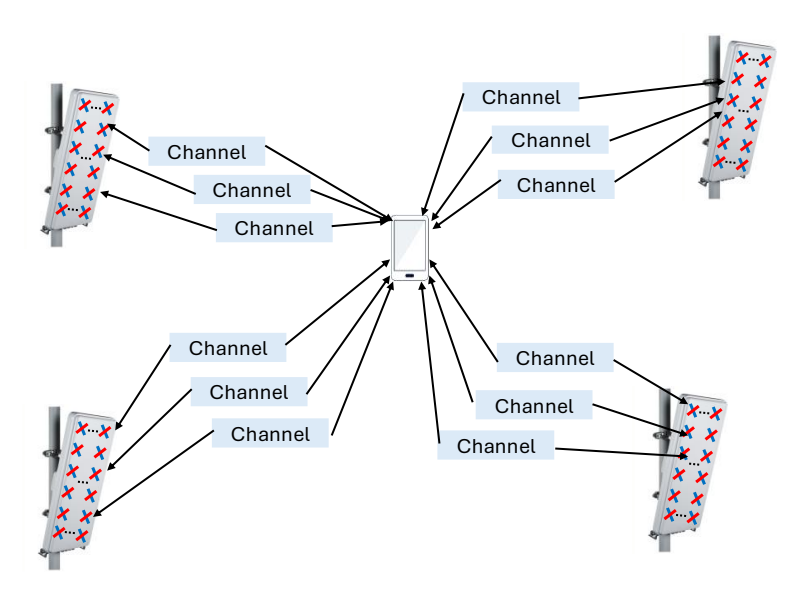


Figure 2-9 Illustration of multiplicity of radio channels calculations in SLS tool.

Radio propagation is characterized by multipath propagation, which arises from primary propagation phenomena such as reflections, diffractions, and penetrations of electromagnetic waves within the surrounding environment. Consequently, the electromagnetic wave travels from the transmitter to the receiver along multiple paths (Figure 2-10).

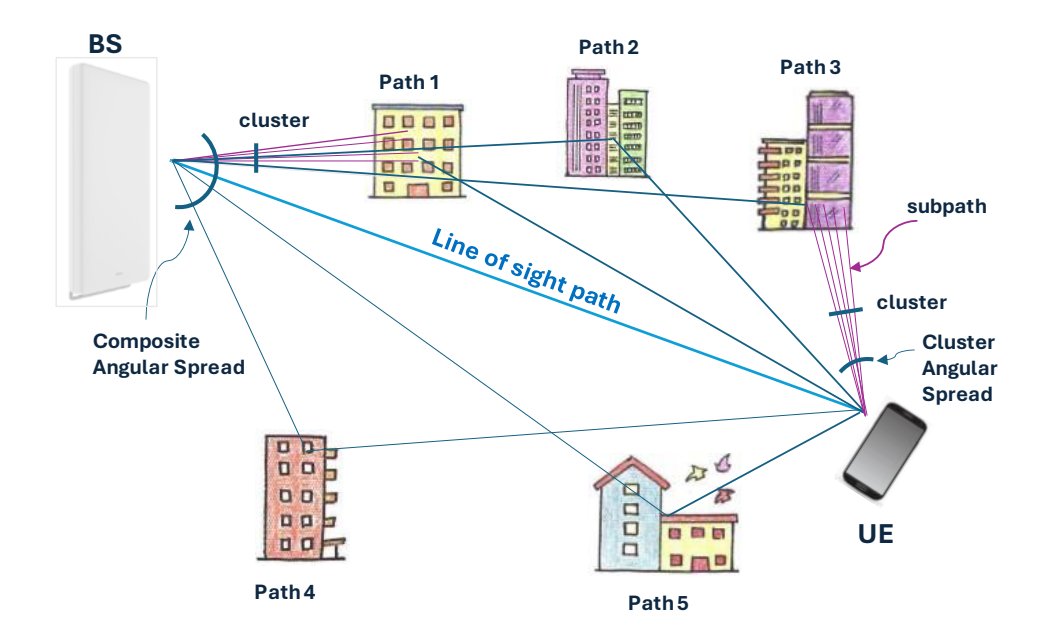


Figure 2-10 Example of extension multipath propagation in urban environment.

In terrestrial environments, radio wave propagation is clustered due to the limited number of objects, such as buildings, trees, and street furniture, which interact with the waves. Each cluster contains multiple sub-paths. The spatial distribution of multipaths is characterized by composite angular spread, encompassing both cluster and individual path angular spreads.

A more detailed model of the spatial channel is illustrated in Figure 2-11. This model depicts how clusters and multipath propagation contribute to the delay spread and angular spread characteristics of the radio channel, which influence the modulated signal transmitted through it. The impact of angular spread is particularly significant for narrow beams from massive MIMO antennas, and this effect is further discussed in Section 8.3.1.

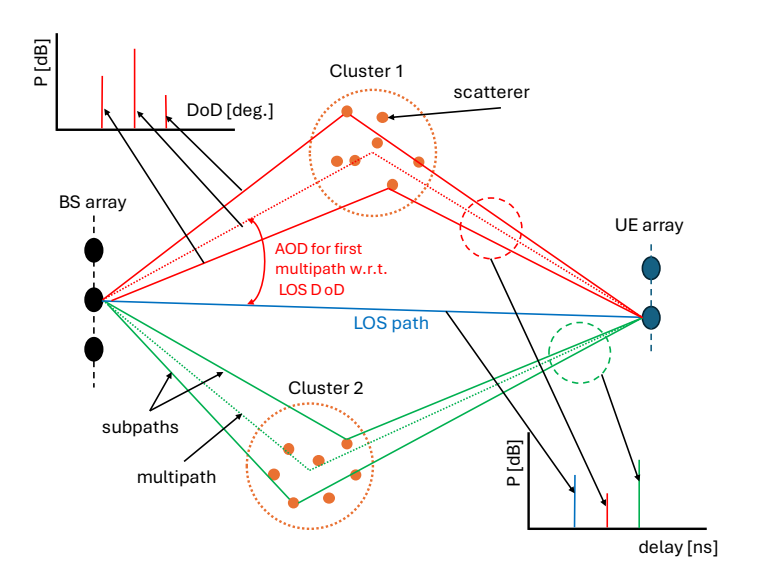


Figure 2-11 Representation of clusters and multipath in channel model. The complexity is substantially increased when Doppler shifts are also considered.

In the SLS tool, all radio channel coefficients are calculated based on 3GPP TR 38.901, following the procedure outlined in Figure 7.5-1 of this document and using channel model parameters listed in Table 7.5-6 Part-1 for UMa and UMi scenarios [19].

## 2.5 Statistical analysis of EMF exposure from beamforming antennas

A Monte Carlo method was applied to model complex processes in a cellular system consisting of multiple base stations. This method incorporated models of BS with mMIMO and beamforming algorithm, varying numbers and distributions of users and 3D spatial-statistical model of radio wave propagation (all topics presented in the previous Sections). To ensure statistically reliable results, multi-drop simulations were conducted. These simulations involved running a series of simulations with different random distributions of UEs locations within the network. By combining the statistical data from each simulation, key performance indicators (KPIs) of interest could be extracted. Executing numerous simulation drops enhances the confidence in the assessment of these KPIs. Consequently, the number of drops for the SLS simulations was chosen to increase the sample size to at least 1000 different spatial UE locations.

This ensured the generation of a wide range of channel model realizations, enabling the beamforming algorithms to adapt to diverse channel conditions. Consequently, the actual EMF exposure could be analyzed for various UE distributions, which is crucial for MU-MIMO pairing algorithms. The multi-path channel realizations resulted in diverse antenna pattern shapes, directly impacting EMF exposure.

The actual EMF exposure in the vicinity of the mMIMO antenna was sampled using a grid layout depicted in Figure 2-12. This grid features a resolution of 5 degrees, spanning azimuth angles from -180 to 175 degrees and elevation angles from -90 to 90 degrees.

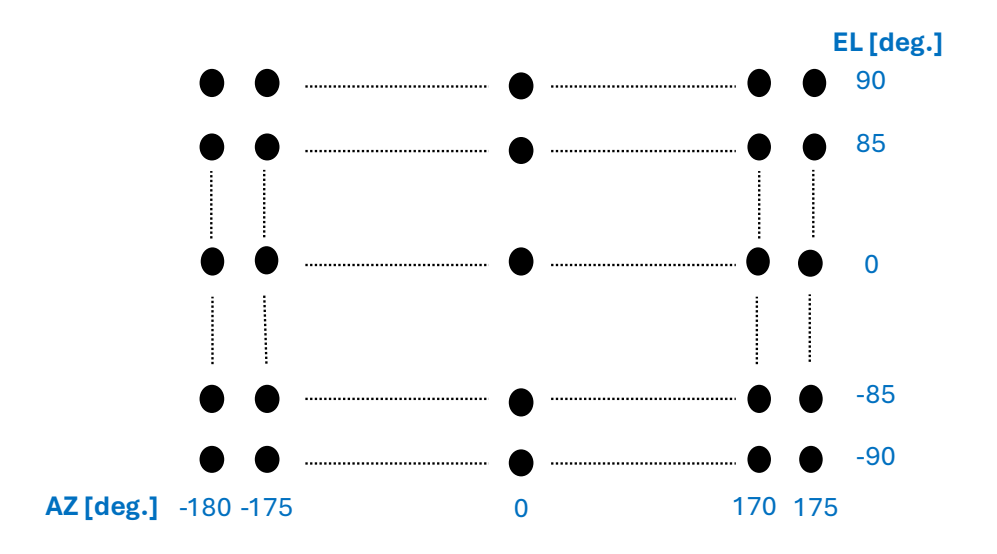


Figure 2-12 The grid layout in the vicinity of mMIMO antenna where actual EMF exposure was analyzed.

Azimuth and elevation angles are always calculated with respect to the center of the antenna. An elevation angle of -90 degrees indicates a direction pointing towards the floor, while +90 degrees points towards the ceiling. An azimuth angle of 0 degrees corresponds to the boresight of the antenna. Positive azimuth angles indicate directions to the left of the boresight, while negative angles indicate directions to the right. The definition of the coordinate system used for azimuth and elevation angles are summarized below:

• **Reference Point:** The center of the antenna is the origin for both azimuth and elevation angles.

### • Elevation:

- o -90 degrees: Points directly downwards towards the floor.
- o +90 degrees: Points directly upwards towards the ceiling.
- o 0 degrees: Represents the horizontal plane, with the antenna's boresight direction.

#### • Azimuth:

- o 0 degrees: Points towards the boresight direction of the antenna.
- o Positive angles: Rotate counterclockwise (left) from the boresight direction.
- o Negative angles: Rotate clockwise (right) from the boresight direction.

During the simulation, beamforming gain was calculated for each TRX and subframe across 2664 directions. This grid comprised (360/5) horizontal grid points multiplied by (180/5 + 1) vertical grid points. For each grid point, a mean value statistic was recorded, enabling the calculation of 2664 average beamforming gains at the simulation's results. The average beamforming gain in a specific direction represents a single sample for CDF in that direction. The simulation duration, and consequently the averaging time, was typically 6 minutes, as recommended by [15][14].

The SLS tool facilitates the generation of various statistical KPIs for analysis, as detailed in subsequent chapters. These KPIs include:

 Normalized Actual EIRP: This metric represents the time-averaged EIRP in a given direction, normalized by the maximum theoretical EIRP. The formula for normalized EIRP is:

$$EIRP_{norm}(\theta, \varphi) = \frac{EIRP_{avg}(\theta, \varphi)}{EIRP_{max}}$$
 Equation 2-1

### where:

- $\circ$  EIRP<sub>norm</sub>( $\theta, \varphi$ ) is the normalized EIRP in direction ( $\theta, \varphi$ )
- $\circ$  EIRP<sub>avg</sub>(θ,φ) is the time-averaged EIRP in direction (θ,φ)
- o EIRP<sub>max</sub> is the maximum theoretical EIRP
- Average Beamforming Gain: This KPI provides the average beamforming gain across the simulation period.

• Average Electric Field Strength: This metric represents the average electric field strength measured across the simulation.

The example of  $EIRP_{norm}(\theta, \varphi)$  is shown on Figure 2-13.

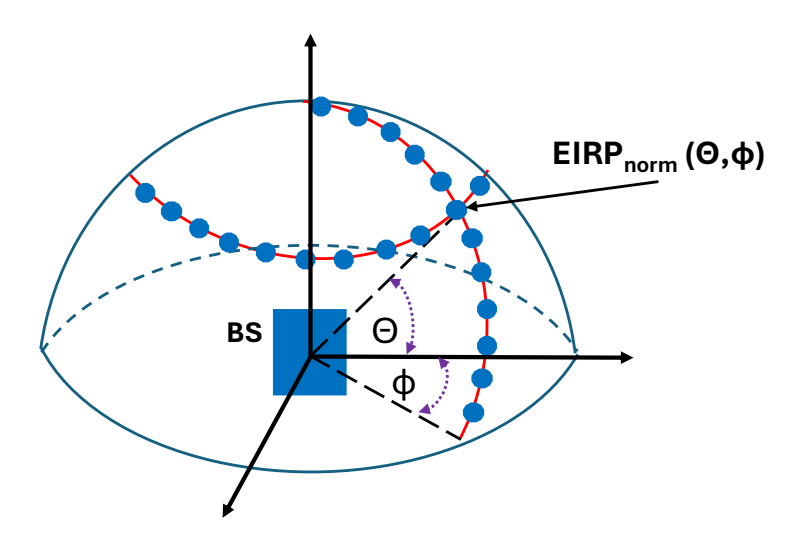


Figure 2-13 The visualization of sample grid where normalized EIRP is calculated.

The simulation results were analyzed to investigate the distribution of electromagnetic field strength within the mobile network under various system configurations. These configurations included different antenna array layouts, beamforming types, UE distributions, and mobility models (static or moving). The findings are presented and discussed in detail in the following chapters.

## 3. Actual EMF exposure from multiantenna systems with 'Grid of Beam' beamforming

### 3.1 Introduction

This chapter presents simulation results and discussions for various antenna array configurations employing GoB beamforming. The chapter begins by examining results for sectoral antennas with 2x2 and 4x4 MIMO configurations, providing a baseline for comparison with mMIMO antennas. Subsequently, simulation results for different antenna array sizes and GoB beam configurations are presented and analyzed. GoB beamforming is the primary beamforming scheme employed in deployed 5G mMIMO base stations.

The chapter then proceeds to present simulation results for millimeter-wave small cell base stations. The impact of averaging time on actual electromagnetic field (EMF) exposure is then elaborated through a discussion of simulation results. Finally, the chapter concludes with a summary of key findings.

### 3.1.1 The analysis of sectoral antennas

The analysis of EMF exposure from typical sector antenna is provided in this chapter for 2 antennas: sector antenna (column antenna) with MIMO 2x2 capability and sector antenna (2-columns antenna) with MIMO 4x4 capability.

### 3.1.1.1 Sector antenna with MIMO 2x2

Typical sectoral antenna used in 2G/3G/4G base stations was modeled in simulator. The sectoral antenna is the linear array antenna with 9 antenna elements in vertical direction as shown on Figure 3-1 with 3D antenna pattern.

The sector antenna contains dual polarized antenna element (+/- 45 degrees) and 2 TRXes are connected to antenna (each TRX to one polarization). The antenna generates static beam pattern (wide beamwidth in azimuth and narrow beamwidth in elevation) with 15 dBi of gain. The simulation assumptions are presented in Table 3-1.

The normalized actual EIRP is depicted in Figure 3-2 for this type of sectoral antenna remains constant. This indicates that the average EMF exposure is equivalent to the maximum EMF exposure. The antenna gain is fixed, and with the full-buffer traffic model, where all frames are transmitted at maximum power, no discernible fluctuations in EMF exposure are observed around the antenna.

Table 3-1 Main simulations assumptions.

Parameter	Value
Channel model	3GPP 38.901 Urban Macro (UMa)
Carrier frequency	1.8 GHz
Channel bandwidth	20 MHz
Sub-carrier spacing	30 kHz
Max total Tx power of BS (without losses)	46 dBm
No. of TRx	2
Gain of BS single antenna element	5.5 dBi
Configuration of BS antenna array per polarization (VxH)	9×1
Beamforming type	non-beamforming (fixed pattern)
Maximum antenna gain	15 dBi
Electrical down-tilt of BS antenna pattern	5°
TDD duty cycle for DL	0.75
Height of BS antenna array centre	25 m
No. of cells / No. of sectors	7 / 21
Inter-site distance	500 m
Type of UE antenna	2 Omnidirectional (one per polarization)
UE distribution	80% indoor, uniform distribution between floors (max. number of floors 4 to 8)
No. of simultaneously served UEs	1
UE serving time	10 s
Traffic type	Full buffer
The actual max approach averaging time	6 min

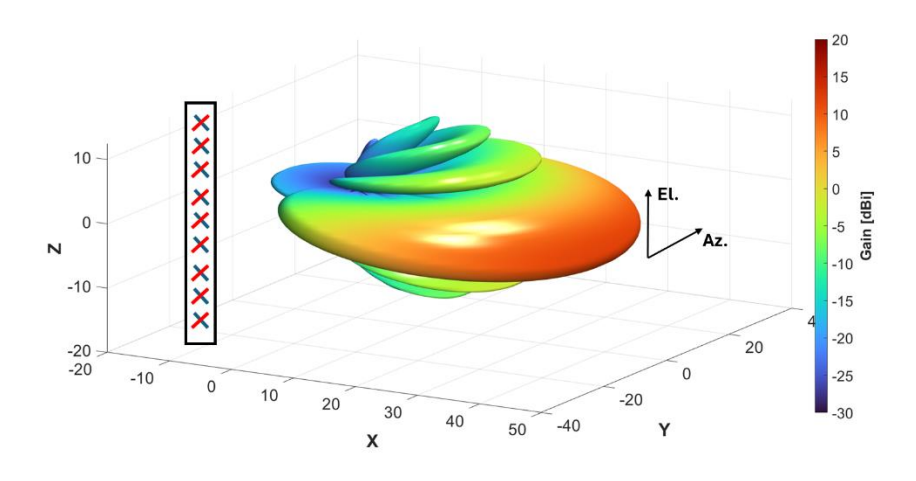


Figure 3-1 3D pattern of sectoral antenna.

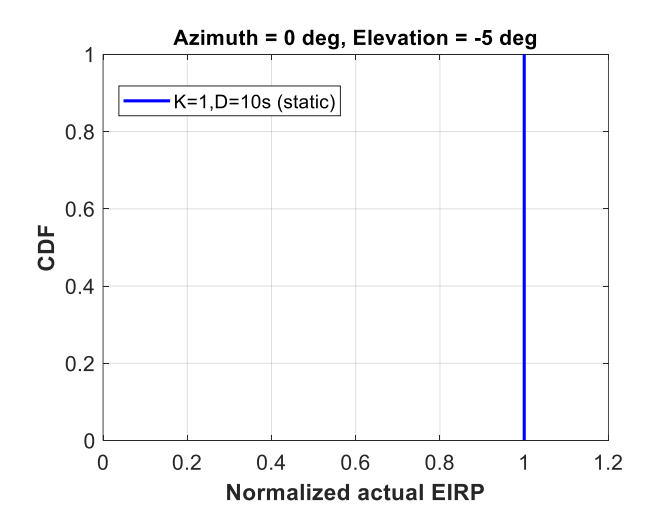


Figure 3-2 Simulation result of actual normalized EIRP from sectoral antenna.

The 2x2 MIMO configuration is implemented on two separate polarizations. Consequently, MIMO precoding does not influence the phase distribution across the antenna elements.

#### 3.1.1.2 Sector antenna with MIMO 4x4

For a MIMO 4x4 sector antenna, a configuration with two columns and four transceivers is required, as illustrated in Figure 3-3. To ensure adequate isolation between MIMO streams transmitted on the same polarization, the distance between the columns should be equal to the carrier wavelength  $(1\lambda)$ .

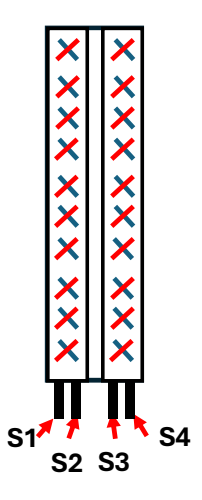


Figure 3-3 Sector antenna with 2 columns and MIMO 4x4 capability.

MIMO precoding is implemented based on the 3GPP codebook outlined in [23]. The MIMO precoder, guided by the reported channel state information reference signal (CSI-RS) feedback, sets the precoding weights for transmission. These weights incorporate varying phases for the antenna panels, enabling limited beamforming in the azimuth direction. This codebook generates 8 distinct beams in the azimuth direction. This configuration was replicated in the SLS tool, with the primary simulation assumptions summarized in Table 3-2.

Table 3-2 Main simulation assumptions.

Parameter	Value	
Channel model	3GPP 38.901	
Chainei modei	Urban Macro (UMa)	
Carrier frequency	3.5 GHz	
Channel bandwidth	20 MHz	
Sub-carrier spacing	30 kHz	
Max total Tx power of BS (without losses)	55 dBm	
No. of TRx	2	
Gain of BS single antenna element	4.9 dBi	
Configuration of BS antenna array per polarization (VxH)	10×2	
Beamforming type	4x4 MIMO precoding	
	8 distinct beams in azimuth	
Maximum antenna gain	17.9 dBi	
Electrical down-tilt of BS antenna pattern	5°	
TDD duty cycle for DL	0.75	
Height of BS antenna array centre	25 m	
No. of cells / No. of sectors	7 / 21	
Inter-site distance	500 m	
Type of UE antenna	2 Omnidirectional (one per polarization)	
UE distribution	80% indoor, uniform distribution between floors (max. number of floors 4 to 8)	
No. of simultaneously served UEs	1	
UE serving time	10 s	
Traffic type	Full buffer	
The actual max approach averaging time	6 min	

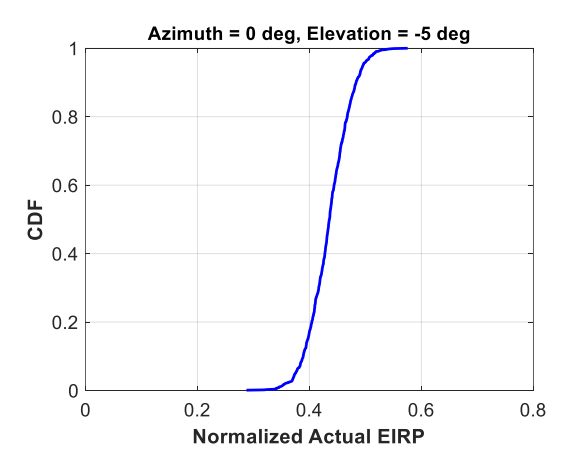


Figure 3-4 Simulation results - CDF of normalized actual EIRP for 4x4 MIMO sectoral antenna.

As anticipated, the normalized actual EIRP results exhibit some disturbances due to the MIMO 4x4 precoding, as depicted in Figure 3-4. The power reduction factor is approximately -3 dB, aligning with the findings presented in [23].

## 3.2 The evaluation of actual EMF exposure from various base stations configurations operating in sub-GHz band with GoB beamforming

### 3.2.1 Simulation assumptions

The system simulator model employed a statistical 3D spatial model of radio wave propagation, adhering to the 3GPP 38.901 UMa (Urban Macro) standard [19]. Simulations were conducted for a cellular network comprising seven cells, each equipped with three sectors featuring Massive MIMO multiantenna base stations. In this scenario, the base stations were positioned at a height of 25 meters, with a 500-meter distance between them. The system operated at 3.5 GHz, utilizing a 20 MHz bandwidth. Simulations were performed for three distinct multiantenna systems, with parameters detailed in Table 3-3. The spacing between antenna elements was set to half the wavelength. The antenna array was organized into smaller sub-arrays, as depicted in Figure 3-5 each connected to a separate TRX transceiver.

Parameter 32TRX\_8x8 64TRX\_12x8 64TRX\_12x16 Number of TRXes 32 64 64 Number of antenna elements (V×H) 8x8 12x8 12x16 Sub-array configuration (VxH) 4x1 3x1 6x1 Maximum antenna gain [dBi] 23.3 25 28 Maximum TX power [W] 128 200 200 GoB\_1: 2x12 Number of beams in vertical and 2x12 2x25 horizontal direction GoB\_2: 6x12

*Table 3-3 Antenna array configurations.* 

The 3D radiation characteristics showing all possible radiation beams are shown on Figure 3-6. These characteristics are the same for both polarizations.

User terminals, equipped with a single omnidirectional antenna, are randomly distributed within the cell. The user population is comprised of 20% outdoor terminals and 80% indoor terminals, with the latter situated in buildings ranging from 4 to 8 floors in height. A separate scenario, detailed in Figure 3-6 Cumulative 3D radiation patterns of all beams generated for different mMIMO setup, considers taller buildings of 15 to 20 floors.

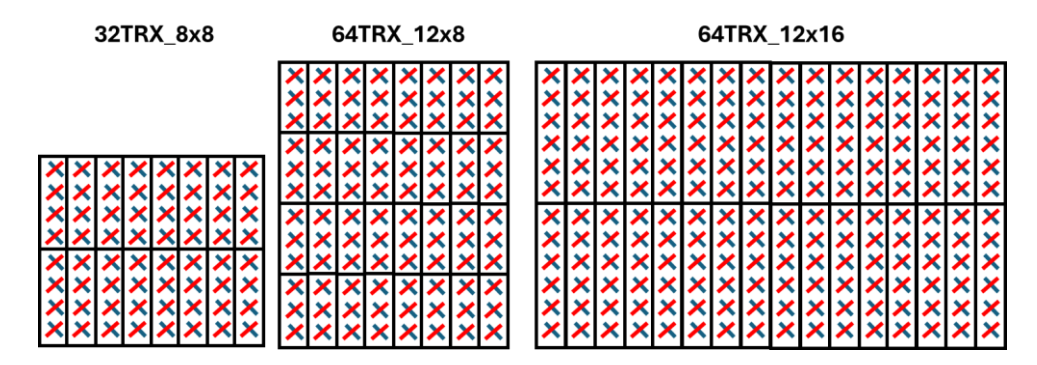


Figure 3-5 Antenna Array configurations used in simulations.

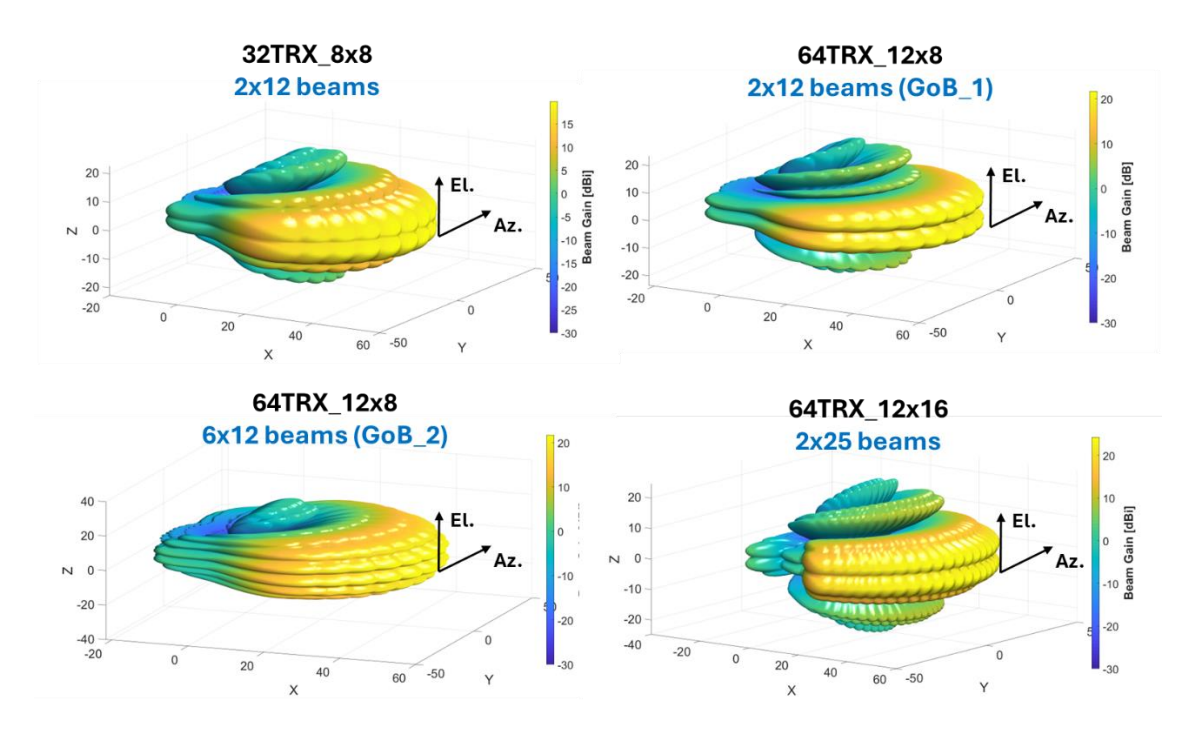


Figure 3-6 Cumulative 3D radiation patterns of all beams generated for different mMIMO setup.

The number of concurrently served terminals (K) varies from 1 to 8, while the duration of individual calls (D) ranges from 10 to 360 seconds. A multiantenna system enables simultaneous service to multiple users through spatial multiplexing (MU-MIMO), employing distinct antenna beams with minimal cross-correlation (inter-beam interference). Each terminal transmits at full power and bandwidth (full buffer).

Terminals are served within a 6-minute timeframe. If the call duration (D) is less than 6 minutes, new terminal locations are randomly selected, and transmission is repeated for a period of D. This approach realistically models a system where the base station serves multiple users distributed around the cell.

The simulation assumptions are summarized in Table 3-4. To accommodate this dynamic scenario, the multiantenna system continuously scans and adjusts antenna beams, a process

modeled within the system simulator. To ensure statistically accurate results, simulations were repeated 50 to 100 times.

Table 3-4 Main simulation assumptions.

Parameter	Value	
Channel model	3GPP 38.901 Urban Macro (UMa)	
Carrier frequency	3.5 GHz	
Channel bandwidth	20 MHz	
Sub-carrier spacing	30 kHz	
Gain of BS single antenna element	5.2 dBi	
Beamforming type	GoB	
Electrical down-tilt of BS antenna pattern	5°	
TDD duty cycle for DL	0.75	
Height of BS antenna array centre	25 m	
No. of cells / No. of sectors	7 / 21	
Inter-site distance	500 m	
Type of UE antenna	2 Omnidirectional (one per polarization)	
UE distribution	80% indoor, uniform distribution between floors (max. number of floors 4 to 8)	
No. of simultaneously served UEs	1, 2, 5, 8	
UE serving time	10, 60, 360 s	
Traffic type	Full buffer	
The actual max approach averaging time	6 min	

#### 3.2.2 Simulation results and discussion

Figure 3-7 and Figure 3-8 present simulation results for base station setup 64TRX\_12x8, illustrating the distribution of normalized radiated power. This metric represents the ratio of average radiated power (averaged over a 6-minute period) to the maximum radiated power of the base station. The results are presented for the direction of greatest radiation, which corresponds to the highest potential exposure to electromagnetic fields. For the scenarios considered, this direction exhibits an azimuth angle of -5° and an elevation angle of -5°. The azimuth angle is attributed to the antenna beamwidth the highest gain being located in this direction. This is due to its proximity to the antenna symmetry direction (broadside), where the antenna array achieves maximum gain. The -5° offset arises from the closest beam within the antenna beam set being located at this angle. Conversely, the elevation angle of -5° is a consequence of the antenna being deployed above the buildings where user terminals are located. Consequently, the beam from the second row of antenna beams, with an elevation of -5°, is most frequently selected.

Figure 3-7 demonstrates the impact of the number of simultaneous users served by multiple antenna beams on the normalized radiated power of the 64TRX\_12x8 base station. As the number of terminals increases, the average radiated power decreases because transmit power needs to be shared between more beams serving different UEs. Conversely, Figure 3-8 illustrates the effect of drop time to a single terminal on the normalized radiated power. A decrease in drop time leads to a reduction in normalized radiated power. This is because shorter drop times result triggers new UEs positions and more frequent antenna beam switching within the 6-minute observation period.

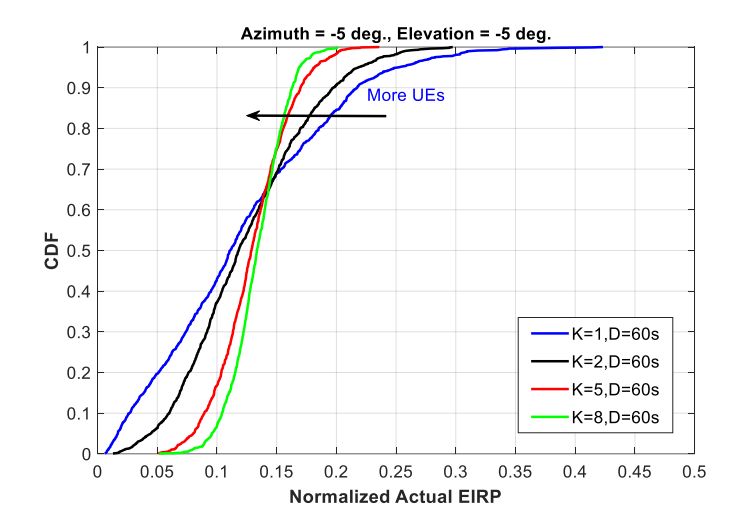


Figure 3-7 Simulation results - CDF of normalized actual EIRP for BS  $64TRX\_12x8$  (GoB\_1) for K=1, 2, 5, 8 and D=60 s showing the impact of number of simultaneously served terminals.

It is noteworthy that for all values of K (number of simultaneous users) and D (transmission time), the normalized radiated power remains below 1. This indicates that the maximum radiated power approach may not be an effective method for analyzing EMF exposure from multiantenna systems. Both graphs reveal that increased variation in antenna beam switching, characterized by higher K values and lower D values, results in reduced exposure to electromagnetic fields from multiantenna systems.

As per IEC 62232 guidelines [15], the  $F_{PR}$  power reduction factor is determined from the 95<sup>th</sup> percentile of the normalized radiated power distribution. Figure 3-9 presents a comparison of these values for various multiantenna systems simulated.

The analysis reveals an inverse relationship between antenna size and the  $F_{PR}$  factor; larger antennas exhibit lower  $F_{PR}$  values. This factor demonstrates variability across different scenarios and configurations. Notably, for realistic telecom traffic scenarios ( $K \ge 2$  and  $D \le 60$ s), the  $F_{PR}$  factor remains relatively consistent at -6.6 to -8.2 dB for the 32TRX\_8x8 and 64TRX\_12x8 multiantenna systems. Conversely, the 64TRX\_12x16 system exhibits a lower  $F_{PR}$  range of -9.2 dB to -11.5 dB.

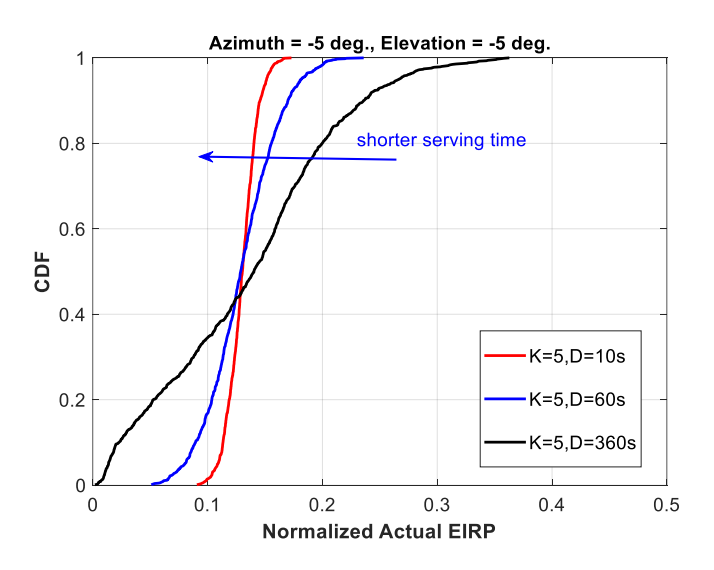


Figure 3-8 Simulation results - CDF of normalized actual EIRP for BS  $64TRX\_12x8$  (GoB\_1) for K=5 and D=10, 60, 360 s showing the impact of serving time.



Figure 3-9 Simulation results - Power reduction factors  $F_{PR}$  for different mMIMO setup.

These findings indicate a significant reduction in average radiated power compared to the theoretical maximum approach employed in conventional methods. Consequently, the compliance area can be reduced by approximately 40-50% for the 32TRX\_8x8 and  $64TRX_{12x8}$  antennas (for  $K \ge 2$  and  $D \le 60s$ ). While the antenna systems differ, the higher transmit power utilized in the  $64TRX_{12x8}$  system contributes to similar results. For the  $64TRX_{12x16}$  antenna, the compliance area reduction is estimated at 25-35%.

Illustratively, the compliance distance for a 64TRX\_12x16 base station with parameters outlined in Table 3-5 is 27.7 meters in case of traditional maximum transmit power approach. However, employing the actual maximum approach with the estimated power reduction factor reduces this distance to 7.1-9.7 meters, contingent upon the D and K parameters.

It has been observed that the F<sub>PR</sub> values for the 32TRX\_8x8 and 64TRX\_12x8 antennas are very similar. This is due to the scenario where there are only two beam rows in the elevation and relatively low buildings where the terminals are located. Consequently, the most significant beam switching dynamics are observed in the horizontal plane. As both antennas possess an

equal number of antenna elements in this plane, the resulting performance characteristics are comparable.

The scenario was modified by significantly increasing the maximum number of floors to values between 15 and 20 and using 6 instead of 2 beam rows in the antenna beam set (GoB\_1 and GoB\_2 in Table 3-3). The results are presented in Figure 3-10, where it can be observed that despite increasing the number of beams in the elevation when we have lower buildings, they do not significantly affect the change in normalized radiated power, as the probability of selecting beams from additional rows is low. Only when users are located on higher floors will these beams be selected much more frequently, and the greater variability of beam switching will result in a decrease in EMF exposure. This means that in the overall analysis, the scenario for which exposure assessment occurs and the number of antenna beams in the two planes are very important.

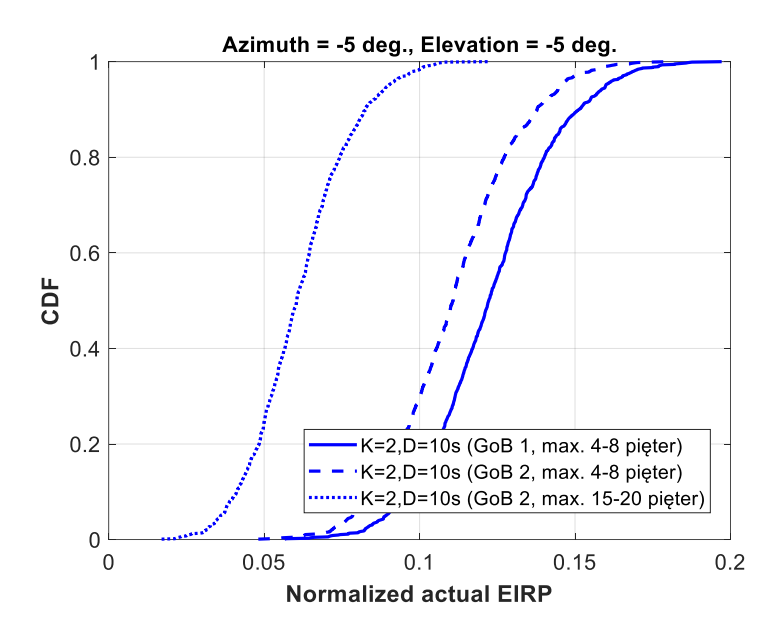


Figure 3-10 Simulation results - CDF of normalized actual EIRP for mMIMO 64TRX\_12x8 setup for scenarios with different building heights.

It is interesting to present the simulation results in the form of a cumulative distribution function of the average antenna gain as in Figure 3-11 for one of the cases with K=2 and D=10s. For comparison, a graph of the gain of a typical sector antenna with a value of 15 dBi has been added there. This is a constant value because this type of sector antenna does not use dynamic beamforming. Comparing the gain of the sector antenna with the average gain of multiantenna systems, their value may be slightly higher or even lower. Focusing on the 95<sup>th</sup> percentile of this average antenna gain, it can be seen that this value is much lower than the maximum gain of these antenna systems, e.g., the 95<sup>th</sup> percentile of the average gain of the 12x16 antenna is only 16.8 dBi, while the maximum gain of this antenna is as high as 28 dBi.

The actual maximum approach implemented in mMIMO base stations significantly reduces the compliance distance. This Section presents an example calculation of compliance distance for different mMIMO setups in Table 3-5. The calculations were made for K=2 and

D=60s (chosen  $F_{PR}$ ), which represents a conservative assumption of traffic, as in real networks, beams switch more frequently (even every 1 ms slot). However, this approach provides an additional margin for operation.

As observed, the compliance distance can be reduced by more than 50%. In the case of the largest antenna array, 64TRX\_12×16, the compliance distance with the actual maximum approach is only 35% of that calculated with the maximum theoretical approach. A compliance distance of around 10 m provides significantly more flexibility in deploying mMIMO BS, particularly in dense urban environments.

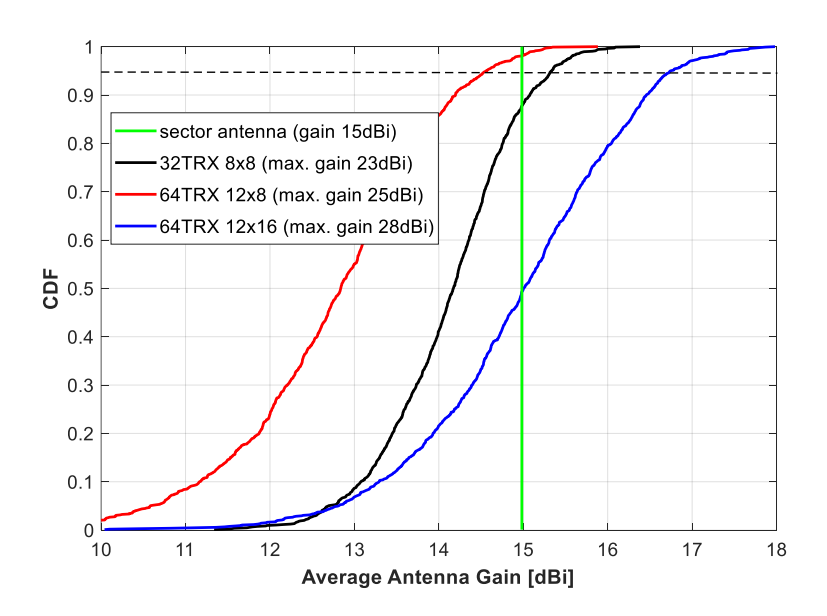


Figure 3-11 Simulation results - CDF of average antenna gain for different antenna configurations.

Table 3-5 Compliance distance calculated with maximum EIRP and actual EIRP approaches  $(F_{PR} \text{ for } K=2, D=60s).$ 

mMIMO setup	Compliance distance [m] Maximum EIRP	Compliance distance [m] Actual EIRP
32TRX_8×8	12.8	6
64TRX_12×8	19.6	9.2
64TRX_12x16	27.7	9.7

# 3.3 The evaluation of actual EMF exposure from base station operating in millimeter wave frequency band with GoB beamforming

#### 3.3.1 Introduction

Base stations operating in the mmWave frequency band are deployed as small cells in Urban Micro (UMi) environments, where the BS antenna height is typically below rooftops. The frequency bands allocated for 5G systems in this range primarily fall within the 24 to 40 GHz spectrum.

Due to significant penetration losses and signal blockage, mmWave deployments are primarily suited for outdoor or indoor coverage, but do not readily provide outdoor-to-indoor connectivity. Consequently, mmWave cells are characterized by smaller sizes and higher density. These cells coexist in close integration with 5G deployments operating below 6 GHz, as well as with 4G networks.

To mitigate the effects of higher path loss and shorter range, 5G mmWave systems utilize beamforming and beam steering techniques. These techniques employ complex antenna arrays that direct high-gain beams towards user devices, either in a static grid pattern or through more sophisticated beamforming mechanisms.

The mmWave BSs typically employ an analog architecture with one transceiver per polarization (two TRX in total) connected to the antenna array. Beamforming is achieved through analog phase shifters. The preference for analog architecture stems from the large bandwidth available in mmWave bands, such as the 400 to 800 MHz range. This wide bandwidth necessitates the use of costly analog-to-digital converters (ADCs) and digital-to-analog converters (DACs), leading to higher power consumption. Additionally, the small cell size results in a limited number of UEs within the coverage area of a mmWave BS. This factor makes a digital architecture, which allows for the generation of multiple beams, less essential. Fast beam switching and reliable beam steering algorithms are sufficient for current mmWave 5G system applications.

This chapter focuses on analyzing the electromagnetic field exposure from mmWave BSs operating at 28 GHz.

### 3.3.2 Simulation assumptions

The mmWave base station equipped with an 8x12 antenna array, as depicted in Figure 3-12, was modeled within the SLS system. The simulation assumptions are detailed in Table 3-6. The small cell, with the mmWave BS installed at a height of 10 meters, was modeled. The system operated in the 28 GHz band, utilizing an OFDM subcarrier spacing of 60 kHz and a full bandwidth of 100 MHz.

The analog architecture utilized in this scenario produces two cross-polarized beams in the same direction within a single time slot. This necessitates rapid beam switching when multiple

UEs require simultaneous service. In the simulation, the antenna beam is switched to different directions after intervals of D=1, 10, or 60 seconds. This assumption is considered conservative, as it provides an additional margin for the estimated EMF exposure.

The GoB comprises  $2\times30$  beams per polarization, as illustrated in Figure 3-13.

User equipment's are randomly distributed, with 90% located in outdoor areas and 10% in indoor areas. This distribution reflects the low probability of serving UEs radiating an outdoor-to-indoor propagation path.

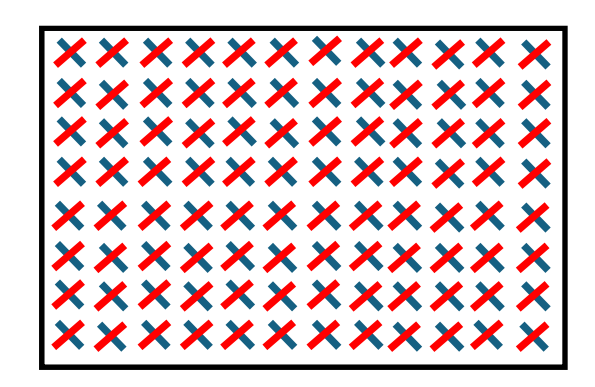


Figure 3-12 The mmWave antenna array layout.

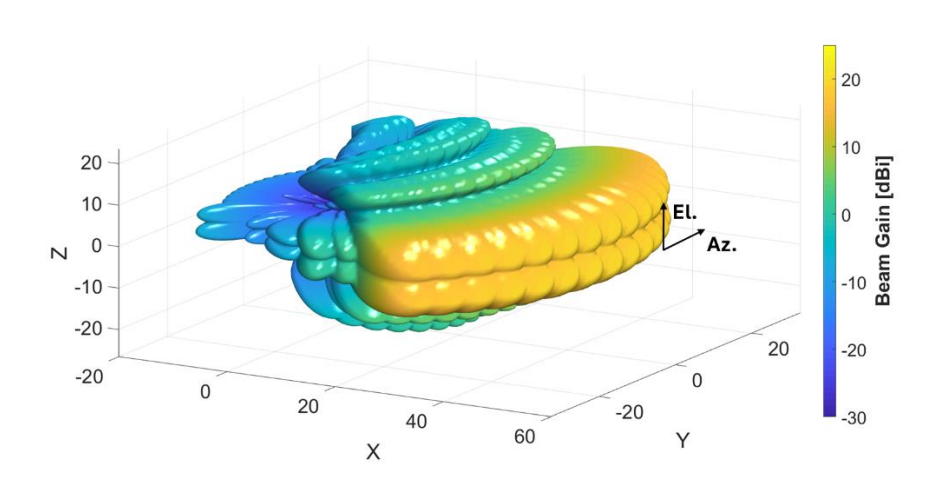


Figure 3-13 Cumulative 3D radiation patterns of all beams of mmWave BS.

*Table 3-6 Main simulation assumptions.* 

Parameter	Value	
Channel model	3GPP 38.901 Urban Micro (UMi)	
Carrier frequency	28 GHz	
Channel bandwidth	100 MHz	
Sub-carrier spacing	60 kHz	
Max total Tx power of BS (without losses)	32 dBm	
No. of TRx	2	
Gain of BS single antenna element	3.2 dBi	
Configuration of BS antenna array per polarization (VxH)	8×12	
Beamforming type	GoB	
Number of beams in vertical and horizontal	2×30	
direction	per polarization	
Maximum antenna gain	23 dBi	
Electrical down-tilt of BS antenna pattern	0°	
TDD duty cycle for DL	0.75	
Height of BS antenna array centre	10 m	
No. of cells / No. of sectors	7 / 21	
Inter-site distance	200 m	
Type of UE antenna	2 Omnidirectional (one per polarization)	
UE distribution	80% indoor, uniform distribution between floors (max. number of floors 4 to 8)	
No. of simultaneously served UEs	1	
UE serving time	1, 10, 60 s	
Traffic type	Full buffer	
The actual max approach averaging time	6 min	

### 3.3.3 Simulation results and discussion

The actual EMF exposure was evaluated through system-level simulations. The normalized actual EIRP exposure is presented in Figure 3-14.

The simulations reveal a very low EMF exposure from the mmWave BS which decreases with the drop time (beam switching time). Faster beam switching leads to a lower average EMF exposure because the rapid beam direction changes result in a reduced average EIRP in analyzed direction.

The  $F_{PR}$  coefficient, depicted in Figure 3-15, ranges from -6.4 to -9.9 dB. Applying the actual EMF exposure with this  $F_{PR}$  significantly reduces the compliance distance (2-3 times).

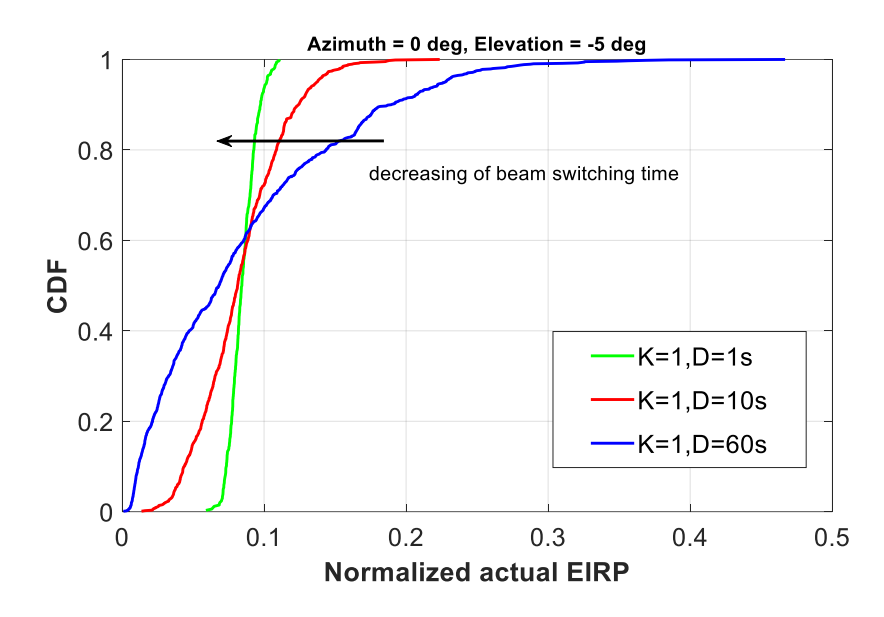


Figure 3-14 Simulation results - CDF of normalized actual EIRP from mmWave BS.

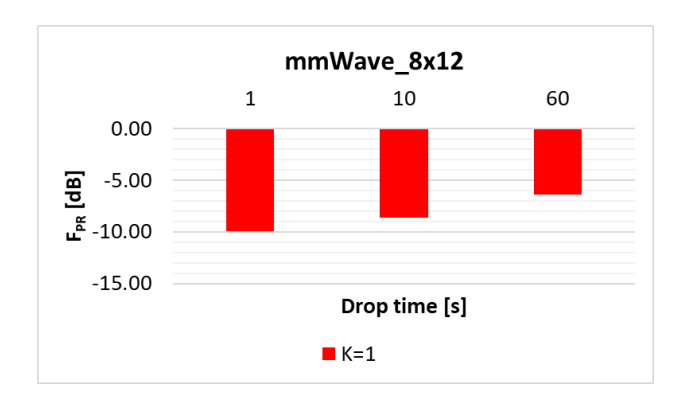


Figure 3-15 Simulation results - Power reduction factors  $F_{PR}$  for mmWave BS.

### 3.4 Impact of averaging time on actual EMF exposure

### 3.4.1 Introduction

The recommended averaging time for whole-body exposure measurements in the International Commission on Non-Ionizing Radiation Protection was significantly increased in the latest ICNRIP:2020 guidelines [12], compared to the ICNRIP:1998 guidelines [24]. A summary of these values is presented in Table 3-7 below.

Table 3-7 Averaging time comparison in ICNRIP:1998 and ICNRIP:2020.

	ICNIRP 1998	ICNIRP 2020
AVERAGING TIME FOR WHOLE-BODY EXPOSURE	6 MIN (400 MHz – 10 GHz) 68/(F <sup>1.05</sup> ) (10 GHz – 300 GHz) - FOR EXAMPLE 2 MIN FOR 28GHz	FIXED TO <b>30 MIN</b> UP TO 300 GHZ
AVERAGING TIME FOR LOCAL EXPOSURE	<b>6 MIN</b> OR LESS DEPENDING ON FREQUENCY	Fixed to <b>6 min</b> up to 300 GHz

The averaging time for whole-body exposure was increased from 6 minutes to 30 minutes for sub-GHz frequency bands designated for 5G systems. For mmWave frequency bands, the averaging time was also changed, for example, from 2 minutes to 30 minutes for the popular 28 GHz 5G frequency band.

The significantly higher averaging time of 30 minutes implies that, from a beamforming perspective, a greater number of beams are scanned, which is expected to reduce average electromagnetic field exposure.

The impact of averaging time was tested in a simulator for mMIMO array with 32 transceivers and an 8x8 antenna configuration (32TRX\_8x8 BS from Section 3.2) for sub-GHz frequencies and for a mmWave base station configuration from Section 3.3 above.

### 3.4.2 Impact of averaging time for actual EMF exposure in sub-GHz frequency band

The mMIMO base station configuration described in Section 3.2 was employed for the simulations. This BS operates at 3.5 GHz and utilizes a GoB beamforming scheme with 48 beams (24 in the horizontal and 2 in the vertical directions). The simulation assumptions remain consistent with those outlined in Table 3-4, with the exception of the averaging time, which was increased to 30 minutes.

Figure 3-16 presents the distribution function of normalized actual EIRP, illustrating the results for both 6-minute and 30-minute averaging times with K=5 served UEs.

The analysis reveals that while the median values remain unchanged, the 95th percentile values are influenced by the extended averaging time.

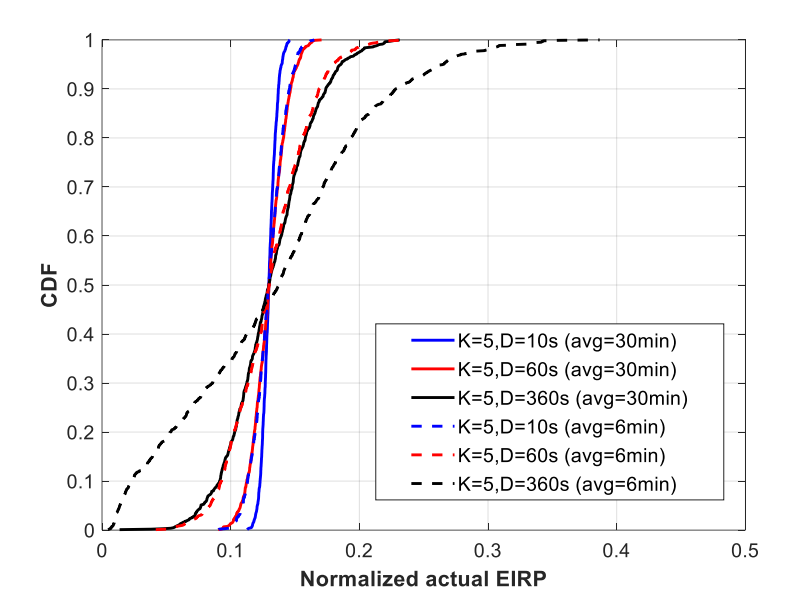


Figure 3-16 Simulation results - CDF of normalized actual EIRP for different averaging time.

The power reduction factor, derived from the 95th percentile of the CDF, is depicted in the bar plot of Figure 3-17 for K=2 and 5.

The impact on the power reduction factor is approximately 0.5-1.5 dB when the averaging time is increased from 6 minutes to 30 minutes. Notably, the reduction in  $F_{PR}$  is more pronounced for use cases with fewer simultaneously served UEs and longer UE scheduling times. This observation can be attributed to the fact that longer observation periods for larger UE drops result in a greater number of new positions compared to shorter observation times.

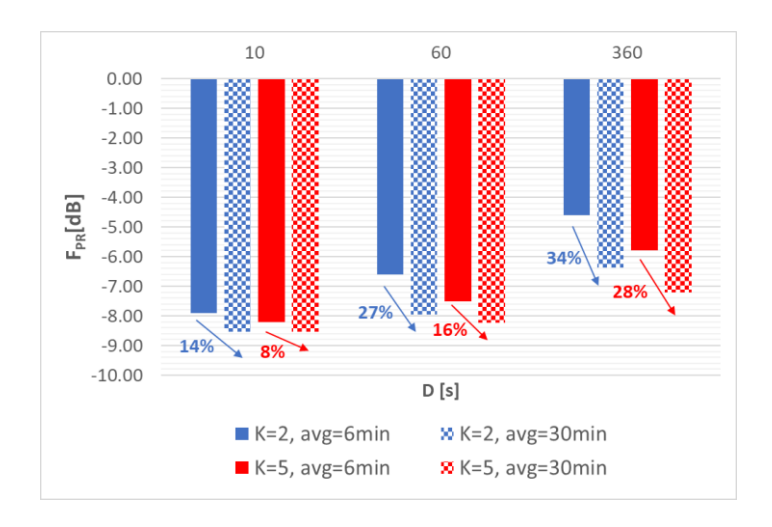


Figure 3-17 Simulation results - Impact of averaging time for power reduction factor.

### 3.4.3 Impact of averaging time for actual EMF exposure in mmWave frequency band

For mmWave simulations, an identical base station setup operating in the 28 GHz band, as described in 3.3, was employed. Simulations were conducted with a drop time D = 10 seconds and averaging times of 2, 6, and 30 minutes.

The impact of averaging time on the normalized actual EIRP is presented in Figure 3-18, and the corresponding power reduction factors are listed in Table 3-8.

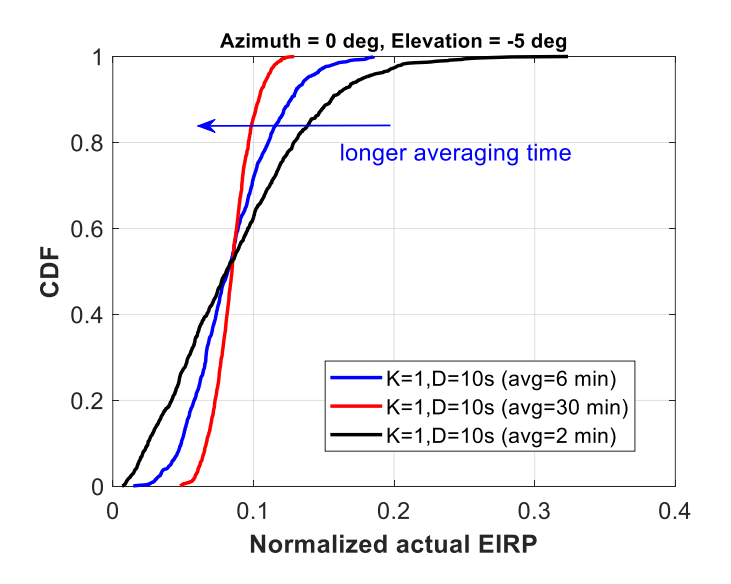


Figure 3-18 Simulation results - Impact of averaging time for distribution of actual EIRP.

The observed behavior aligns with the findings described in Section 3.2. Increasing the averaging time maintains the median value while reducing the 95<sup>th</sup> percentile. This difference is particularly pronounced for averaging times of 2 minutes (ICNIRP: 1998 recommendation) and 30 minutes (ICNIRP: 2020 recommendations).

Table 3-8 Simulation	results -	ımpact of	averaging	time for $F_{PR}$ .

Avg. time [min]	$F_{PR}$ [dB]
2	- 7.5
6	- 8.6
30	- 9.6

At 28 GHz, the impact on the  $F_{PR}$  is approximately 2 dB when the averaging time changes from 2 minutes to 30 minutes. This impact would be more significant at higher mmWave frequencies. For instance, the difference between 0.8 minutes and 30 minutes at 70 GHz would be more pronounced.

### 3.5 Conclusions

In this chapter the actual EMF exposure for mMIMO antennas with GoB beamforming were analyzed. A statistical approach, employing a realistic model of a multiantenna system, has been employed to assess actual EMF exposure. This model incorporates factors such as radio wave propagation, base station and terminal distribution, number of beams in GoB set and telecommunication traffic. The results indicate that actual EMF exposure from such systems is significantly lower than estimated based on maximum radiated power approach and is highly dependent on system parameters and scenario. The results demonstrate that even for currently deployed sectoral antennas with 4x4 MIMO capability, lower exposure levels can be observed near the antenna due to the precoding effect.

The determined power reduction factor enables a substantial reduction in RF exposure compliance boundary around antennas (more than 50 %). However, due to the dynamic nature of these systems, occasional exceedances of established RF exposure compliance boundary may occur. To address this, base stations should be equipped with a mechanism for controlling the actual power or EIRP, as recommended by the IEC 62232 standard [15]. Nonetheless, simulation results suggest that EIRP control will be implemented infrequently and primarily as a preventive measure.

Power reduction factors established based on 6-minute time averaging for sub-GHz and 2-minute time averaging for 28 GHz are conservative when compared to the 30-minute whole-body averaging interval specified in the ICNIRP 2020 guidelines. Consequently,  $F_{PR}$  documented in existing literature remain applicable for assessing compliance with ICNIRP 2020 whole-body limits.

This finding could also have implications for actual EIRP control features. Adjusting counters to reflect 30-minute averaging should reduce the frequency of EIRP control triggering.

The 6-minute averaging, as recommended in IEC 62232 [15] and used in IEC TR 62269 case studies [14], is employed in all simulations presented in this thesis.

The part of research studies presented in this chapter was published in [25].

# 4. Statistical analysis of actual EMF exposure from Massive MIMO base stations serving moving terminals

### 4.1 Introduction

This chapter investigates the impact of user equipment movement on radio frequency electromagnetic field exposure assessments for mMIMO base stations, utilizing the actual maximum approach described in IEC 62232 [15].

Current research primarily focuses on static UE scenarios for channel modeling and RF EMF exposure evaluation [6][20][26][21][17]. However, in real-world operation, UEs are dynamic, leading to frequent beam changes and adaptations. This study introduces a computational model that accounts for UE movement, analyzing its influence on the range of applicable power reduction factors compared to static UE models.

As UEs change position, beamforming weights are updated, resulting in beam switching or shaping, potentially altering the spatial distribution of EMF exposure. This can significantly impact compliance boundary estimation.

This study explores a novel approach that incorporates realistic UE movement into RF EMF exposure evaluation, comparing its impact to static UE scenarios. Specifically, it investigates the influence of UE movement on the estimation of  $F_{PR}$ , as defined in IEC 62232 [14]. The study also analyzes the actual RF EMF exposure at the UE position across various simulation scenarios.

### 4.2 Modeling of moving terminals

The static UE modeling method, as described in [6] and illustrated in Figure 4-1, utilizes a 6-minute averaging time (T) and Large-Scale Parameters (LSPs). These LSPs include path loss, shadow fading, Ricean K factor, delay spread, and angular spreads, as defined in the 3GPP TR 38.901 channel model [19].

In the static UE model, at the beginning of each simulation drop (N), K UEs are randomly positioned within each cell. These UEs remain stationary throughout the drop duration (D) until the next UE drop (N+1). At this point, new random positions are generated for the K UEs. This model simulates the arrival of new UEs randomly distributed within the cell, as depicted in Figure 4-2.

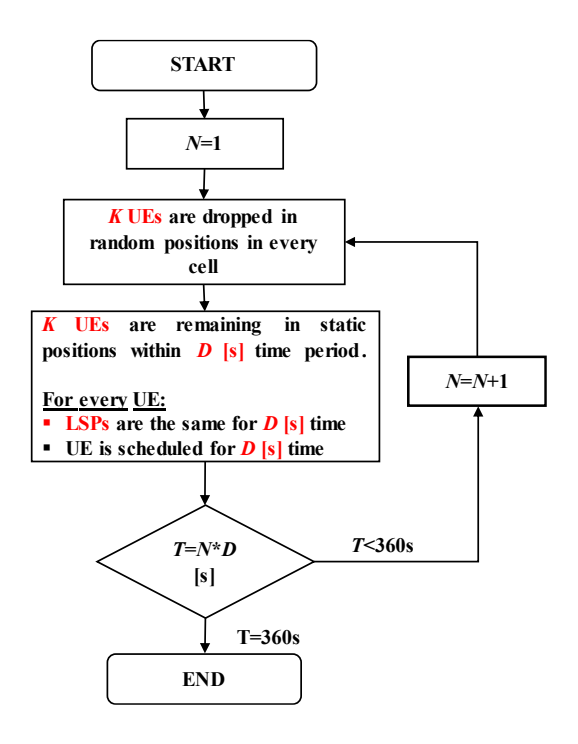


Figure 4-1 Flow chart of static UE model.

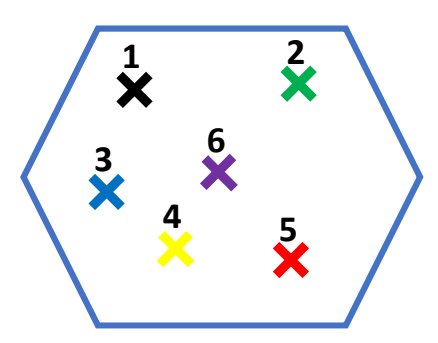


Figure 4-2 Example of static UE model - different colors show new position of UE (K=1) after every drop D=60s.

The movement of UEs is modeled as described in Figure 4-3. At the start of each simulation drop, Gaussian distributions are generated for the X and Y positions of the UEs. The initial positions are randomly selected, ensuring that exactly K UEs are active within the same cell. During the time period D, UEs move within the boundaries of 7 cells. Each UE moves in a single direction with a step size of 1 meter at a speed of 3 km/h. After traversing a distance of 10 meters (D\_turn), representing the mean path length before a turn, the UE randomly selects a new direction and continues moving. The impact of varying D\_turn values is analyzed in the subsequent Section.

The simulator employs a spatial consistency procedure for the LSPs, aligning them with the UMa channel model [19]. New LSPs are generated after every 1 meter of UE movement, maintaining spatial consistency according to [19]. This includes shadowing, angular spreads (for departure and arrival, in elevation and azimuth), delay spread, and Rician K factor for Line-

of-Sight (LOS) conditions. This approach ensures realistic modeling of radio channel propagation parameters, which do not change significantly over small distances.

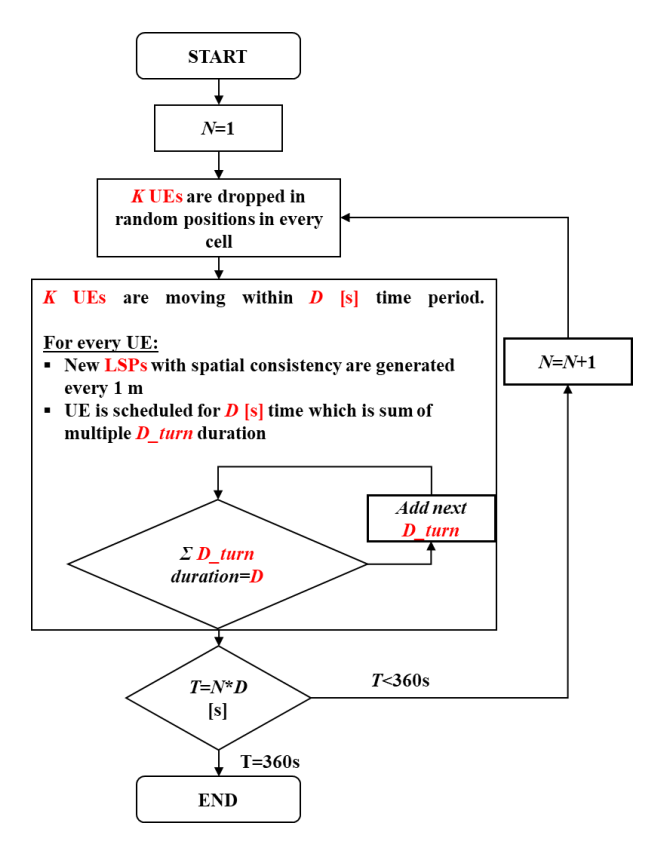


Figure 4-3 Flow chart of moving UE model.

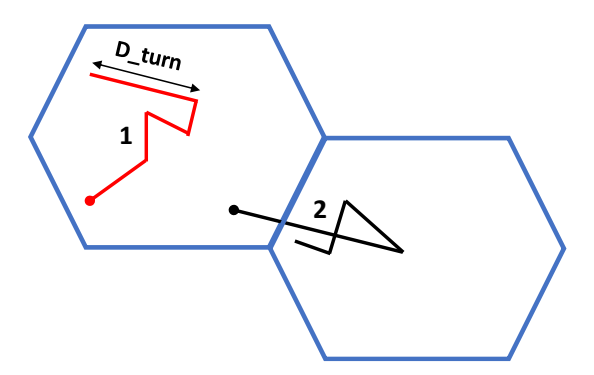


Figure 4-4 Example of moving UE model. The 2 UEs (K=2) are starting to move in the same cell, one UE performs handover to another cell during moving.

Terminals are assigned to indoor or outdoor positions and LOS or Non-Line-Of-Sight (NLOS) conditions based on the distribution specified by the UMa channel model. This assignment remains constant during the random walk. UEs always move on the same floor. When a moving UE reaches the boundary of the 7-cell area, it bounces and continues moving in a random direction. The "wrap around" technique for moving UEs was also tested, but it did not significantly impact the results. Moving UEs can transition between serving cells through a handover procedure. Figure 4-4 illustrates examples of random trajectories for moving UEs.

### 4.3 Simulations assumptions

To accurately reflect the impact of real radio channel characteristics on the results of the F<sub>PR</sub> modeling, the SLS tool described in Chapter 2 was employed. This tool utilizes a statistical 3D spatial model of radio wave propagation, adhering to the 3GPP 38.901 Urban Macro (UMa) scenario [19]. The application of this spatial channel model enables realistic modeling of signal fluctuations experienced by moving UE and accurately captures the significant impact of power angular spread on the effective gain of directional antennas [27][28].

Simulations were conducted using the Monte Carlo technique for a cellular sub-network comprising seven adjacent cells. Each cell is equipped with three sectors, each containing a mMIMO BS. These BSs are positioned at a height of 25 meters with an inter-site distance of 500 meters between them. The system operates at a frequency of 3.5 GHz with a 20 MHz bandwidth and a configured maximum transmitted power of 51 dBm.

Simulations were performed for an 8x8 antenna array consisting of cross-polarized elements and 32 transceivers connected to sub-arrays, as depicted in Figure 4-5. The maximum gain of this array is 23.2 dBi. The antenna array can generate 24 beams per polarization (48 in total within the GoB set, uniformly distributed at 120 degrees of azimuth opening angle and two elevation angles, as illustrated in Figure 4-6.

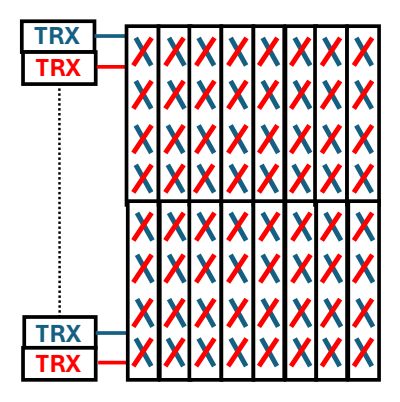


Figure 4-5 Antenna array model 8x8 with 32 TRXes.

Simulated UEs utilize a single cross-polarized omnidirectional antenna and are randomly distributed within a cell. Of these UEs, 20% are located outdoors and 80% indoors, residing within buildings whose heights are uniformly distributed with a maximum number of floors ranging from 4 to 8. The number of terminals served, K, is either 1, 2, or 5, and the duration of a single downlink (DL) connection, D, is 10, 60, or 360 seconds. The 360-second duration corresponds to the averaging time specified in ICNIRP-1998 [24] and IEEE C95.1 [29].

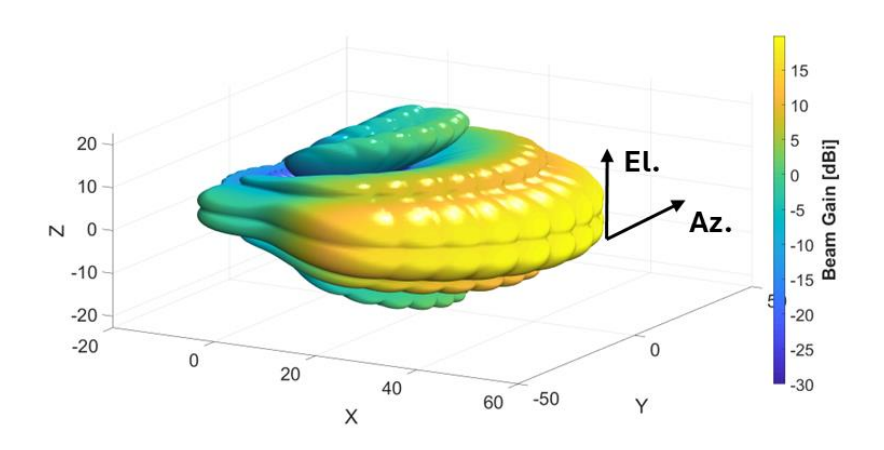


Figure 4-6 Cumulative envelope of beams.

A multiantenna system can serve multiple users simultaneously through spatial multiplexing by employing distinct antenna beams with minimal inter-beam interference. This study considers a configuration where BSs are fully loaded using the full-buffer traffic model [6]. Table 4-1 summarizes the key simulation parameters.

Table 4-1 Main simulation assumptions.

Parameter	Value	
Channel model	3GPP 38.901 Urban Macro (UMa)	
Carrier frequency	3.5 GHz	
Channel bandwidth	20 MHz	
Sub-carrier spacing	30 kHz	
Max total Tx power of BS (without losses)	51 dBm	
No. of TRx	32	
Gain of BS single antenna element	5.2 dBi	
Configuration of BS antenna array per polarization	8×8	
Beamforming type	GoB, 2x24 beams (V×H) per polarization	
Electrical down-tilt of BS antenna pattern	5°	
TDD duty cycle for DL	0.75	
Height of BS antenna array centre	25 m	
No. of cells / No. of sectors	7 / 21	
Inter-site distance	500 m	
Type of UE antenna	Omnidirectional	
UE distribution	80% indoor, uniform distribution between floors (max. number of floors 4 to 8)	
No. of simultaneously served UEs	1, 2 and 5	
UE serving time	10 s, 60 s and 360 s	
The actual max approach averaging time	6 min	

### 4.1 The analysis of impact of moving terminals on actual EMF exposure

To analyze the impact of mobile user equipment movement on actual electromagnetic field exposure, we focused on the scenario with maximum RF EMF exposure and compliance distance. In the vertical plane, outdoor UEs were positioned at street level, while indoor UEs were placed at a maximum height of 24 meters (floor height of 3 meters, maximum of 8 floors). The base station antenna height was 25 meters, exceeding the top floor height. This resulted in the selection of a beam row with a 5-degree elevation tilt. The boresight direction, characterized by the highest antenna gain, was aligned with the centers of two beams in the GoB set (-5° and +5° in azimuth). Consequently, maximum RF EMF exposure was observed in the directions of  $\phi_{max} = -5^{\circ}$  or  $5^{\circ}$  and  $\theta_{max} = 5^{\circ}$  for both static and mobile UE modeling approaches.

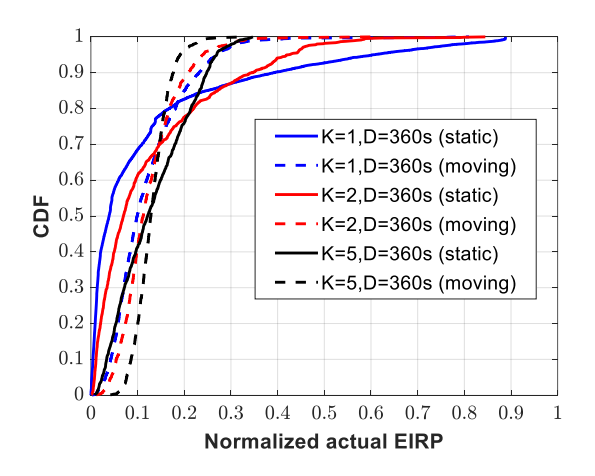


Figure 4-7 Simulation results - CDF of normalized actual EIRP – comparison of static and moving UE models (K=1, 2, 5 and D=360s).

Figure 4-7 presents the actual normalized EIRP, calculated as the average EIRP normalized to the maximum EIRP corresponding to the direction of highest RF EMF exposure. The CDFs in Figure 4-7 demonstrate that for percentiles above 80%, the normalized actual EIRP value is reduced with mobile UEs compared to the static UE model. Mobile UEs trigger beam switching more frequently than static UEs, leading to increased beam switching dynamics and a decrease in average EIRP in the analyzed direction.

Even in the most conservative scenario with a single UE served continuously for 6 minutes (K = 1 and D = 360 seconds), the  $F_{PR}$  determined from the 95<sup>th</sup> percentile of the actual EIRP decreased by a factor greater than 2 (from approximately 60% to 30% of the configured maximum EIRP). The  $F_{PR}$  values for different numbers of K UEs and serving time D = 360 seconds are summarized in Table 4-2. The results indicate that in all cases, the  $F_{PR}$  for the mobile UE model decreased within the range of -1.5 dB (for K = 5) to -3.5 dB (for K = 1).

The  $F_{PR}$  for various serving times, D, and all numbers of K UEs are depicted in Figure 4-8, Figure 4-9 and Figure 4-10. The difference between static and mobile UEs is less pronounced when the serving time is reduced. This is because with D < 6 minutes, static UEs occupy more positions during the same averaging time, triggering more frequent beam switching. For

instance, with D=10 seconds, static UEs change positions randomly 36 times during the averaging time.

Table 4-2 Simulation results - power reduction factor for different UE models.

K	UE model	D (s)	$F_{PR}$ (dB)
1	static	360	-2.2
1	moving	360	-5.7
2	static	360	-3.8
2	moving	360	-6.2
5	static	360	-5.7
5	moving	360	-7.2

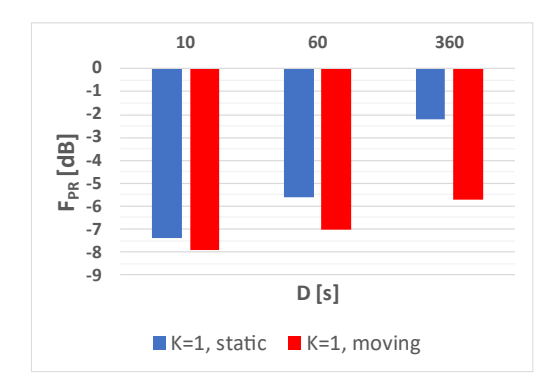


Figure 4-8 Simulation results -  $F_{PR}$  for K=1 and static and moving UE model.

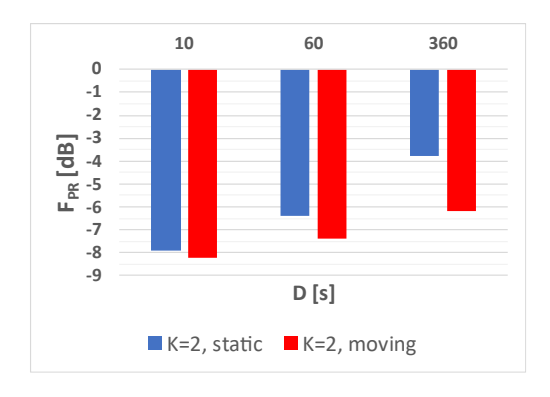


Figure 4-9 Simulation results -  $F_{PR}$  for K=2 and static and moving UE model.

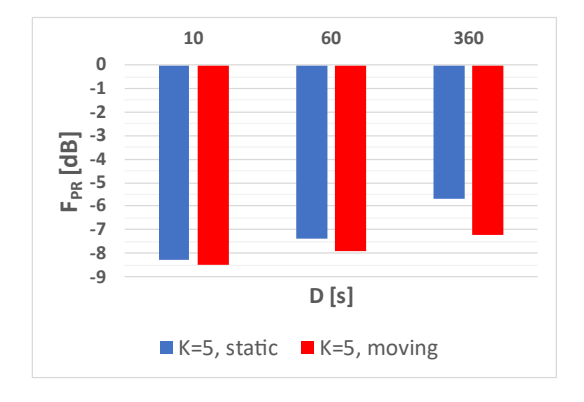


Figure 4-10 Simulation results -  $F_{PR}$  for K=5 and static and moving UE model.

The impact of the  $D_{turn}$  parameter, representing the mean length of a single UE path before changing direction, on  $F_{PR}$  was also investigated and is shown in Figure 4-11. The observed impact is minimal, indicating that with an increase in mean path length, the  $F_{PR}$  value decreases slightly, particularly for longer serving times D. Each UE moves in a straight line for a longer duration when D increases, leading to a higher probability of switching between beams from the GoB set and reduced RF EMF exposure. In the case of shorter mean path lengths, there are more frequent UE turns with a higher probability of selecting beams from a limited range. While every movement can trigger beam switching, this impact is minimal. Consequently, all simulations utilized a mean path length of 10 meters.

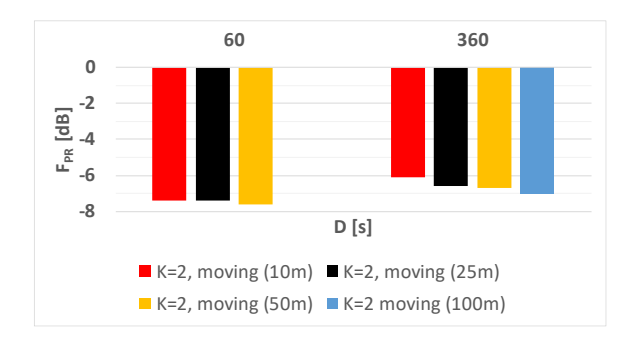


Figure 4-11 Simulation results - impact of the mean path length  $D_{turn}=10, 25, 50$  and 100m for K=2 and D=60 and 360s.

### 4.4 Evaluation of actual electric field of serving and nonserving terminals

This Section compares the simulated RF EMF exposure levels experienced by UE devices served and not served by the same BS during the simulation period. The actual EMF exposure is estimated for all UEs included in the simulation (with 3D distances from the BS ranging from 6 meters to 760 meters) based on the time-averaged electric field strength from all BSs and their active beams during the downlink transmission period, which is 360 seconds.

For served UEs, the results include electric field strengths contributed by beams from the BS scheduling transmission to that UE, as well as interfering beams from the same and surrounding BSs. For non-served UEs, the results only include electric field strengths from interfering beams from all BSs.

Figure 4-12 presents the actual total electric field strength levels observed for moving served UEs over a 6-minute averaging period, considering different numbers of simultaneously served UEs. The results indicate low levels of RF EMF exposure, with mean values ranging from 0.1 V/m to maximum values reaching 2.5 V/m. The number of served UEs (K) has a minimal impact on RF EMF exposure. However, as expected, the scenario with a single UE results in the highest total actual electric field strength values. This is because the transmitted power is shared among multiple beams when the BS serves multiple UEs, but the total RF EMF exposure also includes contributions from side lobes of other non-serving beams.

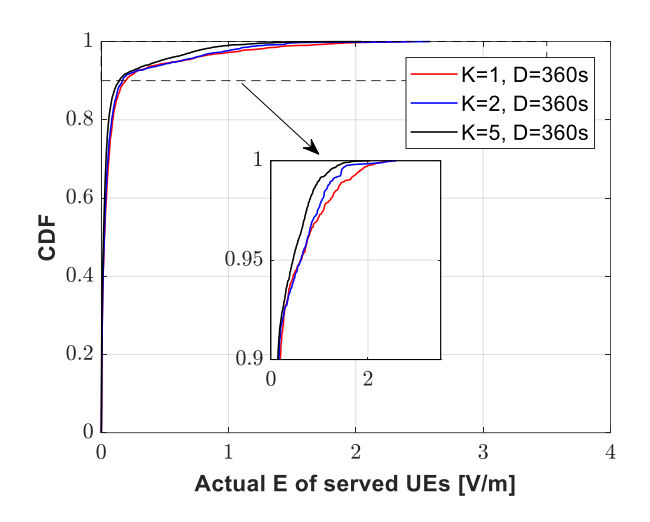


Figure 4-12 Simulation results - actual electric field strength for moving UE model – K=1, 2, 5 and D=360s.

Figure 4-13 presents the RF EMF exposure levels for moving non-served UEs, which are significantly lower than those observed for served UEs (as shown in the direct comparison in Figure 4-14). This is because BSs with mMIMO technology steer high-gain beams towards served UEs, while other positions are primarily exposed to contributions from side lobes and nulls of the beam pattern. In this case, RF EMF exposure increases with the number of UEs in the network.

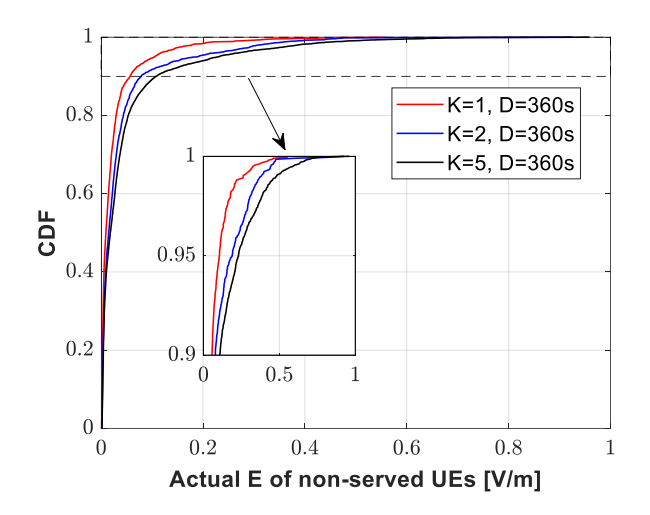


Figure 4-13 Simulation results - actual electric field strength for non-serving moving UE model - K=1, 2, 5 and D=360s.

Figure 4-15 provides an additional comparison of RF EMF exposure between static and moving scenarios for K = 1 and D = 360 seconds. While the mean and median values are similar, the maximum value of the average electric field strength is higher for static UEs (3.5 V/m) compared to moving UEs (2.5 V/m). This difference arises because path loss changes with each new position for moving UEs, whereas static UEs can experience a situation with low path loss and high gain, which remains relatively constant over the 6-minute serving time.

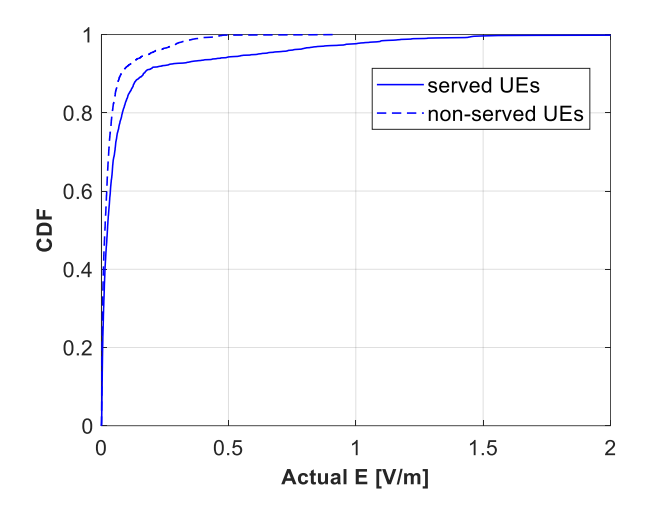


Figure 4-14 Simulation results - comparison of the actual electric field strength for served and non-served moving UE (K = 2, D = 360 s).

Figure 4-16 compares the actual RF EMF exposure of moving UEs located outdoors and indoors. As expected, indoor UEs experience lower exposure due to the attenuation of signals from the BS caused by the penetration loss of walls.

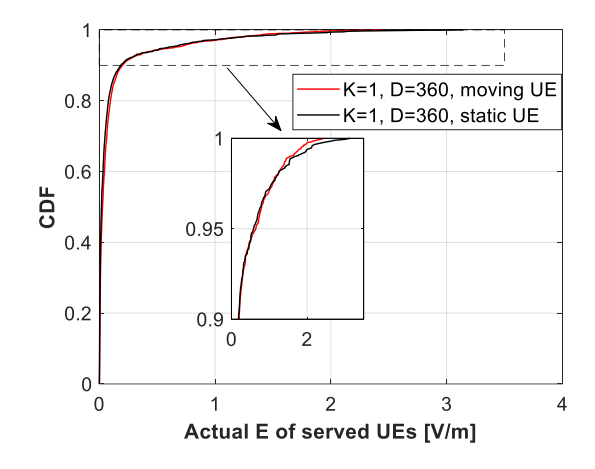


Figure 4-15 Simulation results - actual electric field strength for static and moving UE model,  $K=1,\,D=360s$ .

The modeled values of the actual electric field strength presented in this Section are well below the applicable RF EMF exposure limits for the public (e.g., 61 V/m as per [12]). These results were obtained under maximum traffic load conditions, with the 5G system operating in full buffer mode, where the total transmitted power is used continuously during the serving time. However, such a traffic profile is rare in real networks, meaning that RF EMF exposure is generally lower, as confirmed by experiments on real 5G networks [30][31][32][33][34] .

The measurement report presented in [35] indicates that the highest contribution to RF EMF exposure is generated by the mobile DL signal from the BS, compared to other sources such as uplink and broadcast signals. Additionally, exposure from 3.5 GHz DL is lower than exposure from BSs with non-beamforming antennas (800, 900, 1800, 2100, and 2600 MHz).

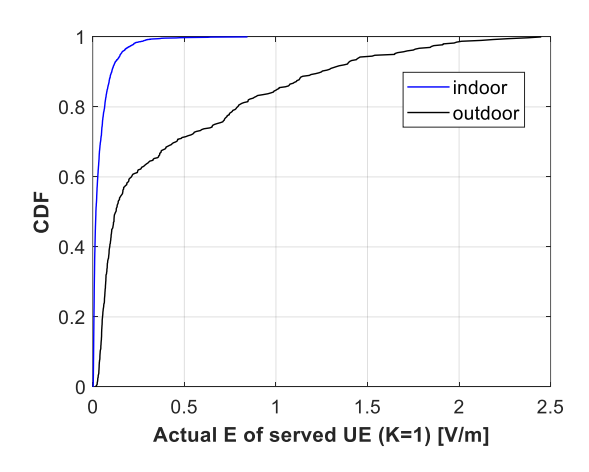


Figure 4-16 Simulation results - actual electric field strength for moving UE model, K=1, D=360s.

### 4.5 Conclusions

This chapter presents a novel method for modeling RF exposure from a mMIMO base station, incorporating channel modeling with moving user equipment devices. The method is grounded in statistical radio channel modeling principles outlined in 3GPP TR38.901, enabling accurate modeling of spatial consistency, which is crucial for analyzing radio propagation in closely spaced locations.

Simulation results demonstrate that the actual RF EMF exposure modeled with moving UEs is reduced compared to static UEs. When applying the actual maximum approach described in IEC 62232 [15], the modeled power reduction factor  $F_{PR}$  is observed to decrease within the range of -1.5 dB (K = 5) to -3.5 dB (K = 1) for a serving time (D) of 360 seconds. This reduction in  $F_{PR}$  can lead to smaller BS compliance distances when mMIMO BSs are deployed in areas primarily serving moving UEs.

The study's findings, particularly the  $F_{PR}$  values, can be valuable for network operators during RF EMF exposure assessments of massive MIMO BSs. These results have been included in IEC TR 62269:2025 [14] list of reference for  $F_{PR}$  modelling studies.

The proposed model for moving UEs holds also potential for application in other research studies within this field.

Furthermore, the study confirms that the actual RF EMF exposure levels in the locations of both served and non-served UEs remain well below the recommended RF EMF exposure limits, such as those established by the ICNIRP.

The research findings presented in this chapter were published in [36].

## 5. Impact of beamforming algorithms on the Actual EMF exposure from Massive MIMO base stations

### 5.1 Introduction

The initial deployment of 5G base stations primarily relied on the GoB algorithm, where beams directed towards user equipment locations are chosen from a predefined set. However, more sophisticated beamforming schemes have been adopted to meet the evolving requirements of the 5G system.

One prominent BF algorithm is eigenbeamforming (EBF), which offers significantly enhanced resolution in beam steering directions compared to GoB and can adapt to dynamic radio propagation conditions. Another BF scheme is eigenmode zero-forcing (EZF), which minimizes interference towards non-served UEs by creating nulls in the beam pattern. Both EBF and EZF algorithms demonstrate superior performance to GoB but necessitate increased signal processing capacity within the baseband modules of massive MIMO BS. These BF methods were introduced in Chapter 2. EBF and EZF techniques leverage multipath propagation, enabling the construction of UE-specific beams in multiple directions beyond the main lobes.

Figure 5-1 illustrates examples of beam patterns for GoB and EBF. In the case of GoB, a classical beam shape is generated from a massive MIMO base station, and the beamformer selects the optimal beam. For EBF, the precoding weights are dynamically adjusted based on the specific user equipment and radio channel characteristics, resulting in an irregular beam shape that adapts dynamically.

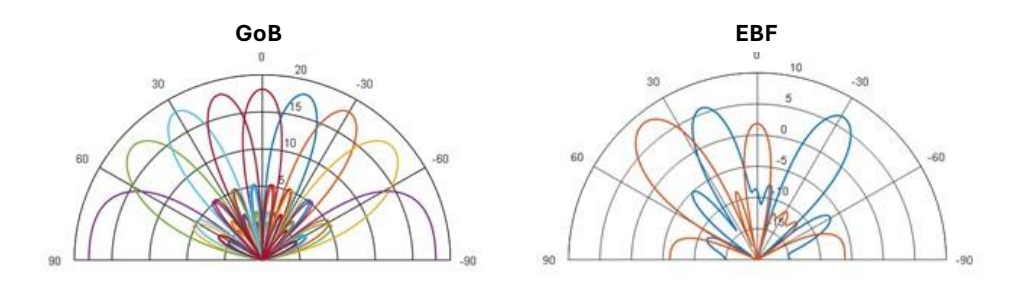


Figure 5-1 GoB beams and EBF example of beams (for 2 different UEs).

Figure 5-2 depicts GoB and EBF beam examples for one UE, considering a simplified radio channel with two strong multipaths of equal strength. It is observed that GoB selects a single beam from the grid, leading to a wider effective antenna pattern due to channel angular spread (discussed in detail in Section 8.3.1). Conversely, EBF utilizes measured uplink pilot signals to adjust beamforming weights, adapting to the specific radio channel. In the example, the resulting pattern consists of two strong lobes directed towards the multipaths. At the UE receiver, the EBF precoded signal transmitted through the channel is coherently summed to maximize the received signal level by leveraging the full array capability and its total gain.

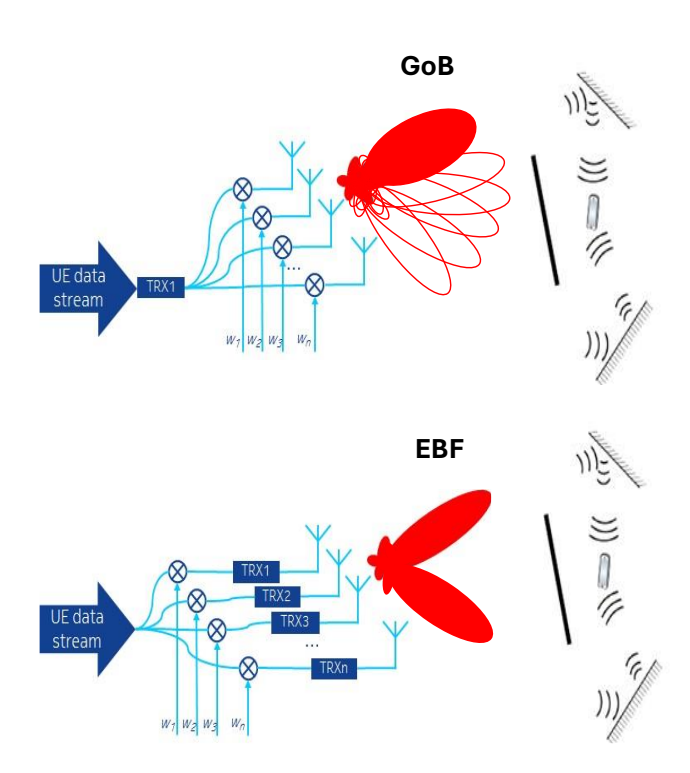


Figure 5-2 Difference between GoB and EBF work principle explained for simple multipath channel and resultant antenna pattern.

Figure 5-3 (2D) and Figure 5-4 (3D) present simulation results for more complex channels.

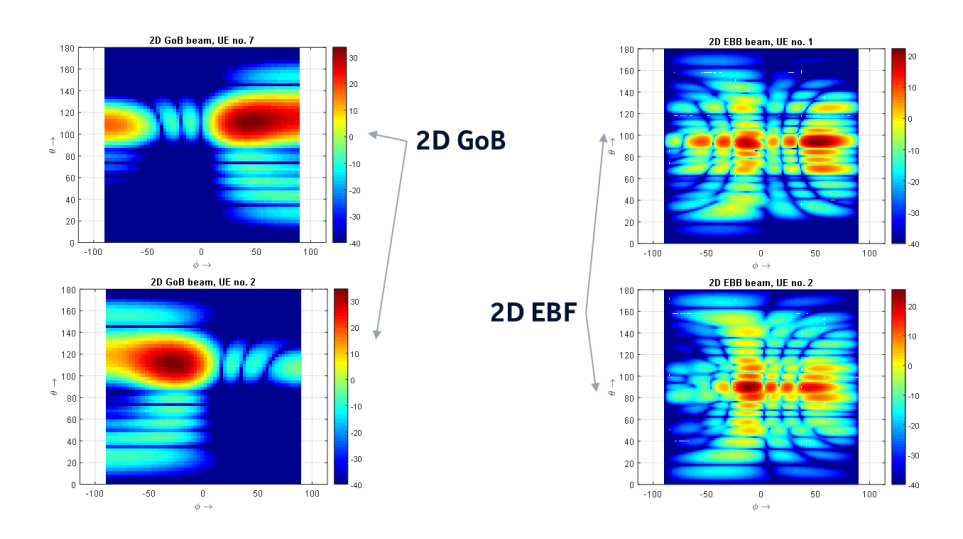


Figure 5-3 Calculated examples of 2D beam patterns (in contour plot format) resulting from the GoB and EBF algorithm for different UE cases.

Figure 5-3 displays 2D beam patterns generated by the GoB and EBF algorithms for different UEs. In the case of GoB, strong radiation is observed in specific directions where the single beam is pointing. EBF, due to its adaptation to the multipath radio channel, distributes radiation across space to cover the strongest multipaths.

The resulting beam can exhibit an arbitrary shape, with multiple beams covering various propagation paths, as illustrated in example in 3D format in Figure 5-4.

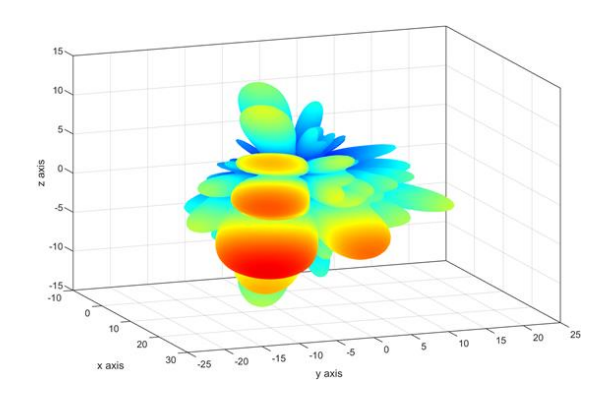


Figure 5-4 Calculated 3D beam pattern generated with the EBF algorithm is illustrated for a single example of radio channel realization.

Therefore, it is crucial to investigate the impact of these highly dynamic and unpredictable beam shapes on radio frequency electromagnetic field exposure, particularly in the context of estimating the power reduction factor employed in the actual maximum approach for Massive MIMO BS, as outlined in IEC 62232 [15].

Numerous publications have analyzed the actual maximum approach for massive MIMO systems using a single selected BF method without comparing it to other schemes, such as [6][20][26]. The influence of BF algorithms on RF EMF exposure was examined in [21], but only for a specific deployment of a single BS and using a ray-tracing channel model. In this chapter, I have extended the statistical analysis presented in previous chapters to encompass various additional BF techniques and massive MIMO antenna configurations to support the implementation of the actual maximum approach for RF EMF exposure evaluation.

### 5.2 Simulation assumptions

This study investigates the performance of a cellular network consisting of seven cells, each with three sectors equipped with massive MIMO multiantenna base stations. The BSs operate in a TDD scheme with a technology duty-cycle factor of 0.75 for the downlink. The BSs are positioned at a height of 25 meters with an inter-site distance of 500 meters. The system operates at a frequency of 3.5 GHz with a 100 MHz channel bandwidth, a subcarrier spacing of 30 kHz, and a maximum transmit power of 51 dBm.

Simulations were conducted using an 8x8 antenna array with cross-polarized antenna elements and two configurations (Figure 5-5): 32 transceivers connected to subarrays and 128 transceivers connected to all antenna elements . The maximum gain of this antenna array is 23.2 dBi at boresight. The antenna was configured with a 5-degree electrical down-tilt to account for UE locations below the antenna height.

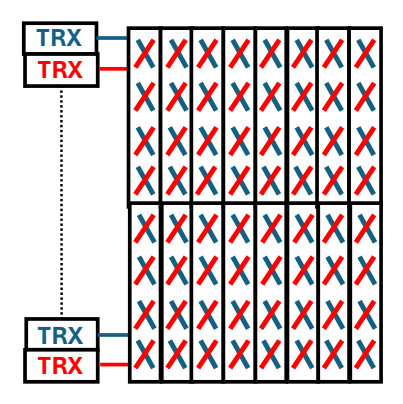


Figure 5-5 Antenna array model 8x8 – antenna capable to generate dual-linear polarization along

Three different beamforming algorithms were implemented:

- GoB ('Grid of Beams'): This algorithm generates 24 beams per polarization (48 in total) uniformly distributed within a 120-degree azimuth opening angle and two elevation angles (Figure 5-6). While GoB enables spatial multiplexing and serves multiple users simultaneously, its limited beam resolution results in lower multi-user MIMO gains.
- **EBF** (**Eigen Beamforming**): This algorithm utilizes the channel covariance matrix averaged over the full carrier bandwidth. The strongest eigenvectors of this matrix are used as a precoder.
- **EZF** (**Zero Forcing**): Similar to EBF, EZF utilizes the channel covariance matrix averaged over the full carrier bandwidth. However, it employs the matrix of strongest eigenvectors for zero forcing precoding calculations.

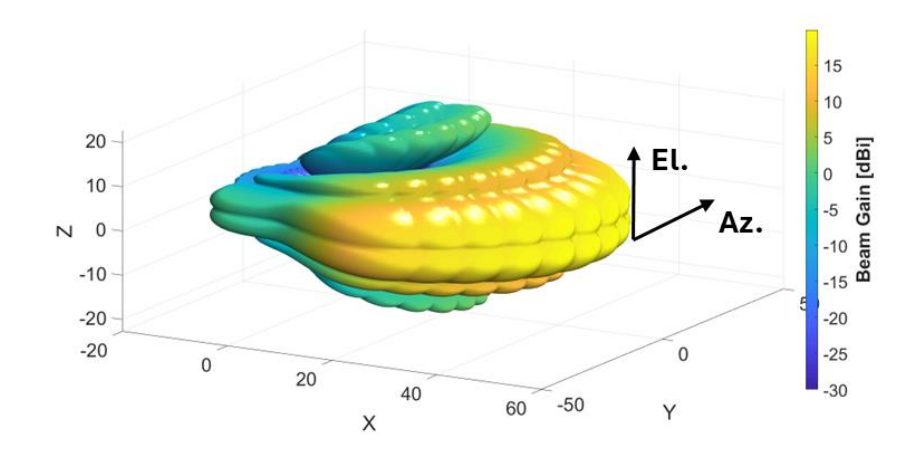


Figure 5-6 Cumulative envelope of beams in GoB BF type.

The simulations assumed ideal Channel State Information (CSI) based on uplink pilots, neglecting pilot contamination.

User equipment was modeled with a single omnidirectional antenna and randomly distributed within each cell. 20% of UEs were considered outdoors, while 80% were indoors, located within buildings with heights uniformly distributed between 4 and 8 floors (following

the 3GPP 38.901 model). UE locations were static, but their positions were randomly rotated for each simulation run.

The number of served terminals (K) was varied between 1, 2, 5, and 8, and the duration of a single DL connection (D) was set to 10, 60, or 360 seconds. The averaging time used for analysis was 6 minutes, as specified in ICNIRP-1998 [24] and IEEE C95.1 [29].

The simulations employed a full-buffer traffic model, assuming fully loaded BSs. Average beamforming gain values were calculated for each BS and subframe to evaluate antenna gain distribution and the performance of the different beamforming algorithms. Table 5-1 summarizes the key simulation assumptions.

*Table 5-1 Main simulation assumptions.* 

Parameter	Value	
Channel model	3GPP 38.901 urban macro (UMa)	
Carrier frequency	3.5 GHz	
Channel bandwidth	100 MHz	
Sub-carrier spacing	30 kHz	
Max total Tx power of BS (without losses)	51 dBm	
No. of TRx	32 or 128	
Gain of BS single antenna element	5.2 dBi	
Configuration of BS antenna array per polarization	8×8	
Electrical down-tilt of BS antenna pattern 5°		
TDD duty cycle for DL	0.75	
Height of BS antenna array centre 25 m		
No. of cells / No. of sectors	7 / 21	
Inter-site distance	500 m	
Type of UE antenna	Omnidirectional	
SU-MIMO maximum rank	2	
UE distribution	80% indoor, uniform distribution between 4 to 8 floors	
No. of simultaneously served UEs	1, 2, 5 and 8	
UE serving time	10 s, 60 s and 360 s	
The actual max approach averaging time	6 min	

### 5.3 The performance of Massive MIMO with different beamforming algorithms

This Section presents a performance comparison of analyzed beamforming methods, specifically with a 32 TRX configuration. Figure 5-7, Figure 5-8, Figure 5-9 and Figure 5-10 illustrate the spectral efficiency, average cell throughput, average user equipment throughput, and cell edge throughput, respectively.

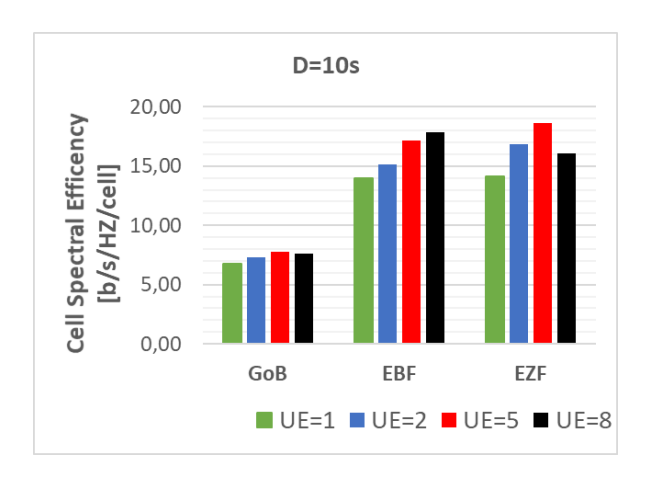


Figure 5-7 Simulation results - Cell spectral efficiency for different BF schemes (32TRX).

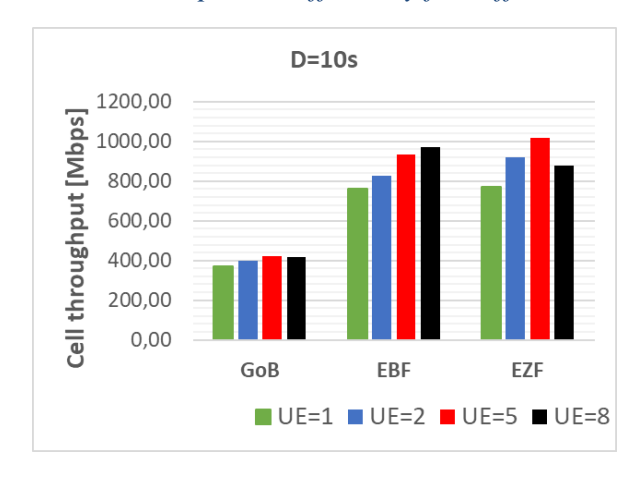


Figure 5-8 Simulation results - Average cell throughput for different BF schemes (32TRX).

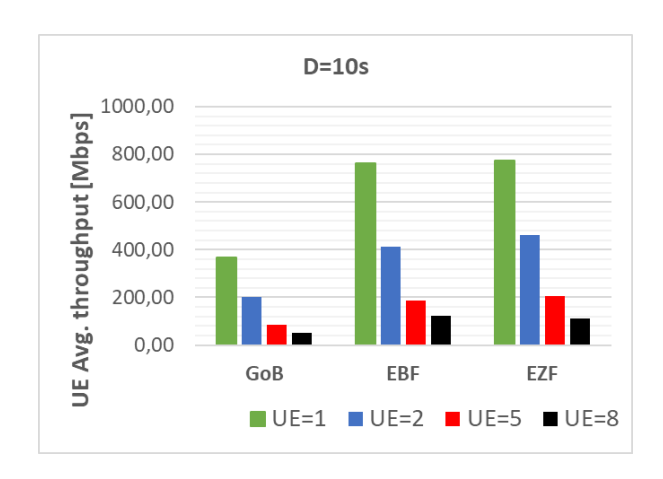


Figure 5-9 Simulation results - Average UE throughput for different BF schemes (32TRX).

The analysis reveals that EBF and EZF beamforming schemes exhibit superior performance compared to the GoB scheme for most combinations of K (number of UEs). Notably, the spectral efficiency of GoB demonstrates only a slight increase with a higher number of served UEs. This indicates that the performance of MU-MIMO is limited by the restricted opportunities for beam pairing due to beam shape and inter-beam interference.

Consequently, with an increased number of simultaneously served UEs, the scheduler faces challenges in selecting, for instance, 5 or 8 beams with an adequate Signal to Interference and Noise Ratio (SINR). This limitation could be mitigated by implementing additional side lobe attenuation.

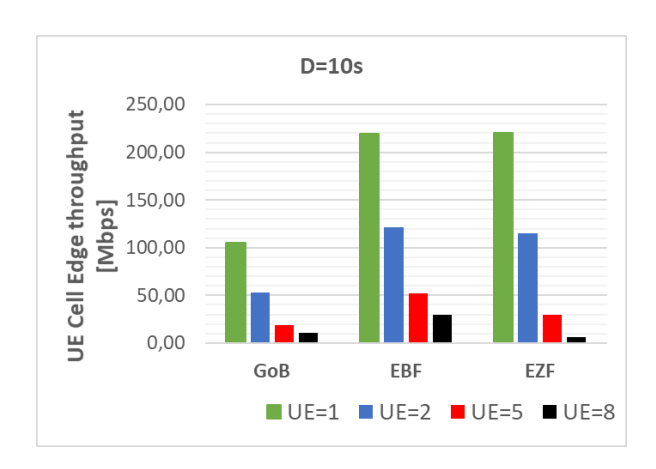


Figure 5-10 Simulation results - UE cell edge throughput for different BF schemes (32TRX).

The implementation of EBF effectively addresses this challenge. EBF's higher antenna beam resolution enhances MU-MIMO pairing capabilities. In the case of EZF, scenarios with 2 and 5 UEs exhibit improved spectral efficiency compared to EBF due to its zero-forcing capability, which effectively cancels interference. However, when 8 UEs are served simultaneously, the spectral efficiency of EZF declines due to its suboptimal performance for cell edge UEs. As depicted in Figure 5-10, the cell edge throughput for EZF with 8 UEs is significantly lower than that of EBF or even GoB. This is attributed to EZF's lack of prioritization for received signal levels, focusing solely on co-channel interference. The increased number of layers results in reduced nulling freedom, large amplitude fluctuations, and a relatively low overall transmitted power. Consequently, cell edge UEs experience reduced received signal levels and lower SINR due to increased neighbor cell interference. As the number of co-scheduled UEs increases, maintaining an adequate level of received downlink signal becomes increasingly challenging for EZF.

Furthermore, the BS antenna architecture assumed for simulation is not optimal for the EZF algorithm when a large number of UEs are served simultaneously. This is due to sub-paneling, which reduces the degrees of freedom of EZF for efficient null forming in elevation. A similar, albeit less pronounced, impact can be observed on EBF for cell edge UEs.

The presented results highlight the absence of a universal beamforming algorithm suitable for all use cases. EBF and, particularly, EZF demonstrate sensitivity to the quality of channel state information. Therefore, practical base station implementations could benefit from employing multiple beamforming algorithms, each tailored to specific use cases.

For instance, EZF could be effectively utilized for UEs located in close proximity to the BS and spatially separated, while EBF could be employed in coverage areas with reliable CSI. Conversely, GoB, due to its inherent reliability, could be enabled for UEs situated at the cell

edge. This dynamic approach allows for optimized beamforming performance across diverse network conditions.

# 5.4 The analysis of beamforming schemes impact on actual EMF exposure

The simulation results of the actual RF EMF exposure are shown in the form of CDF plots of the averaged EIRP normalized to the maximum EIRP corresponding to the direction of the highest RF EMF exposure. Impact of BF schemes and antenna array configurations (number of TRXes) to actual EMF exposure are evaluated in the following Sections.

#### 5.4.1 Impact of beamforming algorithm on actual EMF exposure

This Section analyzes the reduction of RF EMF exposure achieved through different beamforming techniques, namely GoB, EBF, and EZF, in a 32-transceiver antenna array. The results of simulation run within that doctoral studies, presented in Figure 5-11 to Figure 5-14, correspond to varying numbers of served UE, denoted by K, with values of 1, 2, 5, and 8, respectively. All results are obtained for various service times (D) and demonstrate the expected reduction in actual RF EMF exposure with EBF and EZF compared to GoB, attributed to the higher dynamic of beam shaping.

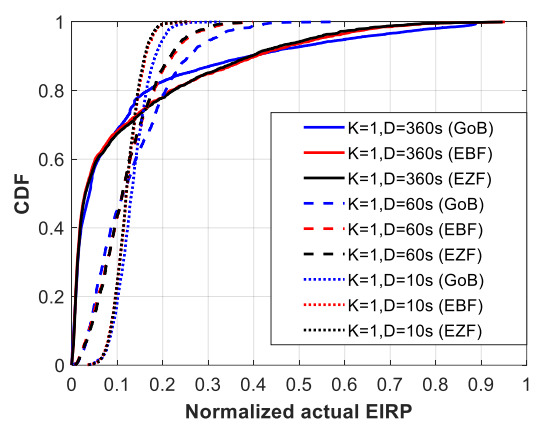


Figure 5-11 Simulation results - impact of BF scheme on normalized actual EIRP for K=1.

In the case of a single served UE (K=1) over extended periods (D=360 s), a scenario rarely encountered in operational networks, EBF and EZF still exhibit reduced RF EMF exposure compared to GoB. Notably, EBF and EZF results are nearly identical for K=1, as interference cancellation is unnecessary with a single UE in the cell.

As the number of UEs increases, the reduction in actual RF EMF exposure becomes more pronounced for EBF and EZF compared to GoB. EZF, specifically designed for interference reduction through null forming, achieves a more significant EMF exposure reduction than GoB and EBF, which prioritize maximizing received power levels.

The CDF curves presented in Figure 5-11 to Figure 5-14 can be utilized as valid input for the BS installation compliance procedure outlined in IEC 62232 [15], based on the actual maximum EIRP. This procedure allows for the determination of the actual maximum EIRP

threshold using CDF derived from computational modeling, which corresponds to the  $F_{PR}$  defined in IEC 62232:2022 [15]. The  $F_{PR}$ , obtained from the normalized CDF curves multiplied by the technology duty cycle factor, can be implemented on the BS to ensure that the determined threshold is not exceeded during operation.

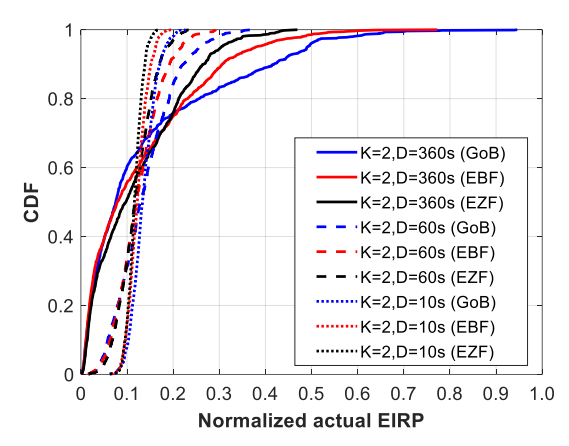


Figure 5-12 Simulation results - impact of BF scheme on normalized actual EIRP for K=2.

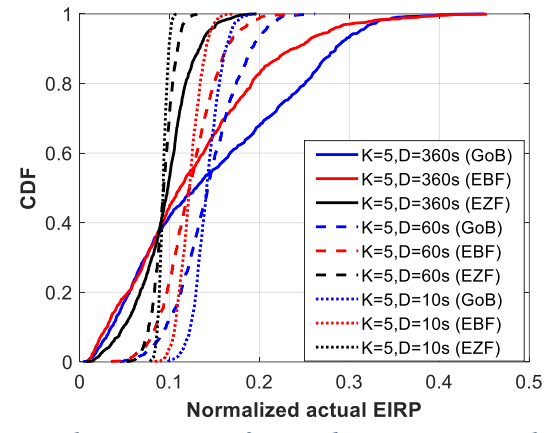


Figure 5-13 Simulation results - impact of BF scheme on normalized actual EIRP for K=5.

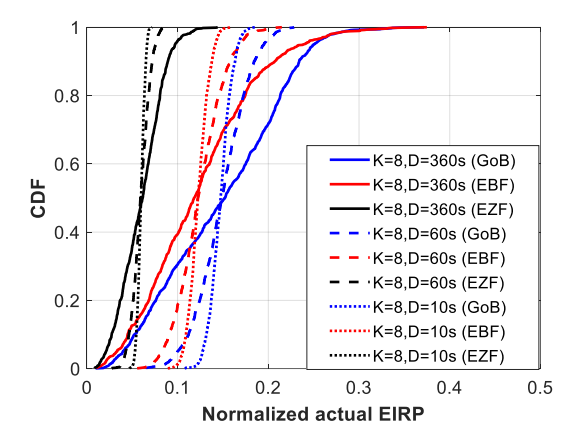


Figure 5-14 Simulation results - impact of BF scheme on normalized actual EIRP for K=8.

Figure 5-11 to Figure 5-14 illustrate the variation of F<sub>PR</sub>, determined as the 95th percentile of the CDF curves presented above, with Table 5-2 summarizing its values for a serving time

of 60 seconds. Notably, the  $F_{PR}$  value decreases for all BF algorithms when traffic becomes more dynamic, characterized by a higher number of UEs (K) and shorter serving times (D). This reduction in  $F_{PR}$  is more pronounced for lower numbers of served UEs (K=1 and K=2) when the serving time decreases. For instance, in the case of GoB, the difference in  $F_{PR}$  values between D=60 seconds and D=10 seconds is 2.1 dB and 1.4 dB for K=1 and K=2, respectively. Conversely, when more UEs are served simultaneously (K=5 and K=8), this difference reduces to 0.9 dB and 0.6 dB, respectively. It is important to note that with 5 or 8 UEs in the cell, simultaneous service using MU-MIMO with separate beams is not always feasible. This depends heavily on UE locations within the cell and radio propagation conditions. Inter-beam interference can limit the number of UEs paired for MU-MIMO, leading to the service of remaining UEs in different time slots instead of separate beams, which likely contributes to the observed behavior.

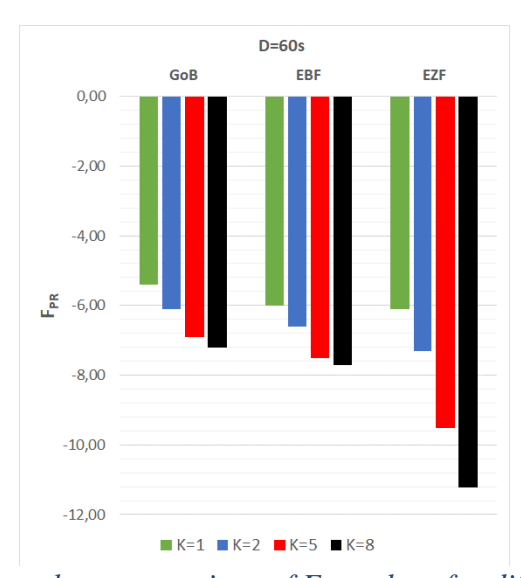


Figure 5-15 Simulation results - comparison of  $F_{PR}$  values for different BF schemes in the case of D=60s.

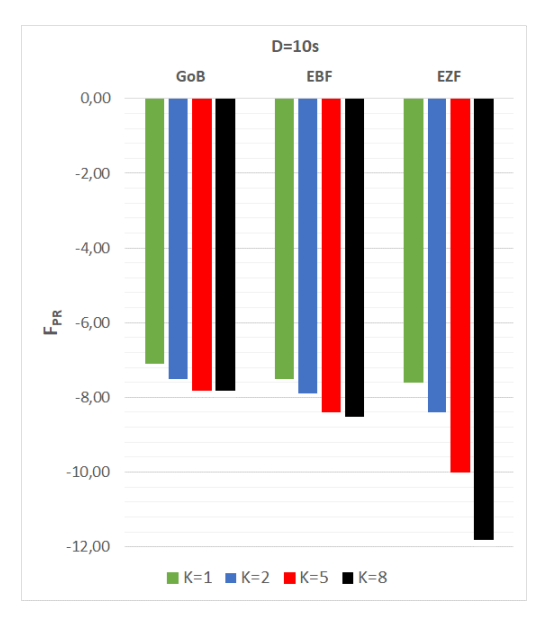


Figure 5-16 Simulation results - comparison of simulation results of  $F_{PR}$  values for different BF schemes in the case of D=10s.

Table 5-2 Simulation results of  $F_{PR}$  for different BF schemes (D=60).

BF type	K	<b>D</b> (s)	$F_{PR}(dB)$
GoB	1	60	-5.0
EBF	1	60	-6.0
EZF	1	60	-6.1
GoB	2	60	-5.9
EBF	2	60	-6.6
EZF	2	60	-7.3
GoB	5	60	-6.9
EBF	5	60	-7.5
EZF	5	60	-9.5
GoB	8	60	-7.1
EBF	8	60	-7.7
EZF	8	60	-11.2

Further analysis of the median values (50th percentile) of the CDF curves in Figure 5-11 to Figure 5-14, summarized in Table 5-3 for D=60 seconds, reveals additional insights. While the 95<sup>th</sup> percentile of normalized EIRP (presented as F<sub>PR</sub>) decreases with increasing K or decreasing D for all BF schemes, the 50th percentile of normalized EIRP for GoB and EBF remains independent of the number of UEs and serving time. This is attributed to the conservation of energy, which is independent of the time required for energy summation or averaging. In contrast, the median value of normalized EIRP for EZF decreases with the addition of new UEs. This algorithm reduces energy through beam-nulling, resulting in stronger cancellation as K increases. However, decreasing the serving time (D) for a given K does not affect the median of normalized EIRP for EZF, again due to energy conservation.

Table 5-3 Simulation results of median of actual normalized EIRP for different BS types.

K	<b>D</b> [s]	GoB	EBF	EZF
1	60	-8.6	-9.1	-9.1
2	60	-8.6	-9.1	-9.3
5	60	-8.4	-9.1	-10.3
8	60	-8.3	-9.1	-12.2

#### 5.4.2 Impact of number of transceivers on actual EMF exposure

The previous subsection demonstrated that employing an advanced beamforming scheme reduces the  $F_{PR}$  compared to the GoB approach. Notably, in the case of EBF, the  $F_{PR}$  can be lowered by 0.5 dB to 1.1 dB (for a duration of 60 seconds). This difference becomes even more

pronounced when a massive MIMO base station (BS) is equipped with a larger number of TRX units, increasing the degrees of freedom available to the EBF algorithm.

To quantify this difference, the simulation study increased the initial number of TRX from 32 to 128, ensuring that each antenna element was connected to a separate TRX. Evaluations were conducted for both GoB and EBF, and an example of the cumulative distribution function with normalized EIRP for K = 2 and D = 60 seconds is presented in Figure 5-17.

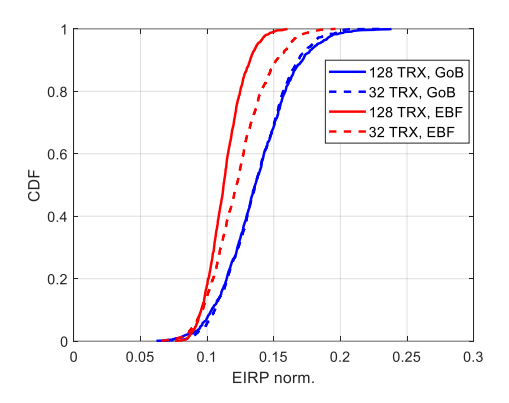


Figure 5-17 Simulation results - comparison of normalized actual EIRP for 32 and 128 TRXes~(K=2, D=60s).

For GoB, the actual RF EMF exposure remains comparable for both antenna array configurations. The F<sub>PR</sub>, determined as the 95<sup>th</sup> percentile, increased by 0.1 dB for 128 TRX compared to 32 TRX. This observation is consistent with the assumption that for GoB, the number and directions of predefined beams are fixed, and additional TRX chains do not provide any performance or EMF reduction benefits. However, a slight difference is noticeable due to improved resolution of antenna weights in the columns of the antenna array for 128 TRX compared to 32 TRX, which has four antenna elements in a single sub-array connected to a single TRX per polarization.

The advantages of a full digital architecture become more apparent when the EBF algorithm is employed. This is attributed to the enhanced capabilities of the precoder due to the increased degrees of freedom compared to the subarray architecture with 32 TRX. Consequently, the  $F_{PR}$  for EBF decreases, reaching 1.2 dB lower for 128 TRX compared to GoB, whereas it was only 0.4 dB lower for 32 TRX.

These results indicate that equipping the BS with a larger number of TRX can potentially lower the actual EIRP and reduce EMF exposure. This is because the increased degrees of freedom for beamforming algorithms result in denser beam resolution and greater variance in the antenna pattern characteristics (in the case of EBF/EZF).

## 5.5 Summary and conclusions

To summarize, all  $F_{PR}$  values determined in this study have been compiled in Table 5-4. This table includes values for various representative configurations, which can be utilized in RF exposure evaluation of a given BS or configured as an input parameter in the actual EIRP control algorithm. Cases with D = 360 seconds have been excluded from this table, as such long

continuous serving times for user equipment are not observed in operational networks. The use cases with D=10 seconds and 60 seconds are more practical but still conservative, as in operational networks, this duration can vary even on a subframe basis. This conservative approach provides a margin for practical implementation of the EMF actual maximum approach.

As shown in Table 5-4, the ranges of  $F_{PR}$  values are:

[-5.1 dB: -7.8 dB] for GoB
[-6.0 dB: -8.5 dB] for EBF
[-6.1 dB: -11.8 dB] for EZF

Therefore, it can be concluded that the  $F_{PR}$  takes values between -5.1 dB and -11.8 dB when 1 to 8 UEs are served simultaneously and continuously for 10 seconds to 60 seconds using GoB, EBF, or EZF beamforming algorithms implemented in a 5G BS array antenna with 32 TRX. This wide range of  $F_{PR}$  values highlights the importance of carefully selecting the appropriate value for real BS operation, taking into account the base station configuration, including antenna array setup, beamforming schemes, and predicted traffic type.

Table 5-4 Summary of  $F_{PR}$  values for 8x8 antenna array with different BF algorithms, UEs distribution and TRX configurations.

BF scheme	K	D (s)	F <sub>PR</sub> (dB) for 32 TRX	F <sub>PR</sub> (dB) for 128 TRX
GoB		10	-7.0	-6.9
		60	-5.1	-5.0
EBF	1	10	-7.5	-8.4
EDF	1	60	-6.0	-7.1
EZF		10	-7.6	-
EZF		60	-6.1	-
CoP		10	-7.5	-7.4
GoB		60	-6.1	-6.0
EBF	2	10	-7.9	-8.6
EDF		60	-6.6	-7.6
EZF		10	-8.4	-
EZF		60	-7.3	-
GoB		10	-7.8	-7.7
GOD		60	-6.9	-6.8
EBF	5	10	-8.4	-8.9
EDF	3	60	-7.5	-8.3
EZF		10	-10.0	-
		60	-9.5	-
CoP		10	-7.8	-7.7
GoB	8	60	-7.2	-7.1
EDE		10	-8.5	-9.0
EBF	o	60	-7.7	-8.5
EZF		10	-11.8	-
EZF		60	-11.2	-

This Chapter investigates the impact of advanced beamforming algorithms and antenna array configurations on the evaluation of actual RF EMF exposure from massive MIMO base stations, as defined by IEC 62232 [15]. The analysis utilizes a 3D statistical channel modeling tool described in Chapter 2 with implemented GoB, EBF, and EZF techniques, as well as antenna arrays with 32 and 128 TRXes.

The study reveals that advanced beamforming schemes, such as EBF or EZF, can reduce actual RF EMF exposure by up to -4 dB compared to the GoB scheme when 8 UEs are connected to the BS. Consequently, lower  $F_{PR}$  can be considered when implementing the actual maximum approach.

A comprehensive comparison of the simulation results indicates that  $F_{PR}$  values can range from -5.1 dB to -11.8 dB when 1 to 8 UEs are served simultaneously and continuously at full buffer for 10 to 60 seconds using GoB, EBF, or EZF beamforming algorithms implemented in a 5G BS array antenna with 32 TRX. Increasing the number of TRX further reduces the  $F_{PR}$ .

It is anticipated that the planned increase in antenna array sizes, associated with a higher number of TRX to enable extreme massive MIMO in upcoming 5G-advanced and 6G technologies, will lead to further reductions in  $F_{PR}$  values. This topic will be discussed in the following chapter.

The research presented in this chapter was published in [37].

# 6. Evaluation of the actual EMF exposure from Extreme Massive MIMO base stations

# 6.1 Introduction to Extreme Massive MIMO for future wireless systems generations

Massive MIMO systems are evolving from simpler beamforming techniques, which rely on codebooks containing a finite number of orthogonal beams selected based on user equipment feedback, to advanced beamforming algorithms. These algorithms can adapt to time-varying radio channel characteristics based on sounding pilots transmitted from the UE.

Multiantenna systems for base stations are also widely considered crucial for ensuring adequate coverage in the new millimeter wave frequency bands introduced for mobile systems [38] [39]. The high frequencies in the mmWave spectrum result in increased free space path loss, penetration loss, and vegetation loss. Large antenna arrays can compensate for these losses.

Therefore, mMIMO is seen as a leading technology for the future 6G standard [40][41][42]. The next generation of mobile systems will utilize new frequency bands in the 7-24 GHz spectrum. This spectrum called in 3GPP FR3 offers large bandwidths but presents challenges in ensuring adequate coverage, particularly compared to the mmWave spectrum. The frequency range between 7 GHz and 15 GHz are especially interested to mobile communication industry.

Increasing the operating frequency from the commonly used 3.5 GHz band in 5G to the 7-15 GHz band planned for 6G necessitates the design of larger antenna arrays to maintain coverage [41]. These arrays will incorporate over one hundred antenna elements, but their overall size will remain similar due to the shorter wavelengths and smaller antenna element sizes. Consequently, extreme mMIMO technology, with significantly larger antenna arrays than those currently deployed, is a key area of research in the development of 6G.

The example of mMIMO array evolution in Figure 6-1 demonstrates that by increasing the operating frequency from 3.5 GHz (currently used in 5G) to 8 GHz (planned for 6G), we can significantly increase the number of antenna elements (AEs) within a similar or even smaller form factor. This Figure shows a substantial increase in AE density, with 1024 AEs for 6G compared to 192 AEs for 5G.

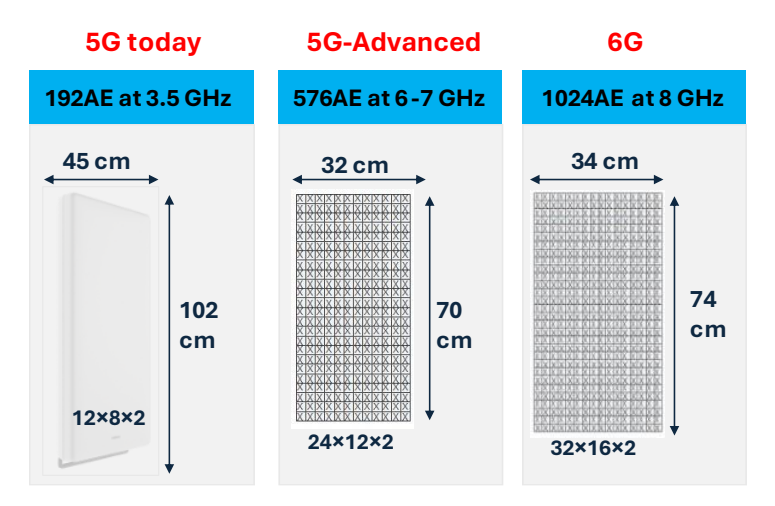


Figure 6-1 The evolution of mMIMO arrays from 5G to 6G is characterized with a few fold increase in element numbers and in smaller 6G antenna outline.

The high gain of large antennas leads to exceptionally large exclusion zones when the maximum radiated power is used for EMF exposure assessment. The actual maximum approach, introduced by IEC 62232 [14] addresses this by accounting for the variability of BS parameters during operation and considering time-averaging over 6 or 30 minutes, as recommended by ICNIRP guidelines [12]. In the case of extreme mMIMO, where antenna gain can exceed 30 dBi, implementing the actual maximum approach is crucial for supporting the deployment of 6G BS.

While most studies [43][40][41][42] focus on the performance and energy efficiency of extreme mMIMO, this thesis focuses on modeling the electromagnetic field exposure from BS equipped with large antenna arrays. This chapter presents modeling results of the power reduction factors applicable to extreme mMIMO systems when implementing the actual maximum approach.

#### 6.2 Simulation methodology

This analysis was conducted using a cellular network model comprising 7 cells, each equipped with three sectors featuring extreme mMIMO BSs. Given that the new frequency bands for 6G are anticipated to be based on TDD mode, the simulations were performed using this mode with a technology duty cycle factor of 0.75 for the downlink. In this scenario, all BSs were positioned at a height of 25 meters with an inter-site distance of 500 meters. Center frequency of 10 GHz was selected as a representative frequency within the 7-15 GHz range planned for 6G. The simulated system operates with a bandwidth of 100 MHz and employs OFDMA with 30 kHz subcarrier spacing. BSs transmit with 200 W of radio frequency (RF) power using extreme mMIMO antenna arrays.

Five different extreme mMIMO antenna array sizes were considered, as detailed in Table 6-1. All arrays utilize cross-polarized antenna elements, and 64 or 128 transceivers connected to subarrays, as illustrated in Figure 6-2, which depicts a 12×16 antenna array as an example. These antenna configurations represent realistic implementations of practical arrays. The number of TRX is lower than the total antenna elements because each TRX corresponds to a sub-array of 3 to 6 antenna elements. The array with 12x8 antenna elements and 64 TRX is typical mMIMO configuration used in currently deployed 5G networks.

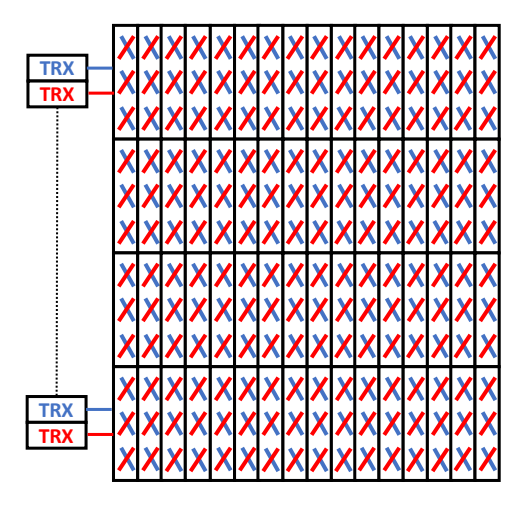


Figure 6-2 Extreme mMIMO antenna array scheme with 12×16 cross-polarized antenna elements clustered in multiple 64 sub-arrays. Each sub-array is connected to 2 TRXes (1 TRX per polarization, 128 TRXes in total).

Table 6-1 Extreme Massive MIMO array configurations.

Antenna Array Size (V×H)	Number of TRX	Number of sub-arrays (V×H)	Sub-array size (V×H)	Total antenna elements number (both pol.)	Maximum Antenna Gain [dBi]
12×8	64	4×8	3×1	192	25.0
24×8	128	8×8	3×1	384	28.0
12×16	128	4×16	3×1	384	28.0
16×16	128	4×16	4×1	512	29.3
24×16	128	4×16	6×1	768	31.0

UEs use an omnidirectional antenna with two polarizations and are randomly distributed in a cell. In indoor areas, 80% of UEs are placed inside buildings with a height uniformly distributed between 4 and 8 floors, and the other 20% of UEs are placed outdoors at street level. The locations of UEs are static during DL transmission but are randomly rotated at every drop. The duration D of a single DL connection is 60 s, and the number K of terminals served simultaneously is considered to be 1, 2, 5 or 8 (16 MIMO streams in total because MIMO 2x2 is used). The full buffer traffic model is used so that the BS is fully loaded.

*Table 6-2 Main parameter specifications for simulations.* 

Parameter	Value	
Channel model	3GPP 38.901 Urban Macro (UMa)	
Carrier frequency	10 GHz	
Channel bandwidth	100 MHz	
Sub-carrier spacing	30 kHz	
Max total Tx power of BS (without losses)	53 dBm (200W)	
Gain of BS single antenna element	5.2 dBi	
Electrical down-tilt of BS antenna	5°	
TDD duty cycle for DL	0.75	
Height of BS antenna array centre	25 m	
No. of cells / No. of sectors	7 / 21	
Inter-site distance	500 m	
Type of UE antenna	Omnidirectional	
SU-MIMO maximum rank	2	
Beamforming type	Eigenbeamforming, wideband CSI	
UE distribution	20% outdoor 1.5 height, 80% indoor with uniform distribution between 4 to 8 floors	
No. of simultaneously served UEs (K)	1, 2, 5 and 8	
UE serving time (D)	60 s	

The selected traffic model and long continuous transmission time towards UE correspond to conservative assumptions for this EMF exposure analysis because, in the real networks, BS generally operate with lower load conditions and beams are often switching between different UEs. Table 6-2 shows main simulation assumptions. Eigenbeamforming was selected as beamforming algorithm.

Simulations use an averaging time of 6 minutes as specified in ICNIRP [12][24] and IEEE C95.1 [29]. Actual (i.e. time-averaged) values of the EIRP are calculated for each BS and for every subframe as part of the implementation of the actual maximum approach.

## 6.3 The performance of Extreme Massive MIMO systems

The performance of various antenna array configurations, as determined through simulation modelling, is presented in Figure 6-3 for spectral efficiency, Figure 6-4 for averaged cell throughput, Figure 6-5 for averaged UE throughput, and Figure 6-6 for UE cell edge throughput. The results demonstrate a clear trend of increasing network performance with the deployment of larger multiantenna systems.

According to the modelling results, the system with extreme mMIMO BSs could achieve several dozen bits per second per Hertz (b/s/Hz) of spectral efficiency (30-50 b/s/Hz), guaranteeing very high cell capacity reaching nearly 2.5 gigabits per second (Gb/s) for the largest array. This level of capacity enables serving UEs with a throughput of hundreds of megabits per second (Mbps) across the entire cell, even when multiple terminals are served simultaneously due to spatial multiplexing and beamforming. Larger arrays exhibit higher beam weight resolution and narrower beams, facilitating more efficient radio resource reuse through effective spatial multiplexing. The increased number of antenna elements enhances antenna gain, further improving performance.

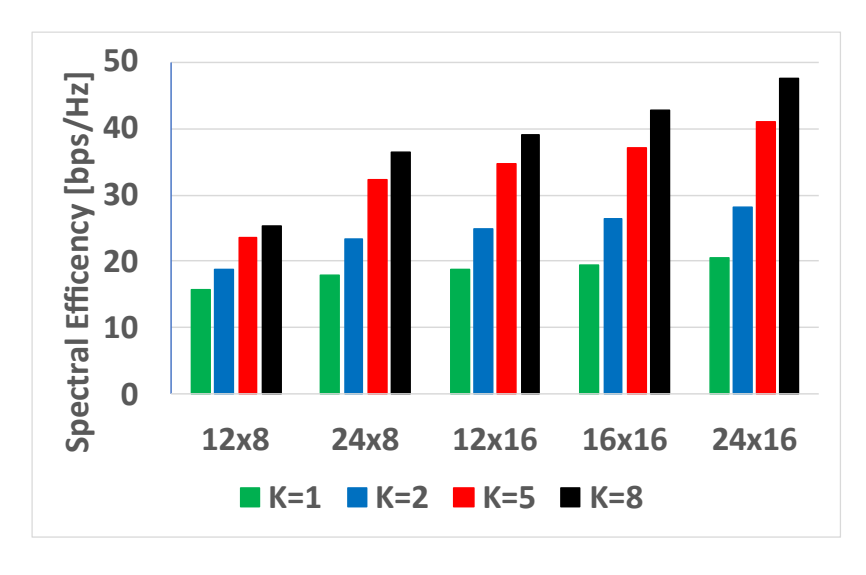


Figure 6-3 Simulation results of cell spectral efficiency for different extreme mMIMO array setup.

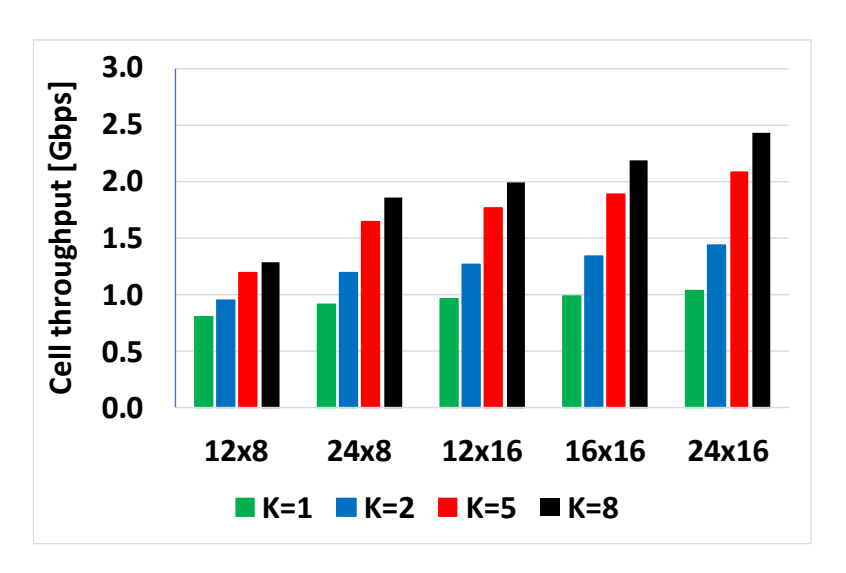


Figure 6-4 Simulation results of average cell throughput for different extreme mMIMO array setup.

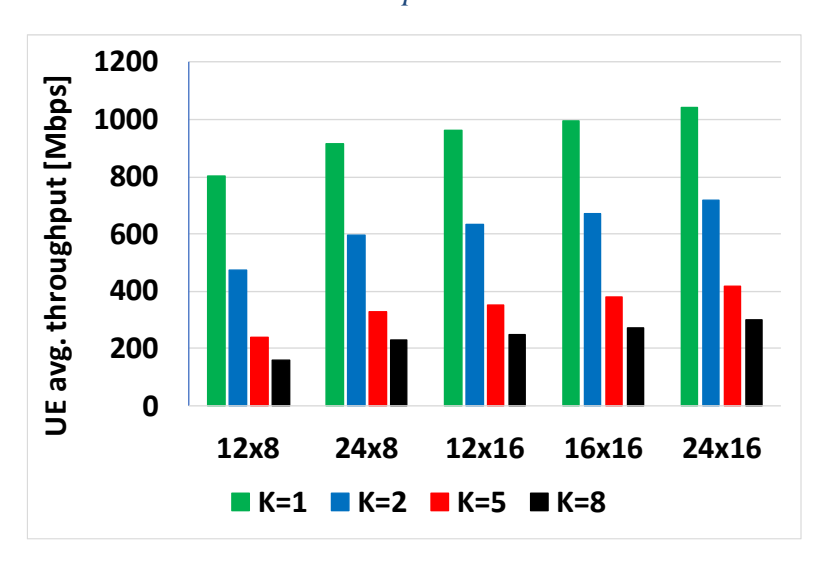


Figure 6-5 Simulation results of average UE throughput for different extreme mMIMO array setup.

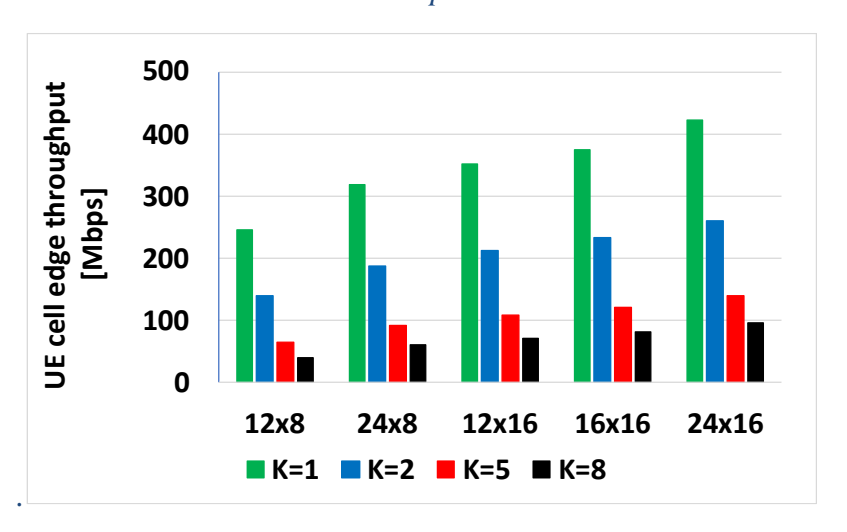


Figure 6-6 Simulation results of average UE cell edge throughput for different extreme mMIMO array setup.

The system's performance could be further enhanced by employing more complex algorithms, such as zero-forcing, as demonstrated in a Chapter 5. While the performance was studied for a 100 MHz bandwidth, future deployments in the FR3 band are expected to utilize 200 MHz bandwidths [44], potentially doubling the achieved results.

# 6.4 The analysis of actual EMF exposure form Extreme Massive MIMO

This Section presents the results of actual exposure simulations for extreme mMIMO base stations in the context of 6G. The simulations results show CDF of the actual EIRP normalized to the maximum EIRP in the direction of highest radio frequency electromagnetic field exposure.

The simulation results presented in the form of CDF curves presented in Figure 6-7 to Figure 6-9 can be used as input for the compliance procedure for BS installation, as outlined in IEC 62232 [15]. The  $F_{PR}$  is determined by the normalized actual EIRP value for a given percentile (e.g.,  $95^{th}$  or  $99^{th}$  percentile) multiplied by the technology duty cycle factor.

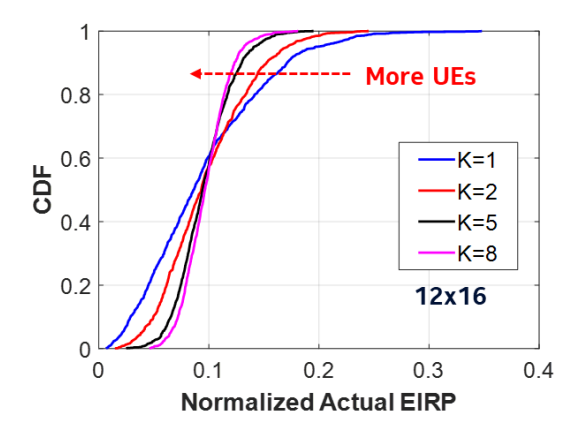


Figure 6-7 Simulation results - CDF of normalized actual EIRP for extreme mMIMO array of 12×16 for different number of UEs.

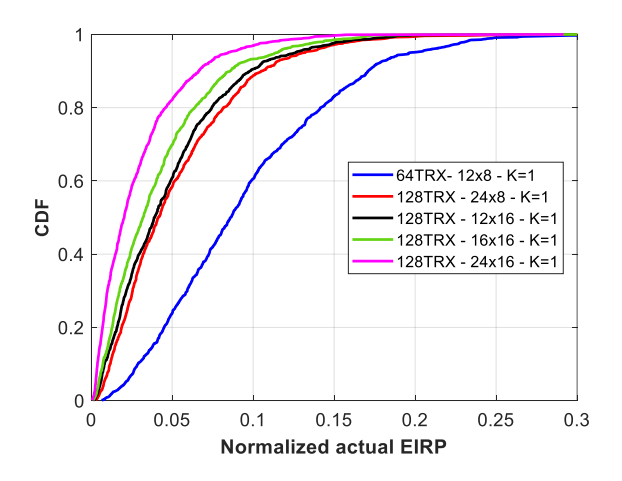


Figure 6-8 Simulation results - CDF of normalized actual EIRP for different extreme mMIMO arrays for K = 1.

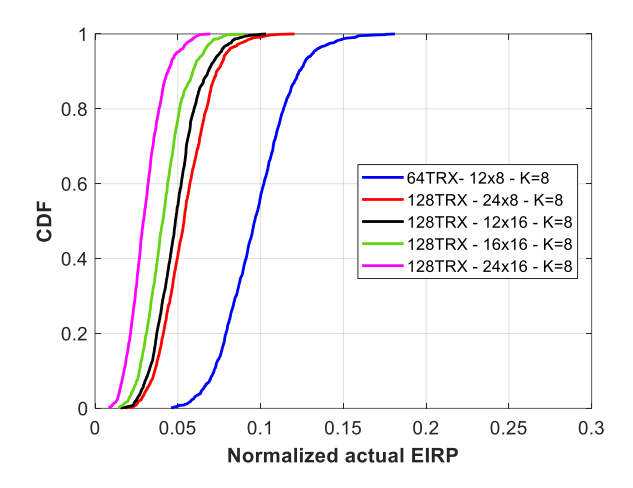


Figure 6-9 Simulation results - CDF of normalized actual EIRP for different extreme mMIMO arrays for K = 8.

Figure 6-7 shows the CDF of the normalized actual EIRP for a 12x16 antenna array with varying numbers of served user equipment (K = 1, 2, 5, and 8). An increase in the number of served UEs leads to lower exposure due to multi-beam operations and power splitting. Notably, even in the rare case of K = 1, the normalized actual EIRP reaches a maximum of 30%, while it reduces to only 10% when 8 UEs are served simultaneously. This demonstrates that fast beamforming and multi-beam operation significantly reduce average EMF exposure in areas close to the BS compared to the configured maximum EIRP.

Figure 6-8 and Figure 6-9 illustrate the relationship between normalized actual EIRP and antenna array size for K = 1 and K = 8, respectively. These results indicate that normalized actual EIRP (and consequently EMF exposure) decreases as the number of transceivers and antenna elements in the extreme mMIMO antenna array increases. This reduction is attributed to the narrowing beamwidth caused by the larger array size, leading to a decrease in actual EMF exposure levels near the BS due to the beamforming algorithm's rapid adaptation to radio conditions and UE positions.

Figure 6-10 and Table 6-3 present a comparison of  $F_{PR}$  values for the 95<sup>th</sup> percentile across all antenna configurations and numbers of served UEs, including the 99<sup>th</sup> percentile results. Larger arrays exhibit lower  $F_{PR}$  values. For instance, the largest array (24x16) shows an  $F_{PR}$  value of -8.7 dB for K=1 and -12.2 dB for K=8 (for the 99<sup>th</sup> percentile), representing a 3.5 dB reduction.

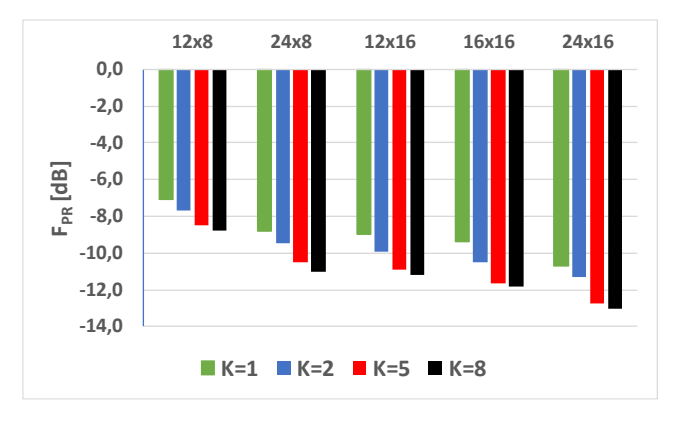


Figure 6-10 Simulation results - comparison of  $F_{PR}$  values for a 95<sup>th</sup> percentile for different extreme mMIMO arrays (D = 60 s).

Figure 6-11 further explores the results by presenting the actual antenna gain for all studied array configurations. While the maximum antenna gain increases from 25 dBi to 31 dBi (6 dB range) for extreme mMIMO, the actual antenna gain, relevant for implementing the actual maximum approach, increases only from 16 dBi to 18 dBi (2 dB range), comparable to legacy fixed beam antennas used in current networks.

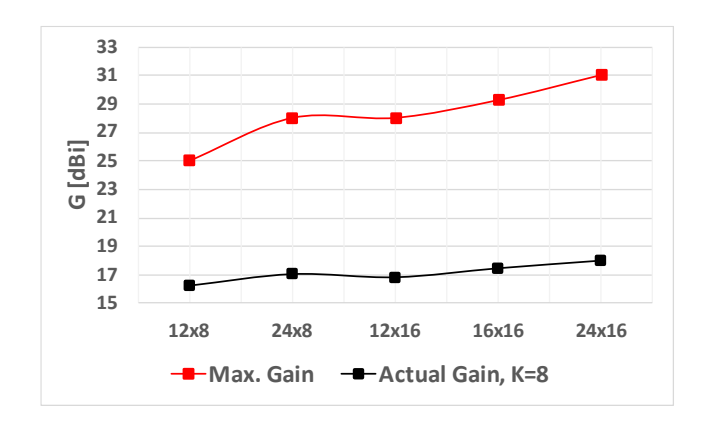


Figure 6-11 Simulation results of maximum and actual averaged calculated antenna gain (for K = 8) for different extreme mMIMO antenna arrays.

Table 6-3 Summary of  $F_{PR}$  calculated values from simulation studies for different extreme Massive MIMO antennas for D = 60s.

Number of served UEs	Antenna Array Type	95 <sup>th</sup> percentile $F_{PR}[dB]$	99 <sup>th</sup> percentile F <sub>PR</sub> [dB]
	12x8	-7.1	-6.0
	24x8	-8.8	-7.4
K = 1	12x16	-9.0	-7.5
13 – 1	16x16	-9.4	-7.9
	24x16	-10.7	-8.7
	12x8	-7.7	-6.9
	24x8	-9.5	-8.6
K = 2	12x16	-10.0	-8.8
	16x16	-10.5	-9,2
	24x16	-11.3	-10.1
	12x8	-8.5	-7.9
	24x8	-10.5	-9.7
K = 5	12x16	-10.9	-10.0
	16x16	-11.6	-10.9
	24x16	-12.8	-11.5
K = 8	12x8	-8.8	-8.1
	24x8	-11.0	-10.1
	12x16	-11.2	-10.6
	16x16	-11.8	-11.2
	24x16	-13.1	-12.2

The application of the actual maximum approach to extreme mMIMO significantly reduces the compliance distance of the deployed BS, as illustrated in Figure 6-12 for a limit of 61 V/m electric field strength according to [15] using the free space formula described in [14]. Comparing the compliance distance calculated for the configured maximum EIRP with the actual maximum EIRP using  $F_{PR}$  values based on the 95<sup>th</sup> and 99<sup>th</sup> percentiles, we observe that assuming the maximum antenna gain results in compliance distances ranging from 20 m to 40 m for the largest 24x16 array. These values would impose significant constraints on extreme mMIMO deployment in urban areas. However, implementing the actual maximum approach with extreme mMIMO maintains compliance distances within a range of 8.5 m to 11.5 m, even for the conservative case of K = 1, enabling deployments in urban environments.

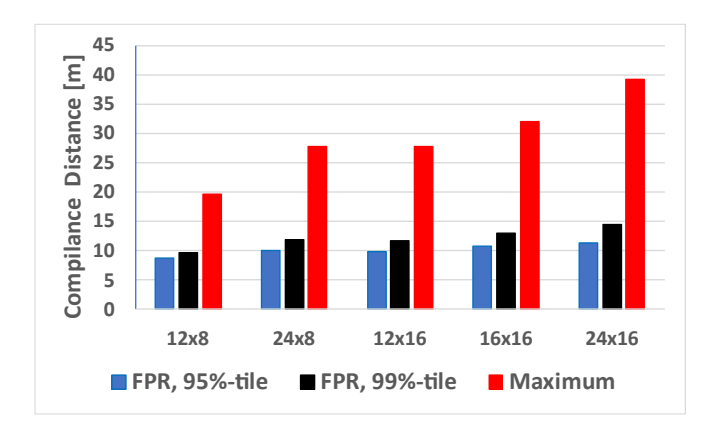


Figure 6-12 Comparison of compliance distances calculated with the actual maximum approach with  $F_{PR}$  95<sup>th</sup> and 99<sup>th</sup> percentile and maximum approach for different mMIMO antenna configurations in case of K=1.

These findings highlight the importance and benefits of implementing the actual maximum approach to support the deployment of extreme mMIMO BS in 6G.

The results presented thus far are based on the UE distribution probability described in 3GPP TR 38.901 [19]. However, scenarios where UEs are more concentrated in specific locations, such as on a single floor, may occur. Figure 6-13 presents three additional UE distribution scenarios to illustrate these use cases using the largest extreme mMIMO antenna array (24x16) and K=8.

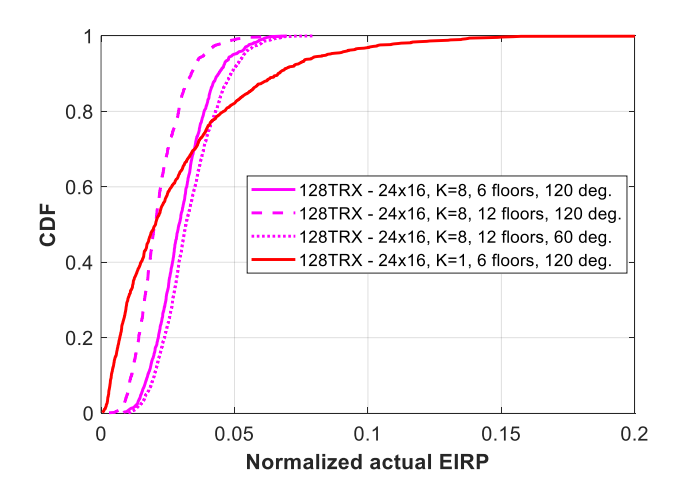


Figure 6-13 Simulation results - CDF of normalized actual EIRP for extreme mMIMO arrays  $24 \times 16$  for various UE distributions with K = 8.

The first scenario assumes UEs are uniformly distributed throughout the sector (120 degrees azimuth range) and in elevation from street level to a mean of 12 floors (range from 10 to 14 floors). The second scenario reduces the mean number of floors with UEs to 6 (range from 4 to 8 floors) while maintaining the horizontal distribution. The third scenario uses the same number of floors as scenario 1 but limits the horizontal UE distribution to approximately 60 degrees. Figure 6-13 shows the variability of the CDF and corresponding  $F_{PR}$  in these three scenarios based on K=8 UEs. It also confirms that the reference scenario with K=1 provides a conservative estimate of  $F_{PR}$ .

## 6.5 The evaluation of actual electric field from Extreme Massive MIMO

This Section analyses the simulation results of EMF exposure at the position of served UEs. The actual EMF exposure was estimated for all UEs within the simulation range (3D distance from 6 m to 760 m) based on the total time-averaged electric field strength from all active BSs and beams during the DL transmission period (D = 60 s). The results include electric field strengths from all beams of the BS transmitting to UEs, as well as electric fields from interfering beams originating from the same and surrounding BSes.

Figure 6-14 demonstrates that while some variability exists in the actual maximum EMF exposure levels between the smallest 12x8 antenna array and the largest 24x16 antenna array, the actual exposure levels remain significantly lower than the exposure limit of 61 V/m for this frequency band, as defined in [12]. The results also confirm that when K = 1, the actual EMF exposure at the served UE position is higher compared to K = 8 simultaneously served UEs. This is attributed to multi-beam operation, which distributes transmit power across all active beams.

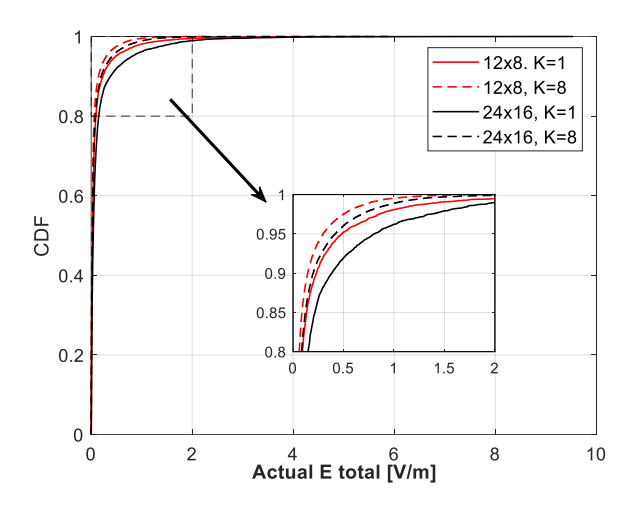


Figure 6-14 Simulation results - CDF of total actual electric field strength at the serving UE position for different extreme mMIMO arrays (12×8 and 24×16) and number of served UEs (K = 1 and K = 8).

Figure 6-15 compares the actual EMF levels from all sources using the largest extreme mMIMO BS with a 24x16 array and K=8 served UEs simultaneously. The highest actual EMF exposure originates from the beams directly serving the UE (denoted as E own in Figure 6-15). Contributions to the actual EMF exposure from beams serving other UEs (denoted as E other in Figure 6-15) are significantly smaller. This is due to the high gain beams formed by the mMIMO BS towards serving UEs. Other sources of exposure primarily stem from side lobes and nulls of the beam pattern of surrounding BSs, rather than the main beams.

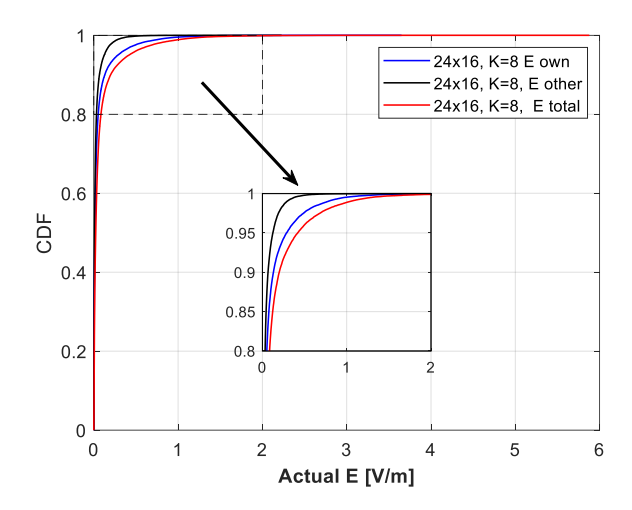


Figure 6-15 Simulation results - CDF with comparison of different sources of the actual electric field strength at the serving UE position for extreme mMIMO BS with  $24 \times 16$  array and K = 8.

Since the system operates in full buffer mode, the maximum transmit power is continuously scheduled during the UE serving period. However, this traffic profile is uncommon in real networks. Consequently, the exposure to RF EMF is generally lower in real mobile networks, as documented in [30][31][32][35][33][34].

#### 6.6 Conclusions

This chapter investigates the actual EMF exposure levels generated by extreme mMIMO active antenna array systems operating at 10 GHz, which is representative of the 7-15 GHz frequency range planned for 6G. The simulations, based on 3GPP TR 38.901 [19] channel modelling guidelines and employing a full buffer traffic load, analyzed various antenna array dimensions, ranging from a 12x8 array with 192 antenna elements to a 24x16 array with 796 antenna elements. The simulations were conducted at 10 GHz, and the actual maximum approach, as described in IEC 62232 [15] was implemented.

The modelling results demonstrate that larger arrays achieve lower  $F_{PR}$  values. Using a 95<sup>th</sup> percentile approach, the  $F_{PR}$  ranged from -7.1 dB for a 12x8 array to -10.7 dB for a 24x16 array in the case of a single attached UE (K = 1). Similarly, with K = 8 UEs attached to the BS,  $F_{PR}$  values varied from -8.8 dB for a 12x8 array to -13.1 dB for a 24x16 array.

This research underscores the significance of implementing the actual maximum approach to facilitate the deployment of extreme mMIMO systems in current and future generations of mobile network systems, including 6G.

The part of the research presented in this Chapter was published in [45].

# 7. The experimental study of actual EMF exposure from Massive MIMO

## 7.1 Objectives

The primary objective of the experimental study is to investigate the spatial distribution of actual EMF exposure in close proximity to a real massive MIMO base station during operation.

The experiment was conducted in an anechoic chamber, which means the results cannot be directly compared to the modeling studies in previous Chapters that utilized a multipath radio channel model. However, the trends and behaviors observed in the experiment are expected to be similar to those predicted by the models.

To ensure consistency with the simulations, the experiment employed a similar number of simultaneously served user equipment and serving times.

### 7.2 The measurement setup

The measurements were conducted in a large anechoic chamber dedicated to Over-the-Air (OTA) testing of Massive MIMO Base Stations at the Nokia Solutions and Networks facility in Wroclaw. The chamber enables the installation of mMIMO BS on a positioner, facilitating the verification of advanced beamforming features.

The chamber's cylindrical wall is equipped with broadband dual-polarized antennas arranged in 4 rows and 24 columns. These antennas are connected to terminals through a system of fast RF switches, allowing for the simulation of various user equipment positions and movements.

In this environment, actual electromagnetic field exposure was measured for different numbers of UEs and use cases. Figure 7-1 depicts the test environment. A Selective Radiation Meter NARDA SRM 3006, equipped with a three-axis antenna capable of measuring EMF exposure from 200 MHz to 6 GHz with isotropic characteristics, was positioned near the wall. The SRM was configured with a resolution bandwidth (RBW) of 10 MHz and a recording time interval of 6 seconds. A dedicated script on a laptop connected to the EMF meter acquired measurement results, recording both instantaneous and 6-minute average electric field strength.

The Nokia mMIMO BS for the 3.5 GHz band comprises an antenna array with 64 TRXes and 192 antenna elements (12x8 antenna array). The BS was configured for a total power transmission of 320 W, with a maximum antenna gain of 24.5 dBi. The BS operated with a bandwidth of 100 MHz and utilized 6 Synchronization Signal Block (SSB) beams in azimuth for transmitting synchronization signals. The SSB includes primary and secondary synchronization signals (PSS and SSS) as well as the broadcast channel (BCH), which contains the master information block (MIB).



Figure 7-1 OTA chamber with mMIMO BS and EMF meter (Nokia Solution and Networks Laboratory in Wroclaw).

The BS employed codebook-based beamforming with 256 beams (32 horizontal beams and 8 vertical beams), as illustrated in Figure 7-2. This allows for precise beam pointing towards the antennas on the walls, particularly in the chamber where line-of-sight (LOS) propagation without multipath occurs. The codebook-based beamforming enables the selection of a single cross-polarization beam suitable for 2x2 MIMO transmission mode.

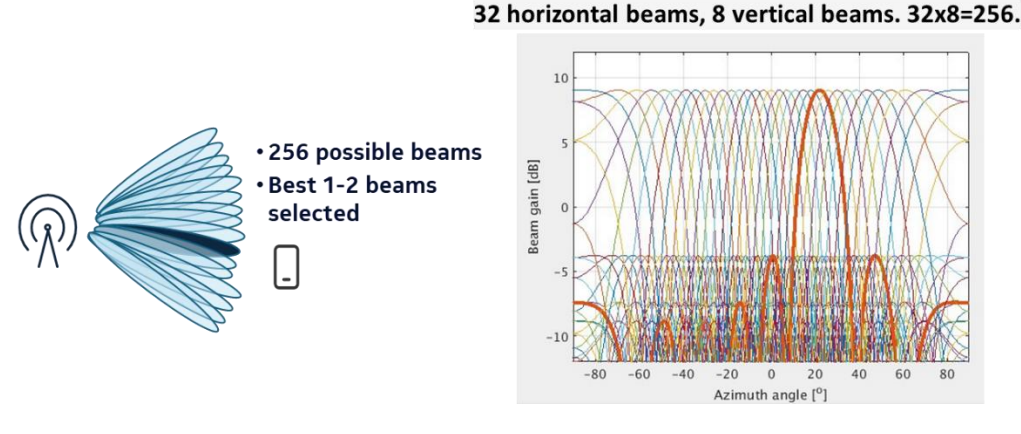


Figure 7-2 The dense codebook-based beamforming used in measurements.

The EMF meter was positioned near the wall, 10.8 meters from the center of the mMIMO BS front. The BS was down tilted to align the EMF probe with the boresight direction of the BS antenna. This configuration allowed for testing the maximum exposure from the mMIMO BS, as the antenna gain is highest in the boresight direction.

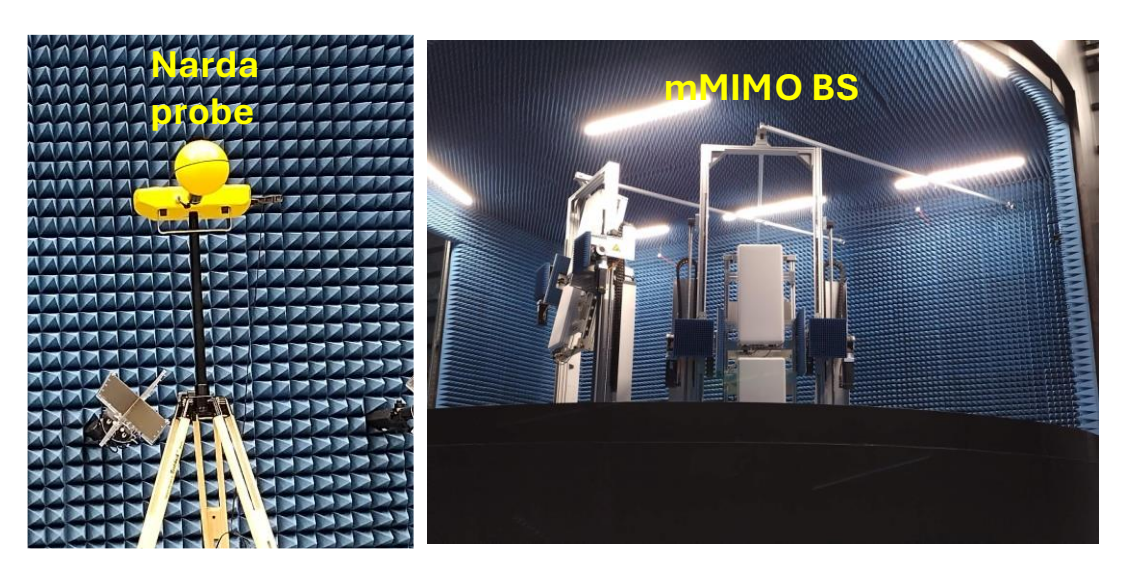


Figure 7-3 The view on EMF meter and mMIMO BS (Nokia Solution and Networks Laboratory in Wroclaw).

### 7.3 The use cases descriptions

The use cases investigated in the measurements were analogous to the parameters employed in the simulations presented in previous Chapters. The measurement duration ranged from 15 to 65 minutes, depending on the specific use case. The positions of the UEs emulated by connected antennas on the wall were randomly selected during the measurement process. This measurement time is significantly shorter than the simulation time used in the SLS tool, preventing a direct comparison between measurements and simulations. Consequently, the resulting cumulative distribution function (CDF) statistics from the measurements are not as smooth due to the limited simulation time and number of UE positions. However, the measurements enable the analysis of trends and the impact of different use cases on actual electromagnetic field exposure.

The use cases are characterized in Table 7-1 and described below:

**Use Case 1:** This baseline scenario involves directing a single beam towards a single UE. Subsequent use cases reference the EMF exposure measured in this scenario.

Use Case 2: In this scenario, the cell is empty, with no UEs present. Only the synchronization signal block (SSB) beams are transmitted.

Use Cases 3-6: These use cases assess the impact of simultaneously serving multiple UEs.

**Use Case 7:** Four UEs are simultaneously served with a drop time of 60 seconds. These UEs are randomly connected to all four rows of the wall.

Use Case 8: One UE from the use case 7 is fixed in the boresight direction.

**Use Case 9:** The impact of low throughput is evaluated with the configuration from use case 7.

**Use Cases 10:** All other use cases involve UEs in full-buffer transmission. Use Case 10 investigates the impact of varying drop times for four UEs.

Use Cases 11: The impact of moving UEs is examined on actual EMF exposure.

Table 7-1 Use Cases description.

Use Case Number	Use Case Name	Use Case Description
1	1 UE boresight	1 UE in boresight direction in fixed position, full-buffer transmission
2	SSB only	Only SSB beams are active, no UEs connected
3	1 UE static, 60s, 2 rows	1 static UE connected to lower 2 rows of antennas in wall, random position selected after 60 s, full-buffer transmission
4	2 UEs static, 60 s, 2 rows	2 static UEs connected to lower 2 rows of antennas in wall, random position selected after 60 s, full-buffer transmission
5	3 UEs static, 60 s, 2 rows	3 static UEs connected to lower 2 rows of antennas in wall, random position selected after 60 s, full-buffer transmission
6	4 UEs static, 60 s, 2 rows	4 static UEs connected to lower 2 rows of antennas in wall, random position selected after 60 s, full-buffer transmission
7	4 UEs static, 60 s, 4 rows	4 static UEs connected to all 4 rows of antennas in wall, random position selected after 60 s, full-buffer transmission
8	4 UEs static (1 UE boresight), 60 s, 4 rows	3 static UEs connected to all 4 rows of antennas in wall, 1 UE all the time in boresight position, 3 UEs in random positions selected after 60 s, full-buffer transmission
9	4 UEs static (1 UE boresight), 60 s, 4 rows, low throughput	3 static UEs connected to all 4 rows of antennas in wall, 1 UE all the time in boresight position, 3 UEs in random positions selected after 60 s, low throughput transmission
10	4 UEs static (1 UE boresight), 180 s, 4 rows	3 static UEs connected to all 4 rows of antennas in wall, 1 UE all the time in boresight position, 3 UEs in random positions selected after 60 s, full-buffer transmission
11	4 UEs moving, 4 rows	4 UEs moving connected to 4 rows of antennas in wall, pedestrian speed (3 km/h)

## 7.4 The analysis of actual EMF exposure for various use cases

Figure 7-4 presents the measurement results from use case 1. The CDF displays the 6-minute averaged actual electric field strength and the maximum instantaneous electric field strength. This reference use case involves continuous transmission through a single beam towards a fixed UE. Consequently, the average electric field strength remains relatively constant.

The maximum average electric field strength measured was 133.4 V/m, exhibiting a minimal difference of 1.5 V/m compared to the calculated value of 131.9 V/m. This use case exemplifies the maximum radiated power approach employed for compliance distance estimation.

The measurements indicate that a distance of 10.8 meters from the massive MIMO base station is insufficient during continuous transmission in a single direction, as the measured electric field strength significantly exceeds the limit of 61 V/m.

The plot also depicts the instantaneous maximum value of the electric field strength, which is notably higher and more dispersed than the average value. This behavior is attributed to the characteristics of the OFDM waveform, which exhibits a high peak-to-average power ratio (PARP) resulting in significant power peaks.

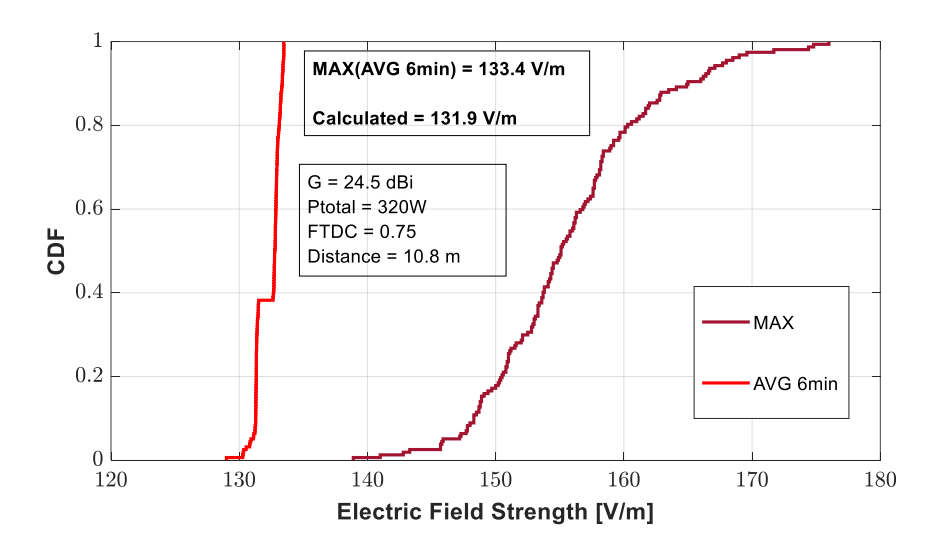


Figure 7-4 Measured CDFs for Use Case 1- fixed UE in boresight.

The measured maximum average electric field strength of 133.4 V/m serves as a reference point for comparison with other use cases.

When the cell is unoccupied, only the SSB beams are transmitted. Figure 7-5 depicts the measured average electric field strength, calculated over a six-minute interval. The measured electric field strength in this scenario is relatively low, ranging from 1.6 to 2.2 V/m.

The impact of the number of simultaneously served UE) on actual EMF exposure was investigated in use cases 3-6. The results are presented in Figure 7-6, with measurements referenced to the maximum exposure observed in use case 1.

Analysis of the data reveals that the  $95^{th}$  percentile of normalized electric field strength ( $F_{PR}$ ) decreases as the number of UEs increases. Conversely, the median normalized electric field strength exhibits an upward trend with an increasing number of served UEs. Notably, the maximum electric field strength remains relatively consistent for 1-2 and 3-4 UEs. This observation is attributed to insufficient measurement time and limited UE positions. Specifically, during the measurements, no UE was positioned directly in the boresight direction.

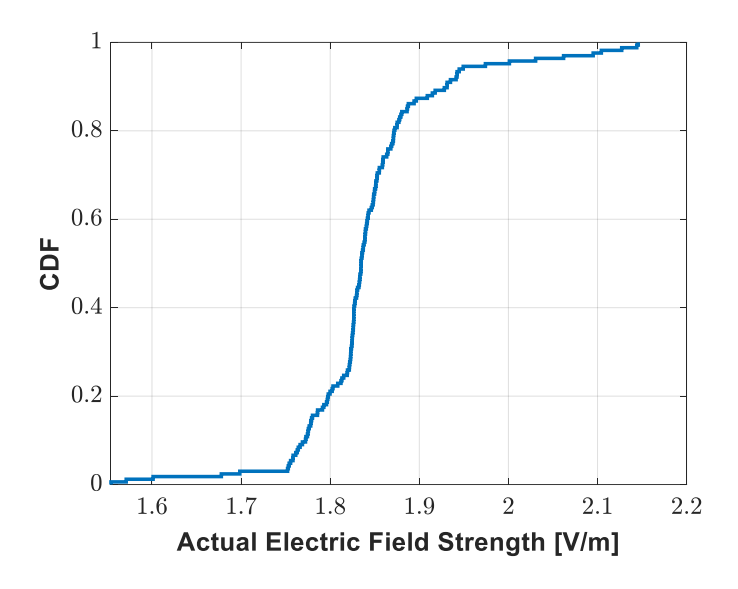


Figure 7-5 Measured CDF of Use Case 2- empty cell, only SSB beams.

Despite these limitations, the trends observed in the cumulative distribution functions and the power reduction factor characteristic align with the measurement results presented in Chapters 6 for the mMIMO 12x8 array.

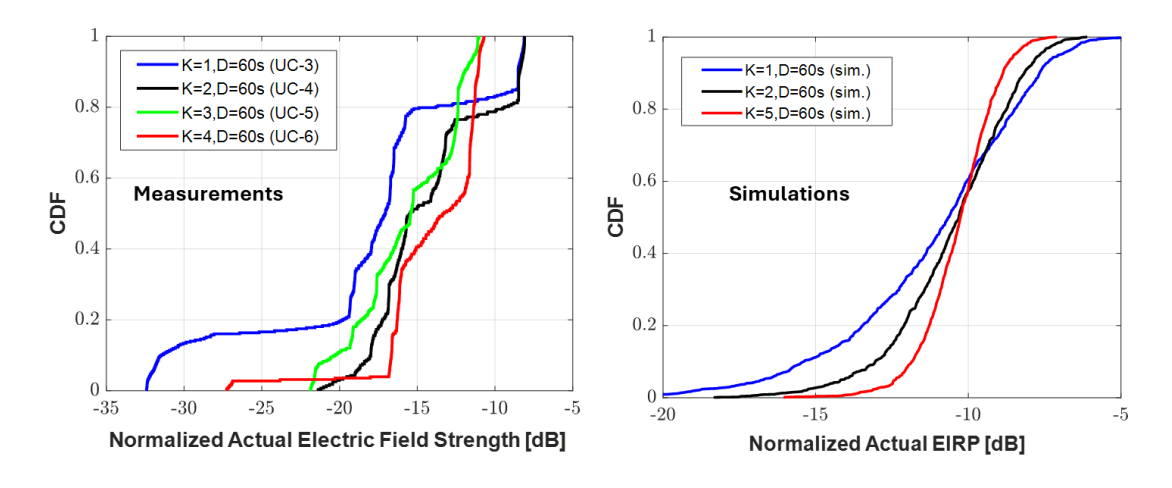


Figure 7-6 Measurement results for Use Cases 3-6 – impact of number of served UEs (left). Simulation results from Chapter 5 (right).

Figure 7-7 presents the measurement results from use cases 7-10. These use cases involved four UEs devices connected simultaneously, each with distinct configurations.

In use case 8, where one UE was fixed in the boresight direction, an increase in electromagnetic field exposure was observed with comparison to use case 7 where all UEs were randomly distributed. This is attributed to a single beam continuously radiating towards the location of the EMF probe. Despite this, the  $F_{PR}$  remained low, approximately -8 dB, indicating an electric field strength level below 61 V/m (around 53 V/m).

Use case 9 compared measurements for low throughput service (approximately 10 Mb/s) with full-buffer transmission (exceeding 700 Mb/s). The low throughput scenario utilized fewer

Physical Resource Blocks compared to the full-buffer scenario, which resulted in significantly lower transmission power and EMF exposure.

The impact of transmission time was investigated in use case 10, comparing durations of 60 seconds and 180 seconds. The longer transmission time (180 seconds) exhibited a steeper cumulative distribution function compared to the shorter duration. This resulted in a higher  $F_{PR}$  for the longer transmission time, particularly at the 95<sup>th</sup> percentile, while the median value decreased. This trend aligns with the observations from simulation results.

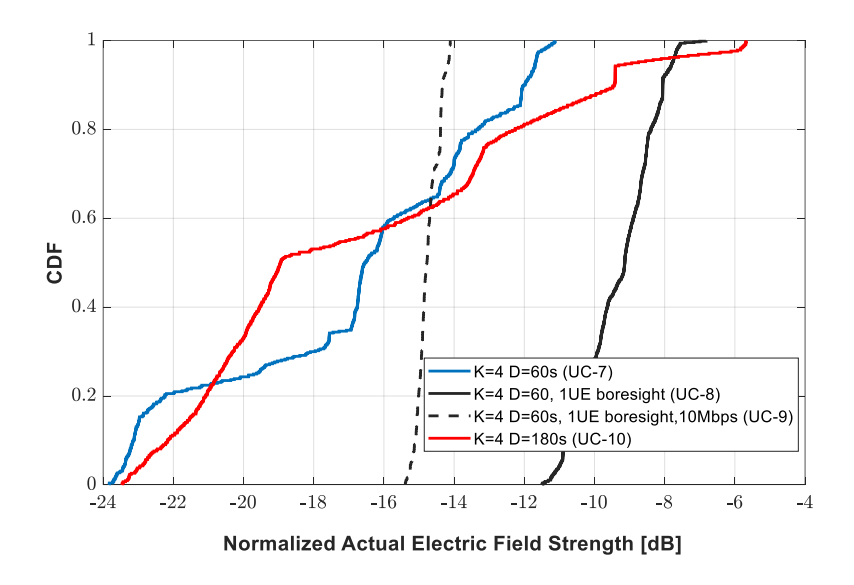


Figure 7-7 Measurement results of Use cases 7-10 – impact of transmission time, throughout and fixed UE position.

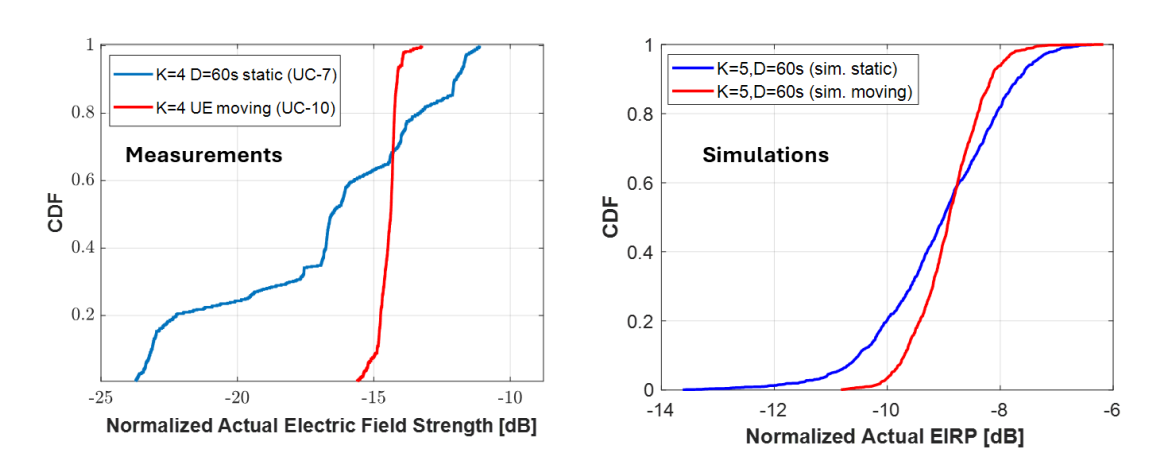


Figure 7-8 Measurement results of Use Case 11 (left) and simulation results from Chapter 4 (right) – comparison of static and moving UE

Use case 11 investigated the impact of a moving UE on measurement results (Figure 7-8). Compared to static UE positions, the maximum and 95<sup>th</sup> percentile values of the electric field strength decreased when the UE was in motion. Additionally, the CDF curve for the moving UE scenario exhibited a more concentrated distribution within a limited range. This is attributed to the rapid switching of beams, resulting in a higher frequency of beams directed towards the

EMF probe compared to the static UE scenarios with infrequent position changes. These observations align with the findings presented in Chapter 4, which focused on the impact of a moving UE.

### 7.5 Summary

This Chapter presents the results of an experimental study conducted in a specialized OTA chamber designed for testing mMIMO base station. The study evaluated actual electromagnetic field exposure in various use cases.

The findings indicate that for all practical use cases, the actual EMF exposure remained below the ICNRIP requirement of 61 V/m at a close distance from the mMIMO base station (approximately 10.8 meters). This result was achieved despite the use of full-buffer transmission during measurements, which is not representative of typical telecommunication traffic. Additionally, the chamber provided near-ideal radio propagation conditions, and beam switching occurred less frequently than in typical beamforming algorithm operations in real networks.

These experimental results align with the trends observed in simulations conducted in previous Chapters.

The measurement results indicate that the maximum approach outlined in IEC62232 [15], and investigated in this thesis, is suitable for practical implementation in massive MIMO (mMIMO) base stations. Simulation studies and measurements consistently indicate that the average EMF exposure surrounding mMIMO base stations during operation is significantly lower than the exposure levels observed at maximum radiated power. This approach allows for the deployment of mMIMO base stations with considerably reduced compliance distances.

In real-world scenarios, the actual EMF exposure is likely to be even lower than observed in the study [46]. This is because high-load traffic conditions are not sustained continuously, and beam switching occurs more frequently than in the test environment. The field results available in [65] shows that  $F_{PR}$  values are in the range of -14 dB to -7.2 dB for 64TRX antenna. The variability of this parameter depends on load and maximum value close to -7 dB (the highest load in the network) is on the similar level presented in simulation results for similar antenna setup used in this thesis (see Chapter 3.2).

The measurement results emphasize the critical need for further research into modeling electromagnetic field exposure from mMIMO base stations. The findings demonstrate the complex interplay of various factors influencing EMF exposure and underscore the importance of considering diverse use cases, as highlighted in the thesis.

# 8. Actual RF emissions control for multiantenna systems with beamforming

## 8.1 Introduction to EIRP control for actual EMF exposure

The core principle of the actual maximum approach method involves determining the power reduction factor, which accounts for both spatial beam variations and temporal traffic fluctuations. This factor can be derived through computational modeling, simulating realistic 5G system operating conditions, or by analyzing measurements from operational base stations. Previous Chapters have extensively explored this problem, evaluating actual EMF exposure from mMIMO systems under diverse conditions and operational scenarios.

The F<sub>PR</sub> value plays a crucial role in a specialized feature designed for actual exposure control within mMIMO BS. This feature aims to ensure that the time-averaged EIRP remains below a predefined threshold, calculated over intervals of 6 or 30 minutes. When the actual EIRP control approaches this threshold, the feature triggers mechanisms to reduce exposure. However, EIRP reduction could directly impacts cell coverage and capacity, necessitating optimization techniques.

To mitigate the effects of EIRP control, the controlled area is divided into spatial segments, enabling individual EMF exposure control within each segment [46][47]. This approach is illustrated in Figure 8-1 and Figure 8-2.

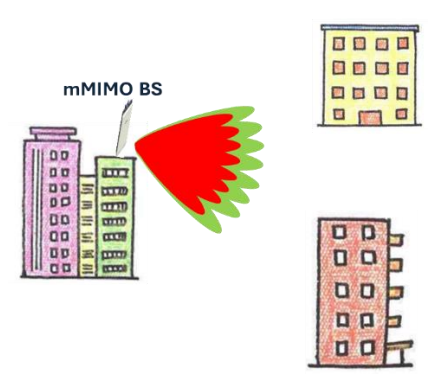


Figure 8-1 Illustration of EIRP control without segments (green – EIRP control disables, red – EIRP control enabled).

When EIRP control is implemented across the entire sector without spatial segmentation (Figure 8-1), triggering the control mechanism reduces EIRP across the entire sector. This affects all UEs within the sector's coverage, even those in areas not requiring protection. For instance, consider two buildings near the mMIMO BS deployment like in Figure 8-1. The actual maximum EMF exposure approach should only operate in these directions. However, the street between these buildings is significantly farther from the BS than the buildings themselves, rendering EIRP control unnecessary in this area. Nevertheless, sector-based EIRP control impacts the performance of all UEs.

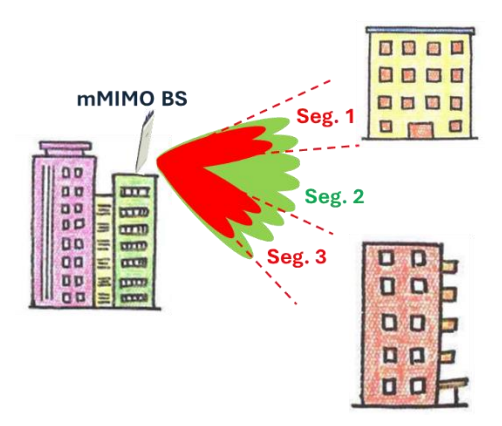


Figure 8-2 Illustration of EIRP control with segments (green – EIRP control disables, red – EIRP control enabled).

In contrast, the segment approach illustrated in Figure 8-2 divides the area into segments with individual EIRP control. This strategy allows for targeted EMF exposure control only in segments requiring it, such as segments containing buildings adjacent to the mMIMO antenna. Segments without nearby buildings do not necessitate control. In the example illustrated in Figure 8-2, Segment 2 does not require control, ensuring UE performance in this area remains unaffected. However, Segments 1 and 2 may require EIRP control due to the proximity of buildings to the mMIMO BS. This control would be triggered individually when the threshold is exceeded within the respective segment.

Field trials conducted in a commercial network, as presented in [14], indicate that EIRP control activation averaged 16 seconds per day without segmenting and 2 seconds per day with segmenting.

Currently, EIRP control is achieved by reducing transmit power [48][49]. These techniques and their impact on capacity are discussed in the next Section. However, mMIMO technology offers the potential to design algorithms that optimize beamforming to regulate antenna gain in specific directions. This Chapter presents two novel algorithms developed by the author. The first algorithm focuses on codebook-based beamforming with a GoB approach (Section 8.3). The second algorithm, designed for advanced reciprocity-based beamforming, optimizes EIRP control within the segment approach (Section 8.4).

# 8.2 The impact of various techniques of EIRP control for system performance

The power density (S, measured in W/m²) of EMF exposure is directly proportional to the EIRP level of the base station and distance, as illustrated in Figure 8-3. Simultaneously, the received power ( $P_{rx}$ , measured in W) at a UE is determined by the power density (S) and the UE antenna gain ( $G_{rx}$ ) at the UE's location. Consequently, reducing the EIRP directly impacts the received power and data transmission throughput.

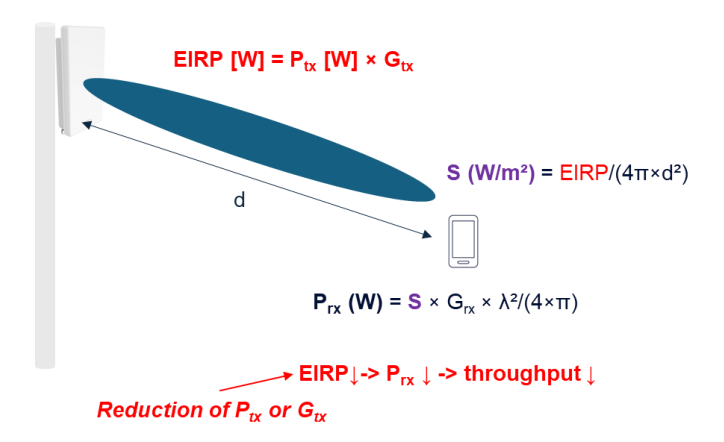


Figure 8-3 Illustration of the impact of EIRP on power density (EMF exposure) and received power in free space conditions.

When implementing the actual maximum approach in mMIMO BS, the power reduction factor  $F_{PR}$  is determined based on statistical evaluation or measurements. The EIRP monitoring function within the BS measures the average EIRP. If this value approaches the threshold, the EIRP control mechanism temporarily reduces the EIRP level. Previous analyses have demonstrated that the probability of high EMF exposure, and consequently high EIRP transmission in a single direction, is very low. However, such use cases are not prohibited. Sporadic instances may occur, such as a single UE in a long, static position within the cell or hotspots with numerous UEs in dense areas requiring high-speed data transmission.

The reduction of EIRP has a direct impact on received power and subsequently on throughput, as evident from the Nyquist-Shannon formula:

$$C = B \times log_2(1 + \frac{P_{rx}}{B \times N_0 + I})$$
 Equation 8-1

where:

C – capacity in b/s

B – bandwidth in Hz

 $P_{rx}$  – received power in W

N<sub>0</sub> – thermal noise density (W/Hz)

I – interference power in W

Currently, the primary techniques for controlling EIRP involve reducing transmit power. This can be achieved through various methods, as described below:

#### a) Reduction of PDSCH power:

PDSCH (Physical Downlink Shared Channel) occupies a significant portion of the bandwidth, making the transmit power level ( $P_{tx}$ ) a major factor influencing  $P_{rx}$  and throughput. Reducing PDSCH power directly impacts capacity:

$$C \downarrow = B \times log_2(1 + \frac{P_{rx} \downarrow}{B \times N_0 + I})$$
 Equation 8-2

Examples of direct P<sub>tx</sub> control with optimization are presented in publication [49].

#### b) Reduction of allocated PRBs of PDSCH channel (bandwidth reduction)

The power density of each PRB is fixed. Reducing the number of PRBs allocated to PDSCH decreases the total  $P_{tx}$ , leading to reduced  $P_{rx}$  and throughput:

$$C \downarrow = B \downarrow \times log_2(1 + \frac{P_{rx}\downarrow}{B\downarrow \times N_0 + I})$$
 Equation 8-3

Optimization techniques exist, and one method that ensures smooth EIRP control by preventing resource shortage is presented in [50].

#### c) Reduction of modulation order

Lowering the modulation order (e.g., changing 64QAM to 32QAM) requires a lower SINR for reliable demodulation. This allows for a reduction in the transmit power level ( $P_{tx}$ ), consequently decreasing  $P_{rx}$  and throughput, as illustrated in Figure 8-4.

$$C \downarrow = B \times log_2(1 + \frac{P_{rx} \downarrow}{B \times N_0 + I})$$
 Equation 8-4

An optimization technique that allocates more PRBs for data transmission after reducing the modulation order to compensate for the loss is presented in paper [48].

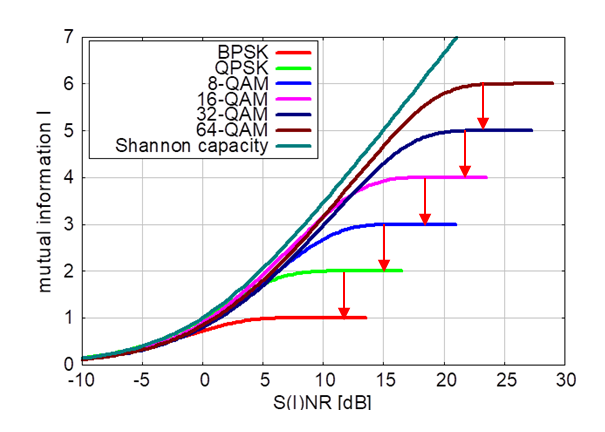


Figure 8-4 EIRP control by reduction of modulation order.

The reduction of EIRP through direct control of  $P_{tx}$  (techniques a and c) or bandwidth (technique b) has varying effects on capacity depending on the SINR level. The Nyquist-Shannon formula indicates that capacity grows linearly with power for low SINR levels, but

for medium and high SNR, capacity grows linearly with bandwidth. This characteristic directly impacts the efficiency of different EIRP control methods.

Figure 8-5 shows the resultant capacity ratio (100% means full available capacity) compared between technique a (direct  $P_{tx}$  control) and technique b (indirect  $P_{tx}$  control by bandwidth reduction) calculated for different levels of EIRP control (-3 dB, -6 dB, and -9 dB).

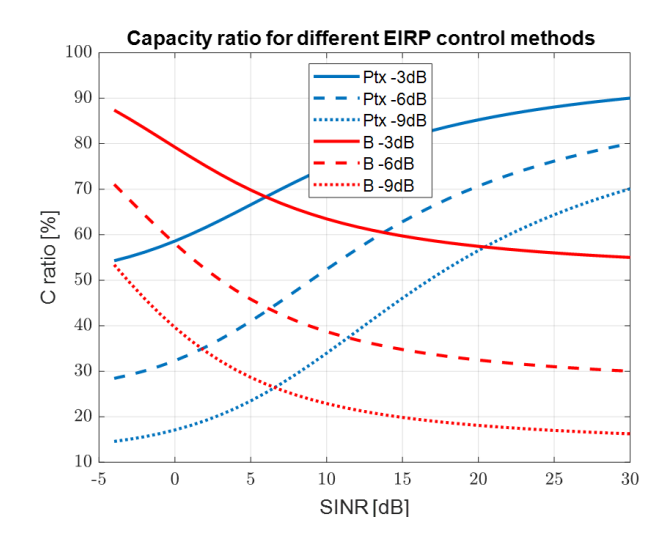


Figure 8-5 The comparison of EIRP control calculated by direct reduction of transmit power or indirect reduction of transmit power by bandwidth reduction.

We observe that direct reduction of power is more efficient for medium and high SINR, while indirect reduction of power through bandwidth reduction is more effective for low SINR levels (cell edge UEs). The intersection point occurs at approximately SINR = 6.5 dB. The difference is significant; for example, for an EIRP control level of -6 dB:

- SINR = 0 dB:
  - $\circ$  Reduction of transmit power  $C_{ratio} = 35\%$
  - $\circ$  Reduction of bandwidth  $-C_{ratio} = 60\%$
- SINR = 20 dB:
  - Reduction of transmit power  $C_{ratio} = 70\%$
  - $\circ$  Reduction of bandwidth  $-C_{ratio} = 32\%$

This indicates that practical implementation of EIRP control should employ different techniques to minimize capacity loss for varying SINR levels.

This Section focused on EIRP control through transmit power management. The following Sections will explore solutions for optimal EIRP control using antenna gain reduction.

# 8.3 The optimal beam broadening method for EIRP control in codebook-based beamforming

## 8.3.1 Principles of the effective antenna gain in real propagation environment

The performance of an antenna is typically characterized by its nominal antenna pattern, measured in an anechoic chamber. This controlled environment emulates ideal free space propagation with minimal multipath effects. However, real-world propagation environments, particularly in urban deployments, are characterized by significant multipath propagation, especially in NLOS conditions. This multipath propagation distorts the nominal antenna pattern, as documented in [51][52][27][28][53][54][55].

Figure 8-6 and Figure 8-7 illustrates the difference between the nominal antenna pattern measured in an anechoic chamber (or free space propagation with a strong line-of-sight path) and the distorted pattern observed in a real-world propagation environment with significant multipath. The real channel distorts the antenna pattern primarily by broadening the beamwidth, leading to a reduction in effective antenna gain.

This phenomenon can be visualized by comparing the propagation of light waves in clear weather and foggy or snowy conditions as shown also on Figure 8-6 and Figure 8-7. In clear weather, turn-on light beams from car reflectors or lanterns are narrow and have a long range. However, fog or snow particles distort the light waves, causing the beams to widen and shorten their range.

While both radio waves and light waves are electromagnetic waves, their wavelengths differ significantly. In the case of radio waves, objects surrounding the transmitter and receiver cause the multipath effects. For light waves, with their much shorter wavelengths, fog or snow particles are the primary contributors to propagation distortion.

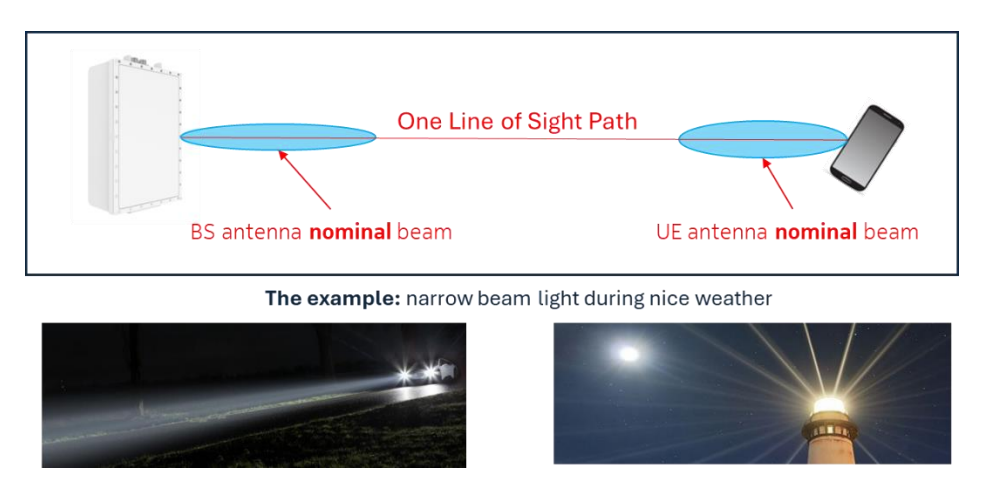


Figure 8-6 Illustration of ideal nominal antenna pattern in anechoic chamber.

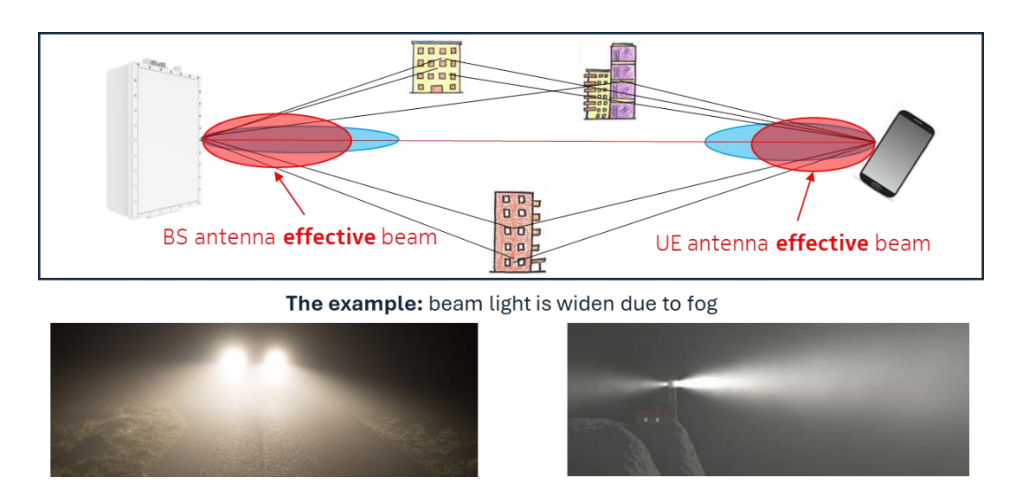


Figure 8-7 Illustration of effective antenna pattern in multipath environment.

As demonstrated in [28][53] the effective antenna pattern and gain are significantly impacted when the angular spread of the channel approaches or exceeds the RMS of the antenna beamwidth. This is particularly true for narrow, directional beams like those used in GoB beamforming. The channel angular spread effectively "widens" these beams, leading to a degradation of effective beamforming gain, especially for UEs in NLOS conditions.

Figure 8-8 presents examples of measurements of effective antenna patterns and effective antenna gain in real propagation environments, as published by Nokia Bell Labs in [51] and [54].

In the Figure 8-8 we have the following examples of measurements:

- a) Effective azimuth antenna gain in O2I environment with buildings with modern low-emissivity (low-e) and single-glazed ("traditional") windows, Figure 6 from [51]:
  - o This Figure illustrates the impact of different building materials on effective antenna gain in an indoor-to-indoor environment.
- **b**) Sample azimuth effective antenna pattern in factory LOS environment (solid) and in anechoic chamber (dashed), Figure 10 from [54]:
  - o This Figure compares the effective antenna pattern in a factory LOS environment with the nominal pattern measured in an anechoic chamber.
- c) Sample azimuth effective antenna pattern in factory NLOS environment (solid) and in anechoic chamber (dashed), Figure 11 from [54]:
  - o This Figure compares the effective antenna pattern in a factory NLOS environment with the nominal pattern measured in an anechoic chamber.

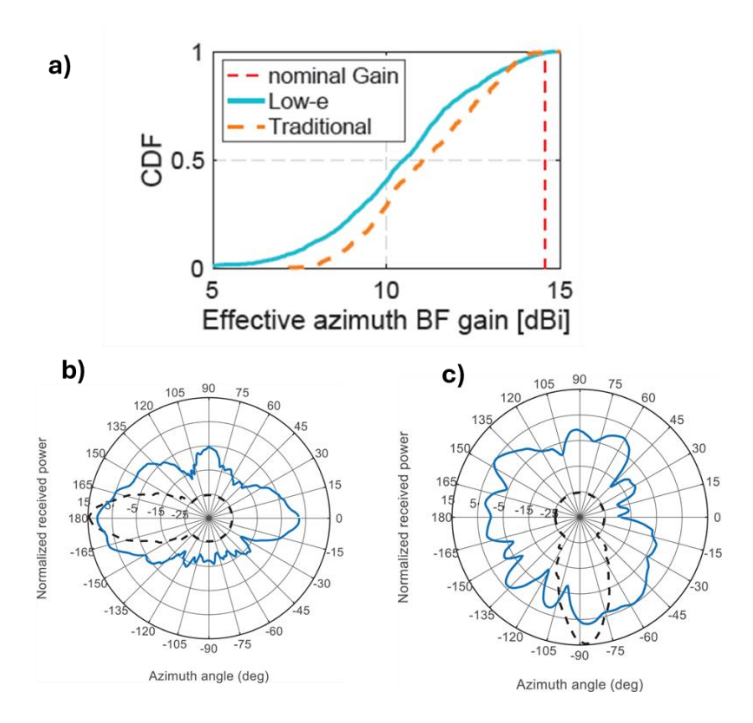


*Figure 8-8 The measurement results of effective antenna gain and patterns:* 

- a) Effective azimuth antenna gain in O2I environment with buildings with modern low-emissivity (low-e) and single-glazed ("traditional") windows, Figure 6 from [51]
- b) Sample azimuth effective antenna pattern in factory LOS environment (solid) and in anechoic chamber (dashed), Figure 10 from [54]
- c) Sample azimuth effective antenna pattern in factory NLOS environment (solid) and in anechoic chamber (dashed), Figure 11 from [54].

These Figures provide valuable insights into the differences between nominal antenna patterns measured in controlled environments and the actual performance observed in real-world propagation scenarios. They highlight the importance of considering the impact of multipath and other environmental factors on antenna performance in practical deployments. It accurately captures the key takeaway: the discrepancy between idealized antenna performance in controlled environments and the real-world performance impacted by multipath and other environmental factors. This understanding is crucial for optimizing antenna design and deployment strategies in practical applications.

To mitigate this substantial antenna gain degradation, advanced digital beamforming schemes are required. These schemes rely on accurate channel state information (CSI) and dynamic adaptation of the antenna pattern to the specific radio channel realization. However, obtaining accurate CSI is challenging. Therefore, in such conditions, codebook-based beamforming with dense GoB offers better reliability, even if its performance is lower than advanced beamforming schemes [37].

The concept of an optimal antenna array, described in [28] [53], aims to minimize the impact of angular spread on effective antenna gain by optimizing the array size. This study revealed that the angular spread is significantly greater in the azimuth direction compared to the elevation

direction in most typical radio channels. Consequently, effective antenna gain is more substantially impacted in the azimuth plane.

The effective antenna gain ( $G_{eff}$ ) affected by angular spread in the real channel can be estimated using the following formulas [18]:

$$G_{eff} = NG_e = \frac{2}{B_h B_v}$$
 Equation 8-5  
 $B_h = \sqrt{B_{ho}^2 + ASD^2}$  Equation 8-6  
 $B_v = \sqrt{B_{vo}^2 + ZSD^2}$  Equation 8-7

#### Where:

- N: Number of antenna elements
- Ge: Antenna element gain
- B<sub>h</sub>, B<sub>v</sub>: RMS antenna beamwidth in azimuth and elevation, respectively (in radians)
- B<sub>ho</sub>, B<sub>vo</sub>: Nominal RMS antenna beamwidth in azimuth and elevation, respectively (in radians)
- ASD, ZSD: RMS azimuth spread of departure and zenith spread of departure, respectively (in radians)

Nominal RMS antenna bandwidth can be estimated using the following formulas, valid for beams with a Gaussian shape, typical for antenna arrays:

$$B_{h0} = \frac{HPBW_{h0}}{2\sqrt{\ln{(4)}}}$$
 Equation 8-8
$$B_{v0} = \frac{HPBW_{v0}}{2\sqrt{\ln{(4)}}}$$
 Equation 8-9

#### Where:

• HPBW<sub>h0</sub>, HPBW<sub>v0</sub>: Nominal half-power (3 dB) beamwidth in the azimuth and the elevation planes, respectively (in radians)

For example, an 12x12 array with an antenna element gain of 5 dBi and a radio channel angular spread of ASD =  $17^{\circ}$  and ZSD =  $2^{\circ}$  results in an effective antenna gain of 19.4 dBi, compared to a nominal antenna gain of 26.5 dBi (7.1 dB of gain degradation).

This Section highlights the importance of considering the impact of real-world propagation environments on antenna performance. While nominal antenna patterns provide a useful

starting point, understanding the effects of multipath propagation and angular spread is crucial for optimizing antenna design and beamforming strategies in practical deployments.

#### 8.3.2 Beam broadening algorithm for actual EIRP control

The effective antenna gain of an antenna array saturates when the RMS beamwidth approaches or exceeds the angular spread of the propagation channel. Consequently, increasing the number of antenna elements to reduce the beamwidth does not significantly enhance gain in real-world propagation environments.

In the context of EMF exposure assessment near mMIMO BS, such as those deployed on building rooftops for 5G services, areas accessible to people are typically located in LOS conditions. Conversely, UEs locations can be either LOS or NLOS. Urban environments predominantly feature indoor UEs (so NLOS), while LOS probability in outdoor areas remains low. For instance, in Urban Macro (UMa) scenarios, LOS probability falls below 30% for distances exceeding 100 meters between the BS and UE [19]. Therefore, the effective antenna pattern at most UE positions is influenced by the angular spread of multipath propagation.

The angular spread in the Azimuth Domain (ASD) is generally larger than the angular spread in the Zenith Domain (ZSD) in typical propagation conditions [19][27][28]. This leads to a more pronounced degradation of the antenna pattern, and consequently, the effective antenna gain, in the horizontal plane. This phenomenon has been leveraged to develop a beam broadening algorithm for optimal EIRP control.

When EIRP control is not activated, the mMIMO BS employs beams with default gain to maximize performance. If the radio channel exhibits sufficient angular spread in azimuth, the effective gain of these beams at the UE's location is lower compared to the immediate vicinity of the BS. When the EIRP control algorithm is triggered due to the time-averaged EIRP approaching the EMF exposure limit, the beam is broadened. This broadening ensures that the effective gain at the UE location is minimally reduced compared to the case with disabled EIRP control. Simultaneously, this solution reduces EMF exposure in the close proximity to the BS, as the antenna gain in LOS conditions decreases directly due to the wider beamwidth and lower angular spread. Consequently, the UE experiences minimal performance degradation at its NLOS position, as the effective gain remains similar. This is because the angular spread of the radio channel introduces less distortion to beams with broader beamwidths compared to narrower beams. The concept of the idea is illustrated in Figure 8-9 below.

Figure 8-10 illustrates the flowchart of the proposed algorithm's generic design. Step 1 involves estimating the ASD. A simple and validated method, based on measuring the uplink pilot signal strength by the BS using a reconfigurable antenna array, was proposed in [53] and could be adopted for this purpose. In step 2, the nominal horizontal beamwidth of the antenna,  $B_{h0}$ , is calculated using formula (4). Step 3 compares the estimated ASD with  $B_{h0}$ . If the ASD is greater than or equal to  $B_{h0}$ , the algorithm proceeds to step 4, where the effective horizontal beamwidth,  $B_{h}$ , is calculated using formula (2), which accounts for the impact of the radio channel's angular spread. The broadening factor, FB > 1, introduced in step 5 allows for the assumed broadening

of the effective beamwidth,  $B_{broad\_eff}$ , calculated in step 6. Subsequently, step 7 calculates the nominal broadened beamwidth,  $B_{broad\_nom}$ , which is then applied for transmission in step 8.

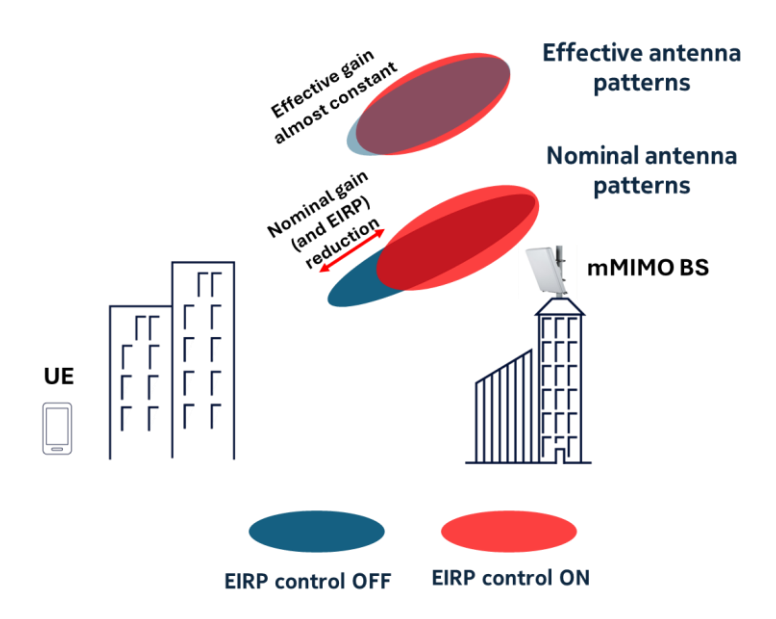


Figure 8-9 Illustration of beam broadening method for EIRP control.

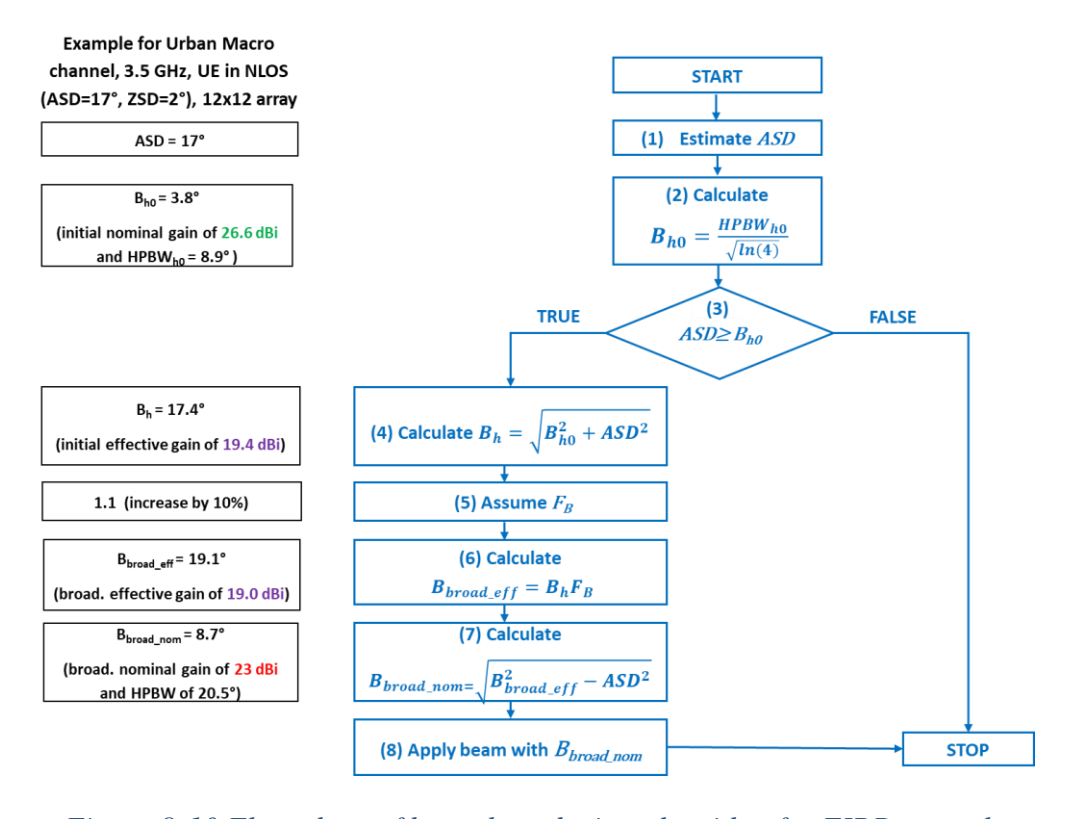


Figure 8-10 Flow chart of beam broadening algorithm for EIRP control.

Figure 8-10 demonstrates also the algorithm's output for a 12x12 antenna array and a radio channel with an ASD of  $17^{\circ}$  and a ZSD of  $2^{\circ}$  (representative of a UMa NLOS channel at 3.5 GHz [19]). The effective beamwidth of this antenna ( $B_h = 17.4^{\circ}$ ) is the same as the angular spread in azimuth of the channel, triggering the beam broadening algorithm.

The algorithm produces a nominal beam that is 2.3 times broader (20.5° vs 8.9°), resulting in a 3.6 dB degradation in nominal gain (and thus EIRP) (23 dBi vs 26.6 dBi). However, the effective gain at the UE position for this channel remains nearly constant (19.0 dBi vs 19.4 dBi), effectively ensuring minimal performance loss.

#### 8.3.3 Verification of beam broadening algorithm

The algorithm presented in previous Section was verified by analytical calculations, system level simulations and measurements.

#### 8.3.3.1 Analytical calculations

Table 8-1 presents examples of angular spread in azimuth for UMa NLOS and O2I NLOS channels, as defined in 3GPP 38.901 [19]. The angular spread in azimuth (ASD) is modeled using a Gaussian distribution. The table displays the median ( $\mu_{ASD}$ ) and values corresponding to one and two standard deviations ( $\sigma_{ASD}$ ) from the median, representing a 95% confidence interval. In the table also the typical values of beamwidth of array (half-power and RMS beamwidth) with different number of antenna elements are shown for comparison with angular spreads. The observed ASD values generally exceed the RMS antenna beamwidths, indicating that a beam broadening algorithm could be effectively applied in most multipath environments. The angular spread in zenith (ZSD) is significantly smaller than the ASD, typically ranging from 0.5° to 5° for these channel models.

Table 8-1 The typical distribution of ASD in UMa and O2I NLOS channels as compared to beamwidth of antenna arrays with different number of elements.

# 3GPP 38.901 UMa NLOS ASD [°] μ<sub>ASD</sub> 27 μ<sub>ASD</sub> 14 μ<sub>ASD</sub> - 2×σ<sub>ASD</sub> 7.5 3GPP 38.901 O2I NLOS

	ASD [°]
$\mu_{ASD}$	17.8
$\mu_{ASD}$ - $\sigma_{ASD}$	6.8
μ <sub>ASD</sub> -2×σ <sub>ASD</sub>	2.6

Antenna Array beamwidth in azimuth

Number of Antenna Elements	Half power beamwidth [°]	RMS beamwidth [°]
4	26.8	11.4
8	13.4	5.7
12	8.9	3.8
16	6.7	2.9

The following analytical calculations, based on the formulas presented in the previous Section and illustrated in Figure 8-10, will be discussed. The calculations were performed for an 8x20 (VxH) mMIMO antenna array with an element gain (G<sub>e</sub>) of 5 dBi, resulting in a

nominal azimuthal half-power beamwidth (HPBW) of 4.5° and a nominal antenna gain of 27 dBi. Figure 8-11 depicts the effective and nominal gains of the antenna array as the HPBW is broadened from 4.5° to 6.7°, 8.9°, 13.4°, and 26.8°. These HPBW values correspond to reducing the number of antenna elements in the horizontal dimension from 20 to 16, 12, 8, and 4, respectively.

The effective gain was calculated using the UMa O2I radio channel model , characterized by a mean angular spread distribution (ASD) of  $\mu_{ASD}=17.8^{\circ}$  and a standard deviation  $\sigma_{ASD}=2.63^{\circ}$ . Additionally, the effective gain was estimated for ASD values of  $6.8^{\circ}$  ( $\mu_{ASD}$  -  $\sigma_{ASD}$ ) and  $2.6^{\circ}$  ( $\mu_{ASD}$  -  $2\times\sigma_{ASD}$ ) to demonstrate the channel effect for lower angular spread values, modeled by a Gaussian distribution in 3GPP. A zenith spread distribution (ZSD) of  $2^{\circ}$  was selected for the elevation plane.

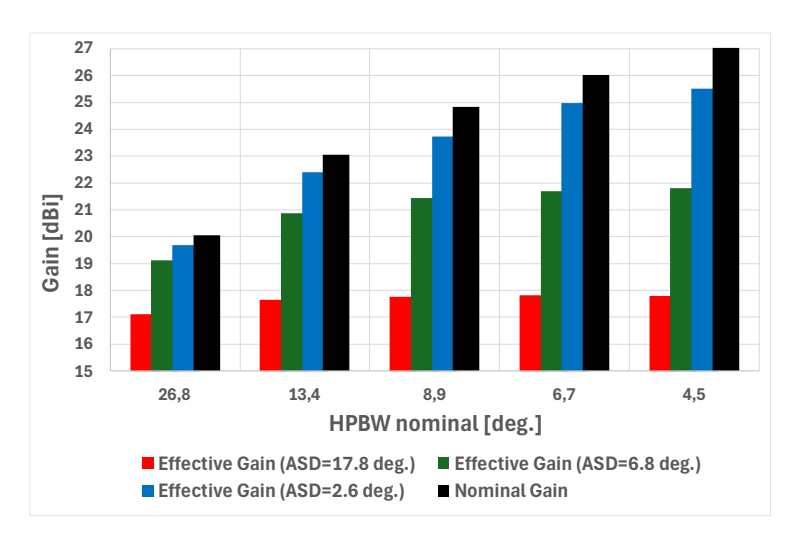


Figure 8-11 Analytical calculations of effective antenna gain in a case of beam broadening.

The results demonstrate that the effective gain of the antenna for the mean ASD of  $17.8^{\circ}$  is significantly lower than the RMS nominal gain. Broadening the beam from  $4.5^{\circ}$  to  $26.8^{\circ}$  (six times) reduces the nominal gain (and EIRP) by 7 dB, but the effective gain is reduced by only 0.7 dB. Similarly, the effective gain is reduced by only 0.16 dB when the beam is broadened three times (from  $4.5^{\circ}$  to  $13.4^{\circ}$ ), resulting in a 4 dB reduction in EIRP in close proximity to the base station. For a  $\mu_{ASD}$  -  $\sigma_{ASD}$  =  $6.8^{\circ}$ , the effective gain is reduced by only 0.9 dB when the beam is broadened three times, while the nominal gain is reduced by 4 dB. However, for the case of a small angular spread ( $\mu_{ASD}$  -  $2\times\sigma_{ASD}$  =  $2.6^{\circ}$ ), beam broadening is less effective. Broadening the beam from  $4.5^{\circ}$  to  $8.9^{\circ}$  reduces the effective gain by 1.8 dB, while the nominal gain (and EIRP) is reduced by 2.2 dB, resulting in a difference of only 0.4 dB.

#### 8.3.3.2 System level simulations

The impact of beam broadening was investigated through system-level simulations utilizing a 3D statistical spatial radio channel model [19]. These simulations validated the influence of angular spread on statistically distributed UEs positions, characterized by varying radio channel realizations and, consequently, different angular spreads. The same simulation tool employed in previous Chapters was utilized in this study, configured with the key parameters outlined in Table 8-2.

*Table 8-2 System level simulations assumptions.* 

Parameter	Value
Channel model	3GPP 38.901 urban macro (UMa)
Carrier frequency	3.5 GHz
Channel bandwidth	20 MHz
Sub-carrier spacing	30 kHz
Max total Tx power of BS (without losses)	53 dBm (200W)
Antenna Array Size [VxH]	8×8 and 8×4
Gain of BS single antenna element	5.2 dBi
Electrical down-tilt of BS antenna	5°
Height of BS antenna array centre	25 m
No. of cells / No. of sectors	7 / 21
Inter-site distance	1000 m
Type of UE antenna	Omnidirectional
SU-MIMO maximum rank	2
Beamforming type	GoB (25×45 beams)
UE distribution	20% outdoor 1.5 height, 80% indoor
No. of simultaneously served UEs	1
UE serving time	360s

The simulated cellular network comprised seven sites, each with three sectors (totaling 21 cells), and a mMIMO BS in each sector. Each BS was positioned at a height of 25 meters, with an inter-site distance of 1000 meters. The system operated at a frequency of 3.5 GHz, with a 20 MHz channel bandwidth, a subcarrier spacing of 30 kHz, and a maximum transmit power of 51 dBm.

Simulations were conducted using 8x8 and 8x4 antenna arrays to assess the effect of beam broadening in azimuth. All UEs within a cell were equipped with a single omnidirectional antenna and were randomly distributed, with 20% located outdoors and 80% indoors within buildings. The maximum building heights were uniformly distributed between 4 and 8 floors. A full buffer traffic model was employed, with a single UE served in a static position for 6 minutes before being randomly relocated. A GoB beamforming scheme was implemented, utilizing 25 beams in the elevation direction and 45 beams in the horizontal direction. These beams were uniformly distributed within a 120-degree azimuth opening angle.

To investigate the impact of beam pointing error, simulations were performed with an increased number of horizontal beams. This was achieved by adding more beams to cover the entire sector, given the narrower beamwidth of individual beams. However, increasing the number of

horizontal beams beyond 45 did not result in any significant difference, indicating that the primary influence on the results was the angular spread.

Figure 8-12 illustrates the effect of angular spread on different horizontal beamwidths. It depicts the difference in signal-to-noise ratio (SNR) in the downlink connection between simulations using 8x8 and 8x4 arrays at identical UE positions. The plot reveals that in approximately 80% of UE positions, the SNR difference, and consequently the effective gain difference, is less than 0.5 dB. Most of these positions are indoors, as 80% of UEs are located there, and for such O2I propagation conditions, the angular spread is relatively large, as discussed in previous subsection.

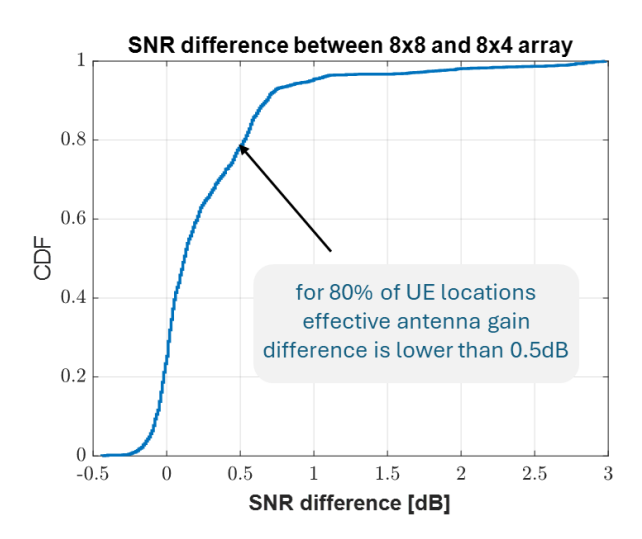


Figure 8-12 Simulation results - the difference between SNR with 8x8 and 8x4 array.

The same plot shows that for less than 20% of UE positions, the 8x4 antenna array exhibits slightly higher SNR (up to 0.4 dB). This could be attributed to beam pointing accuracy, which remained consistent even with a larger number of beams.

Simulation results confirm the effectiveness of the beam broadening method in various typical deployment scenarios. In the presented example, the EIRP in close proximity to the BS could be reduced by 3 dB, while maintaining the received power level at most UE locations.

#### 8.3.3.3 Laboratory Measurements

The principles of the beam broadening method was further confirmed by laboratory measurements. These measurements were conducted using a small cell BS operating at 28 GHz and equipped with a 16x16 antenna array. Different antenna array configurations were tested by disabling antenna elements in the horizontal dimension, effectively emulating the beam broadening effect. A horn antenna with a nominal gain of 10 dBi was employed at the receiver.

Measurements were conducted in both LOS and NLOS environments, meticulously constructed in a laboratory setting. To introduce multipath propagation through reflections, plates were strategically positioned, as illustrated in Figure 8-13. The estimated angular spreads in these environments, as reported in [28][53], were as follows:

- LOS
  - $\circ$  ASD = 4° and ZSD = 0°
- NLOS
  - $\circ$  ASD = 27° and ZSD = 1°

LOS

## NLOS







Figure 8-13 Photos from laboratory experiments.

Table 8-3 (LOS) and Table 8-4 (NLOS) present the measured nominal antenna gain (obtained in an anechoic chamber) and the effective antenna gain reductions, compared to the 16x16 array, for various antenna array configurations. These configurations feature a reduced number of antenna elements in the horizontal direction, representing different levels of beam broadening.

These tables also include calculated effective antenna gain values, derived from the formulas presented in Section 8.3.1, to assess the accuracy of the analytical estimations.

Table 8-3	Measurement	results for	LOS channel.

Antenna Array [V×H]	Measured Nominal Gain reduction as compared to 16×16 array [dBi] (anechoic chamber)	Measured Effective Gain reduction as compared to 16×16 array [dBi] (LOS channel)	Estimated Effective Gain reduction as compared to 16×16 array [dBi] (LOS channel)
16×4	-6 dB	-4.1 dB	-3.9 dB
16×2	-9 dB	-6.1 dB	-6.7 dB
16×1	-12 dB	-10.3 dB	-9.7 dB

Table 8-4 Measurement results for NLOS channel.

Antenna Array [V×H]	Measured Nominal Gain reduction as compared to 16×16 array [dBi] (anechoic chamber)	Measured Effective Gain reduction as compared to 16×16 array [dBi] (NLOS channel)	Estimated Effective Gain reduction as compared to 16×16 array [dBi] (NLOS channel)
16×4	-6 dB	0 dB	-0.33 dB
16×2	-9 dB	-2.2 dB	-1.13 dB
16×1	-12 dB	-3.3 dB	-2.93 dB

The results demonstrate that reducing the number of antenna elements in the horizontal dimension, thereby broadening the beam, leads to a smaller reduction in effective gain compared to the nominal gain, especially in NLOS channel which is characterized by large ASD. For instance, reducing the number of antenna elements in the horizontal dimension from 16 to 1 results in a 12 dB reduction in EIRP close to the BS, but the effective gain of the antenna in the real NLOS channel with a large angular spread is only reduced by 3.3 dB.

The values estimated using analytical formulas show an accuracy within the range of 0.3 dB to 1.1 dB, which is deemed sufficient for practical implementation.

# 8.4 The selective EIRP control in spatial segments for advanced beamforming

#### 8.4.1 Introduction

The mMIMO systems utilize various beamforming algorithms, which directly influence electromagnetic field (EMF) exposure (see Chapter 5):

#### Codebook-based Beamforming (GoB)

This approach selects the optimal beam from a predefined set based on UE feedback. The beam is directed in a single spatial direction. EIRP control within segments can be achieved by reducing power or broadening the beam (Section 8.3.3) in the controlled segment.

#### • Reciprocity-based Beamforming:

This technique leverages the DL channel response derived from UL reference signal measurements. The BS estimates the channel characteristics based on the UL Sounding Reference Signal (UL SRS) and generates optimal beam weights. This approach exploits multipath propagation, resulting in multiple spatial lobes, unlike

the single main lobe of codebook-based beamforming. This irregular antenna pattern also applies to zero-forcing algorithms for interference reduction.

While codebook-based beamforming allows for targeted EIRP control within specific segments, reciprocity-based beamforming presents a challenge. Due to the spread of spatial lobes, reducing power in a controlled segment also affects lobes in uncontrolled segments. This can lead to unnecessary power reduction in areas where EIRP control is not required, potentially impacting cell capacity.

Figure 8-14 and Figure 8-15 illustrates this issue for GoB and reciprocity-based BF respectively.

When codebook-based beamforming is employed, and a specific beam is directed within a defined segment, EIRP control can be triggered to reduce EMF exposure to the required level.

Figure 8-14 illustrates this concept with an example of EIRP control for three segments using codebook-based beamforming. The Figure presents a 2D heat map depicting two different beams directed towards different UEs. The three segments designated for EIRP control are also identified.

Let's assume that Segment 3 requires EIRP control because the EIRP budget is approaching the actual EIRP threshold. In the upper picture, when a particular beam is positioned within Segment 3, the radiated power is high, and EIRP control is activated accordingly. However, when the beam shifts its position to serve other UE, as shown in the bottom picture, EIRP control is not necessary because the radiated power within Segment 3 is significantly lower.

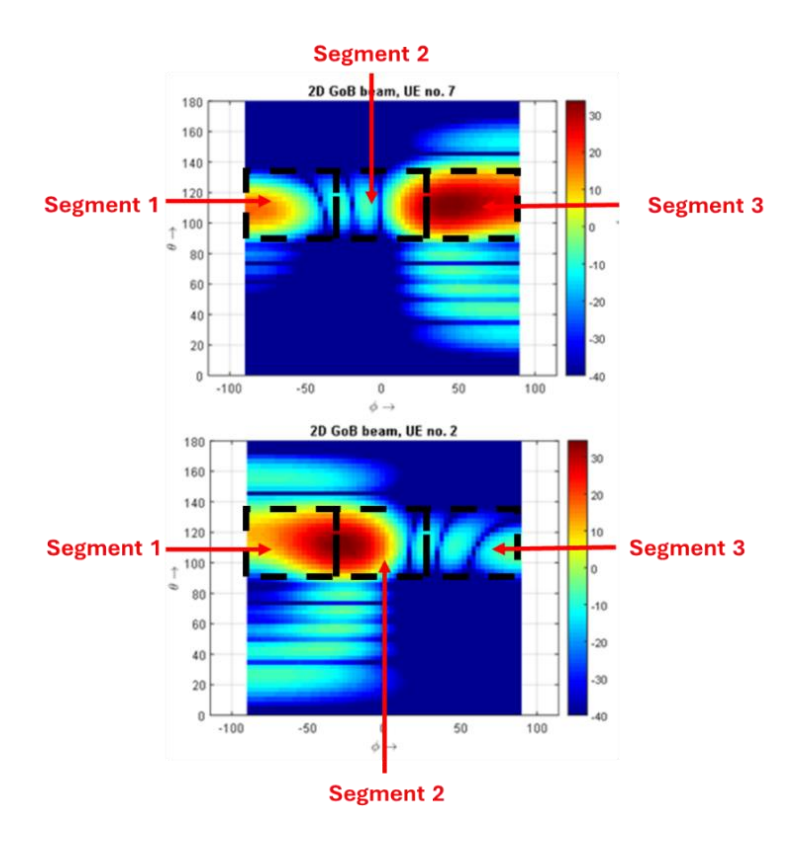


Figure 8-14 Example of GoB with EIRP control in segments.

Figure 8-15 demonstrates the issue with EIRP control in reciprocity-based beamforming. In the case of reciprocity-based beamforming, even with a single UE being served, multiple strong spatial lobes can exist in different segments. While the UE locations differ between the upper and lower pictures, both scenarios exhibit a strong spatial lobe within Segment 3, necessitating EIRP control. However, this control also affects other spatial lobes in segments that do not require control, leading to unnecessary power reduction.

This unintended reduction of EIRP in uncontrolled segments, where EIRP control is not required, negatively impacts cell capacity. The reason is that the power reduction in these segments diminishes the signal strength in areas where it could be maintained, potentially affecting the overall performance and capacity of the cell.

To address this challenge, a novel algorithm for EIRP control in reciprocity-based beamforming has been developed. This algorithm selectively reduces power in controlled segments while increasing power in uncontrolled segments, minimizing the overall beamforming gain loss.

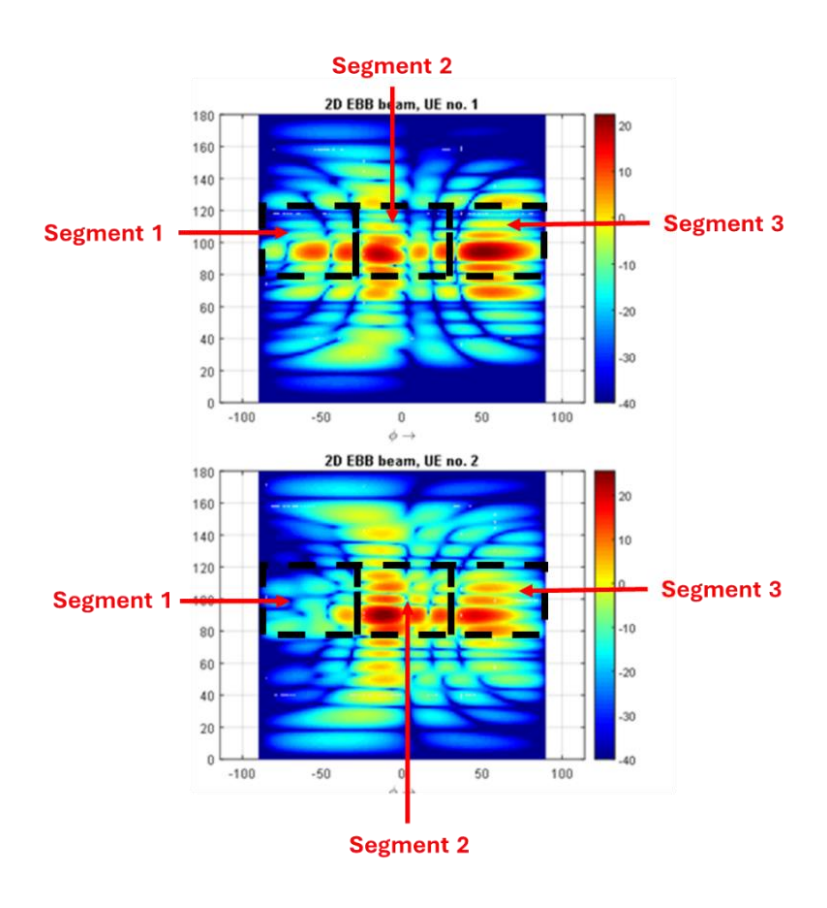


Figure 8-15 Example of reciprocity-based BF with EIRP control in segments.

# 8.4.2 The method of selective actual EIRP control for advanced beamforming schemes

This Section presents two algorithms for calculating optimal precoding weights to control the EIRP in segments. The algorithms aim to minimize total beamforming loss by reducing spatial lobe gain in controlled segments and increasing gain outside these segments. Two versions of algorithm was developed and both are based on the same principle while the second version of algorithm is more suitable for implementation in real BS.

#### Algorithm 1

The main principle of **Algorithm 1** is as follows:

- 1. **Identify** all spatial lobes in the nominal antenna pattern that are outside of the controlled segments.
- 2. **Place** virtual multipaths at the center of these spatial lobes.
- 3. **Calculate** and **add** the array response for these virtual multipaths to the nominal array response.
- 4. **Apply** the Maximum Ratio Transmission (MRT) method to the resulting array response to calculate the precoding weights.

#### Algorithm 2

**Algorithm 2** follows a similar principle, but focuses on the controlled segments:

- 1. **Identify** all spatial lobes in the nominal antenna pattern that fall within the controlled segments.
- 2. **Place** virtual multipaths at the center of these spatial lobes.
- 3. **Calculate** and **subtract** the array response for these virtual multipaths from the nominal array response.
- 4. **Apply** the MRT method to the resulting array response to calculate the precoding weights.

#### **Detailed Implementation of Algorithm 1**

The following steps illustrate the implementation of **Algorithm 1** for a Uniform Linear Array (ULA) and a multipath propagation channel model:

- 1) Channel Response Acquisition: The channel response *h* from the antenna array is obtained during the channel state information process within the base station by measuring the Uplink Sounding Reference Signal (SRS). Beamforming algorithms, such as Eigen Beamforming (EBF) or Zero Forcing (EZF), are then applied to calculate precoding weights *p* based on the channel response and specific optimization criteria.
- 1. **Spatial Lobe Identification:** The nominal antenna pattern is analyzed for the given channel and corresponding precoding weights to identify the spatial lobes outside controlled segments.

- 2) Virtual Path Placement: Virtual paths V are placed at the center of spatial lobes located outside the EIRP controlled segments  $(\varphi_v, \theta_v)$ .
- 3) Virtual Channel Response Calculation: The virtual channel response  $h_{\nu}$ , for all virtual paths V outside the controlled segments is calculated using the following formula:

$$h_V = \sum_{v=1}^V e^{-j\psi_v} a_M(\varphi_v, \theta_v)$$
 Equation 8-10

where:

 $\psi_v$ 

- the *vth* virtual path phase shift, equal to the phase shift in the nominal channel response

$$a_M(\varphi_v,\theta_v)$$

- array response for the ULA with M antenna elements for azimuth  $\varphi_v$  and elevation  $\theta_v$  angles of the *vth* virtual path

The array response is calculated using the following formula:

$$a_{M}(\varphi_{v}, \theta_{v}) = \begin{bmatrix} 1 \\ e^{-j2\pi \frac{\Delta \sin(\varphi_{v})\cos(\theta_{v})}{\lambda}} \\ \vdots \\ e^{-j2\pi \frac{(M-1)\Delta \sin(\varphi_{v})\cos(\theta_{v})}{\lambda}} \end{bmatrix}$$
 Equation 8-11

 $\Delta$  – antenna element spacing, typical  $\frac{\lambda}{2}$ 

4) **Total Channel Response Calculation:** The virtual channel response  $h_v$  is multiplied by the factor A and added to nominal channel response h to obtain total channel response  $h_{total}$ 

$$h_{total} = Ah_v + h$$
 Equation 8-12

5) Precoding Weight Calculation: The precoding weights  $p_{total}$  are calculated using MRT method for the resulting total channel response  $h_{total}$ 

$$p_{total} = \frac{h_{total}^*}{\|h_{total}\|}$$
 Equation 8-13

The antenna array pattern with precoding weights  $p_{total}$  reduces beamforming gain in the controlled segments and increases gain in other spatial directions.

#### **Detailed Implementation of Algorithm 2**

The implementation of Algorithm 2 follows a similar process, with the key difference being the calculation and subtraction of the virtual channel response of the virtual paths which falls into controlled segments from the nominal channel response:

- 1) Channel Response Acquisition: The channel response *h* from the antenna array is obtained during the channel state information process within the base station by measuring the Uplink Sounding Reference Signal (SRS). Beamforming algorithms, such as Eigen Beamforming (EBF) or Zero Forcing (EZF), are then applied to calculate precoding weights *p* based on the channel response and specific optimization criteria.
- 2) **Spatial Lobe Identification:** The nominal antenna pattern is analyzed for the given channel and corresponding precoding weights to identify the spatial lobes which fall into controlled segments.
- 3) Virtual Path Placement: Virtual paths C are placed at the center of spatial lobes located within the segments requiring EIRP control ( $\varphi_c$ ,  $\theta_c$ ).
- 4) Virtual Channel Response Calculation: The virtual channel response  $h_c$ , for all virtual paths C within the controlled segments is calculated using the following formula:

$$h_c = \sum_{c=1}^{C} e^{-j\psi_c} a_M(\varphi_c, \theta_c)$$
 Equation 8-14

where:

 $\psi_c$ 

- **vth** virtual path phase shift, equal phase shift in nominal channel response  $a_M(\varphi_c, \theta_c)$ 
  - array response for ULA with M antenna elements for azimuth  $\varphi_c$  and elevation  $\theta_c$  angles of the *cth* virtual path

The array response is calculated using the following formula:

$$a_{M}(\varphi_{c}, \theta_{c}) = \begin{bmatrix} 1 \\ e^{-j2\pi \frac{\Delta \sin(\varphi_{c})\cos(\theta_{c})}{\lambda}} \\ \vdots \\ e^{-j2\pi \frac{(M-1)\Delta \sin(\varphi_{c})\cos(\theta_{c})}{\lambda}} \end{bmatrix}$$
 Equation 8-15

 $\Delta$  – antenna element spacing, typical  $\frac{\lambda}{2}$ 

5) Total Channel Response Calculation: The virtual channel response  $h_c$  is multiplied by a factor B and subtracted from the nominal channel response h to obtain the total channel response  $h_{total}$ 

$$h_{total} = h - Bh_v$$

#### Equation 8-16

6) Precoding Weight Calculation: The precoding weights  $p_{total}$  are calculated using MRT method for the resulting total channel response  $h_{total}$ :

$$p_{total} = \frac{h_{total}^*}{\|h_{total}\|}$$
 Equation 8-17

The antenna array pattern with precoding weights  $p_{total}$  reduces beamforming gain in the controlled segments and increases gain in other spatial directions.

The factors  $A \ge 1$  and  $B \in [0, 1]$  control the level of reduction of gain in the controlled segments.

- A≥1: This factor is used in Algorithm 1 and determines the strength of the virtual paths added to the nominal channel response. A higher value of A leads to a greater reduction in gain within the controlled segments.
- $B \in [0, 1]$ : This factor is used in Algorithm 2 and determines the weight of the virtual paths subtracted from the nominal channel response. A higher value of B leads to a greater reduction in gain within the controlled segments.

By adjusting these factors, the algorithms can be fine-tuned to achieve the desired level of EIRP control in different scenarios.

Both algorithms achieve the same objective of EIRP control, but Algorithm 2 is more suitable for practical implementation due to its focus on identifying spatial lobes within the controlled segments. Algorithm 1 requires identifying lobes outside the controlled segments, which can be significantly more numerous.

The presented algorithms can be adapted to other antenna array types, such as Uniform Rectangular Array (URA), non-uniform arrays, and spherical arrays, by applying the relevant array response formula.

The next Section will present simulation results demonstrating the effectiveness of the proposed methods.

#### 8.4.3 Simulation results

The algorithms for selective EIRP control were verified in a MATLAB environment using various radio channel realizations and resulting antenna patterns.

#### Example 1

This example demonstrates the application of Algorithm 1 for a uniform linear array (ULA) with 8 elements. The nominal antenna pattern exhibits four strong lobes of equal amplitude in different directions. Two segments requiring EIRP control are identified. Virtual paths are placed at the center of the spatial lobes outside the controlled segments, as outlined in Algorithm 1 (Section 8.4.2). EIRP control is then applied to these segments with factors A=1 and A=2.

The resulting antenna patterns (Figure 8-16) show a reduction in gain within the controlled segments (3.1 and 2.7 dB for A=1, and 5.2 and 3.9 dB for A=2), with a greater reduction for larger values of A. Simultaneously, the gain of lobes outside the controlled segments is enhanced (approximately 1.7 to 2.3 dB) to minimize the overall antenna loss.

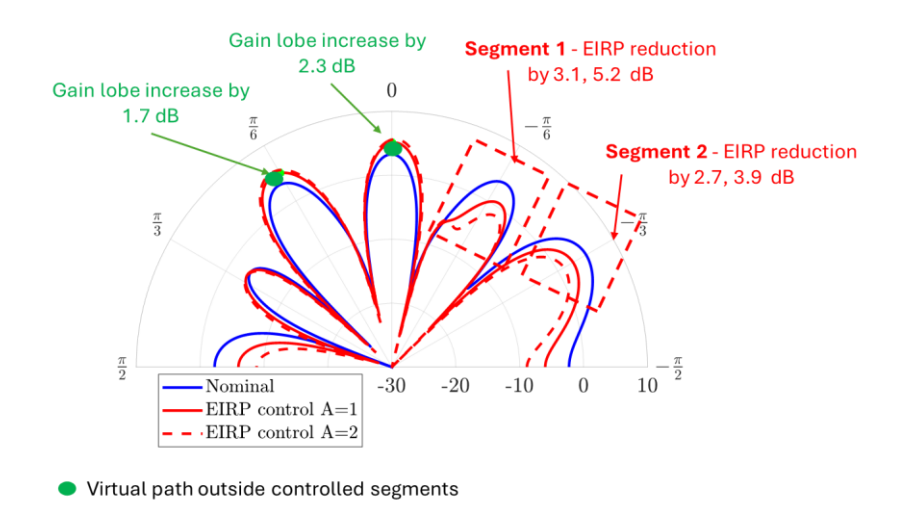


Figure 8-16 Calculated antenna patterns in azimuth for a ULA with 8 elements, demonstrating selective EIRP control using Algorithm 1.

#### Example 2

Algorithm 2 was also verified using the same nominal antenna pattern (Figure 8-17). In this example, a single segment requires EIRP control in the boresight direction of the array. The algorithm was applied with factors B=0.5, 0.7, and 1. Increasing levels of EIRP reduction are observed: 2.3 dB (B=0.5), 7.2 dB (B=0.7), and 16.7 dB (B=1). Applying B=1 effectively performs null forming in this direction, completely canceling the lobe. The lobes outside the controlled segment experience a slight enhancement.

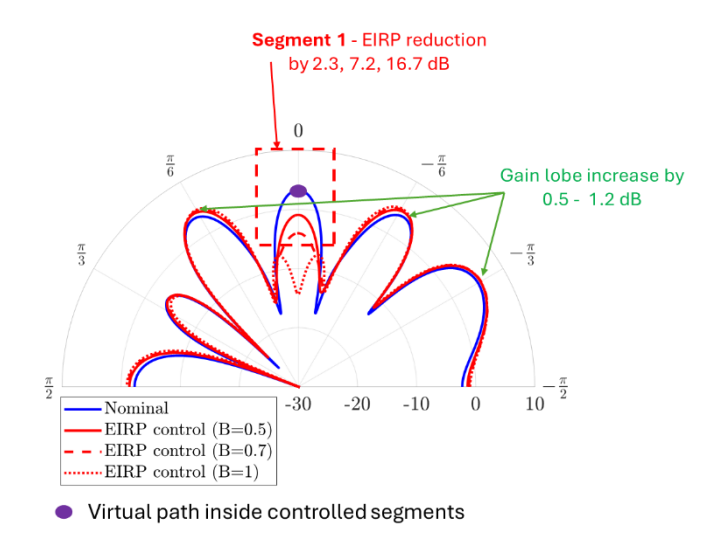


Figure 8-17 Calculated antenna patterns in azimuth for a ULA with 8 elements, demonstrating selective EIRP control using Algorithm 2.

The level of enhancement depends on the number of controlled segments and uncontrolled lobes. In Example 1, with two controlled segments and two uncontrolled lobes, the gain enhancement was more significant. In this example, with only one controlled segment and three uncontrolled lobes, the MRT algorithm needs to distribute less energy to more lobes, resulting in a lower gain enhancement.

#### Example 3

This example utilizes a ULA with 12 elements and tests Algorithm 2. The nominal antenna pattern reveals five lobes with varying amplitudes (Figure 8-18). The controlled segments are located on the strongest lobes, and Algorithm 2 is applied with factors B=0.5 and 0.8. Significant EIRP reduction levels are observed (4.2 and 6.8 dB), particularly for larger values of B. The gain enhancement is also more pronounced for larger B values (3.8 and 4.2 dB).

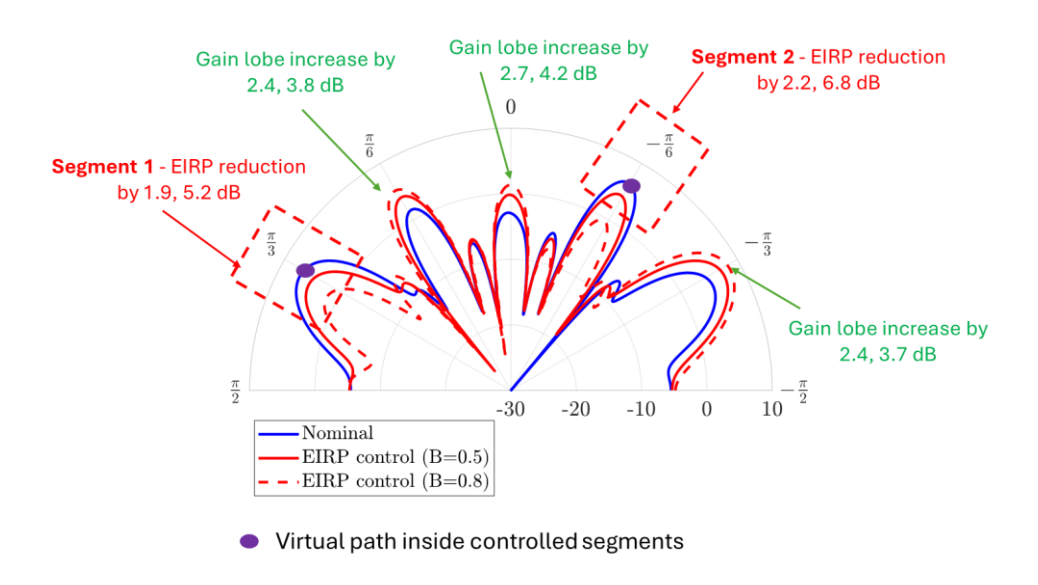


Figure 8-18 Calculated antenna patterns in azimuth for a ULA with 12 elements, demonstrating selective EIRP control using Algorithm 1.

#### Example 4:

This example verifies selective EIRP control using Algorithm 2 for a URA antenna with 12x12 elements. The 3D antenna pattern before and after EIRP control activation is shown in Figure 8-19. The controlled segment is placed in the direction of the antenna boresight, where the strongest lobe is present. Two additional lobes with lower amplitudes are visible at other angles.

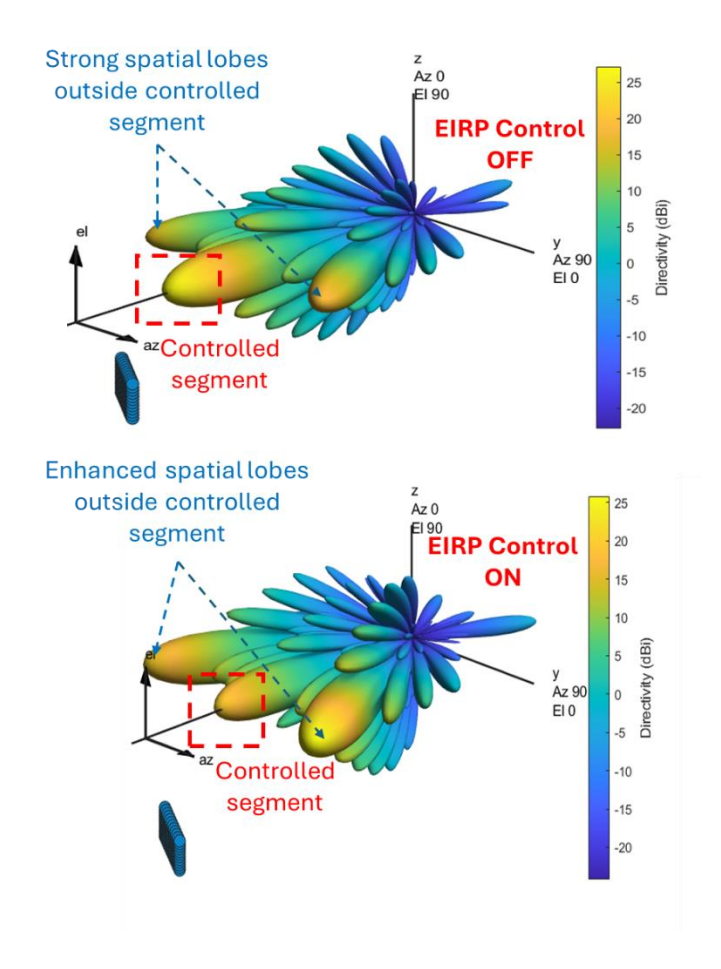


Figure 8-19 Calculated 3D antenna patterns for a ULA with 12x12 elements, demonstrating selective EIRP control using Algorithm 2.

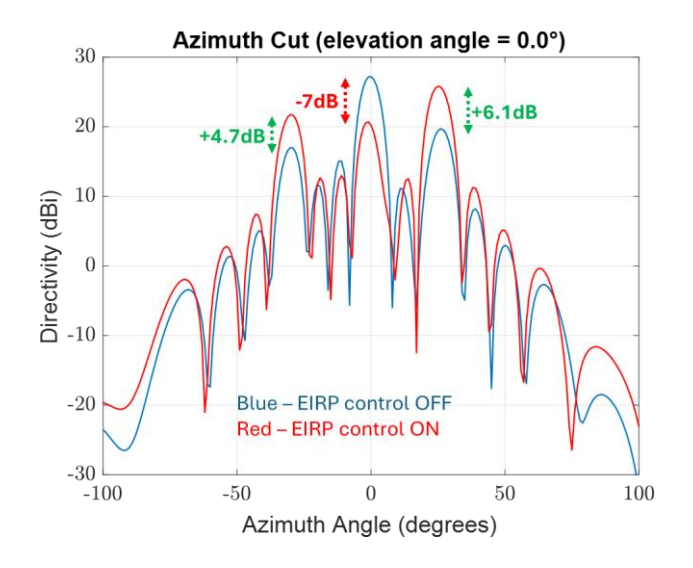


Figure 8-20 Calculated azimuth antenna pattern for a ULA with 12x12 elements, demonstrating selective EIRP control using Algorithm 2.

When EIRP control is activated, the lobe gain in the controlled segment is reduced, and the gain of lobes outside the controlled segment is enhanced. The azimuth cut of the pattern is presented in Figure 8-20, illustrating the magnitude of these changes. The lobe gain in the controlled segment is reduced by -7 dB, while the gain of other lobes is increased by 4.7 dB and 6.1 dB to compensate for the total beamforming loss.

## 8.5 Summary and Conclusions

This Chapter explores the critical role of Effective Isotropic Radiated Power control in massive MIMO systems, particularly in the context of meeting electromagnetic field exposure limits as defined in IEC 62232 [15].

The Chapter emphasizes the importance of real-time EIRP monitoring and control mechanisms to ensure compliance with EMF exposure limits. While EIRP control is crucial for maintaining average EIRP below defined thresholds, it's important to note that a single solution may not be universally applicable due to potential impacts on system performance.

The Chapter discusses the advantages of a segment-based approach to EIRP control compared to a sector-based approach. This segment-based approach allows for more granular control and optimization.

The Chapter analyzes various transmit power-based control techniques, highlighting the suitability of PRB based reduction for users with low SINR and PDSCH based power control for medium to high SINR levels.

The Chapter introduces and analyzes novel methods for actual EIRP control that leverage beamforming algorithms. The EIRP control toolbox relies on various combination of transmit power reduction. The thesis investigates the potential of directive RF emission shaping from of antenna arrays by utilized specialized beamforming algorithms.

Beam broadening technique for codebook-based beamforming utilizes the angular spread of the radio channel to broaden and optimize the beamwidth of transmitted beams, effectively reducing EIRP without significantly impacting received power for users within the cell. This approach complements traditional EIRP control techniques based on power or resource block reduction.

Selective EIRP control solution for advanced beamforming schemes addresses the challenges of EIRP management in reciprocity-based beamforming by selectively controlling gain in specific segments, optimizing performance and minimizing unnecessary gain reduction. This approach maximizes spatial lobe gains outside the controlled segments, minimizing overall beamforming loss.

Both presented solutions are designed for practical implementation in mMIMO base stations. The choice of beamforming algorithm significantly impacts EMF exposure and EIRP control in mMIMO systems. While codebook-based beamforming offers targeted control,

reciprocity-based beamforming requires a more sophisticated approach to ensure efficient EIRP management without compromising cell capacity.

This Chapter provides a comprehensive overview of EIRP control strategies in mMIMO systems, emphasizing the importance of a multi-faceted approach that considers both traditional and novel techniques. The document highlights the benefits of segment-based control, beamforming algorithms, and selective power control in specific segments, ultimately contributing to the development of efficient and compliant mMIMO systems for future 6G deployments.

# 9. Summary

#### 9.1 Conclusions on research results

My doctoral dissertation investigates electromagnetic field exposure from multiantenna systems, specifically focusing on the EMF impact of Massive MIMO with beamforming. Advanced system-level simulations were conducted using various use cases, parameter sets, parameter values, and scenarios to analyze the effect of beamforming on actual average EMF exposure.

The research evaluated the power reduction factors required for operation within the actual maximum approach, as recommended by IEC62232 [15]. It also explored the actual EIRP control topic and proposed two novel beamforming algorithms designed for practical implementation in 5G and 6G base stations.

All the research Questions presented in Chapter 1 (Section 1.6) have been addressed by the research conducted in this dissertation.

#### Q1. Actual EMF Distribution

The RF EMF distribution in the vicinity of a base station with multiantenna systems is characterized by the statistical distribution of EIRP generated by the mMIMO base station. My doctoral thesis involved a system level simulation with channel modeling studies of multiantenna systems. Employing a realistic model incorporating radio wave propagation, base station and terminal distribution, beamforming algorithms, and telecommunications traffic, a statistical approach revealed that actual EMF exposure from these systems is significantly lower than anticipated. This exposure is highly dependent on system parameters and scenario. The determined power reduction factor enables a substantial reduction in the compliance zones surrounding the antennas.

The initial phase of the research involved analyzing Massive MIMO systems employing 'Grid of Beam' algorithms, as detailed in publications [25]. This analysis demonstrated that a statistical approach, incorporating realistic modeling of radio wave propagation, base station deployment, terminal distribution, beamforming algorithms, and traffic exposure, indicates significantly lower actual exposure to EMF from these systems. Notably, the exposure level is highly dependent on system parameters and scenario-specific conditions.

The actual EMF exposure and the power reduction factor values are influenced by several critical factors:

- Size of the antenna system
- Number of antenna beams and active MIMO streams
- Spatial distribution of terminals
- Number of supported terminals and the duration of their serving time

Furthermore, an increase in telecommunications traffic leads to greater beam switching dynamics, resulting in reduced EMF exposure.

#### **Q2.** Statistical Channel Modeling

Statistical channel modeling using advanced system-level simulations is crucial for evaluating EMF exposure from mMIMO base stations due to the complex nature of wireless communication systems. Digital beamforming schemes are highly dependent on the distribution of user equipment within the sector and radio propagation characteristics. Both factors can be effectively modeled using statistical models.

To accurately model the complex operation of a 5G mobile network, I have enhanced the system level simulator for evaluating actual EMF exposure. These enhancements aim to closely replicate the realistic functionality of real massive MIMO base stations. The inherent complexity of the system, further amplified by the use of multiantenna systems with spatially shaped power transmission, necessitates advanced simulation techniques. I utilized the Monte Carlo method, a powerful tool for modeling complex processes, to conduct simulations of a cellular system with multiple base stations. These simulations incorporated models of mMIMO systems featuring dynamic radiation control, varying numbers of users, and diverse user distributions.

This research investigated the influence of moving terminals on the actual power electromagnetic field intensities near the antenna and the  $F_{PR}$  coefficient. Existing models, including those presented in [6][20][26][21][17] have primarily focused on stationary terminals. This research proposed a statistical model of terminal movement that incorporates the correlations of statistical radio channel model parameters for consecutive terminal positions. The findings demonstrate that the actual EMF exposure near the base station and the associated  $F_{PR}$  coefficient decrease when terminals are in motion, a common occurrence in real cellular systems. This reduction is attributed to the increased activity of antenna beam switching. The  $F_{PR}$  coefficient exhibited a decrease ranging from -1.5dB to -3.5dB. These results were published in [36].

#### Q3. Beamforming Impact

Beamforming algorithms significantly impact the level and spatial distribution of EMF exposure. mMIMO base stations implement beamforming algorithms to generate multiple beams that adapt to user positions, resulting in a spatial distribution of EMF exposure. I modelled advanced beamforming algorithms in the simulator, such as eigenbeamforming which adapts to changes in the propagation channel, and eigenbeam zero-forcing which additionally minimizes interference by steering the null of the antenna pattern towards the terminals. In these studies, a statistical radio channel model was used for the first time, in comparison to [21], where the ray-tracing method and one simple scenario were used. My results were published in [37] and show that the use of advanced beamforming methods, in addition to significantly improving system performance in the form of increased capacity, significantly reduces the EMF exposure in the base station's surroundings. It should be noted that advanced beamforming methods such as EBF and EZF will be introduced as part of the development of Massive MIMO

systems and will be mainly used in new 6G network solutions based on artificial intelligence algorithms. The results of the work show once again how critical it is to use complex propagation models to evaluate multiantenna systems.

#### **Q4.** Power Reduction Factor

Effective estimation of the power reduction factor requires modeling cellular network operations using system-level simulations with deployment types and parameters similar to real systems. The simulations should consider the propagation scenario, antenna array setup, beamforming scheme, number of serving UEs, and traffic type to estimate  $F_{PR}$  values. While accurate modeling is challenging, the research demonstrates that estimated  $F_{PR}$  values are often overestimated, providing an additional margin for base station deployment.

To validate computer simulations, I conducted EMF measurements at the Massive MIMO base station within a specialized anechoic chamber. This chamber facilitates the emulation of terminal traffic, enabling the use of varying numbers of terminals and diverse telecommunications traffic types. The measurement results align with the simulation outcomes.

#### Q5. Actual RF Emissions Control

The IEC62232 [15] standard for Massive MIMO introduces the EMF exposure assessment method, which relies heavily on EIRP monitoring and control functions. Due to the statistical nature of this method, based on average EMF values, there is a risk of exceeding the EIRP limit, even for brief periods. EIRP control mitigates this risk by reducing the EIRP to ensure the average value remains within the  $F_{PR}$  parameter limits. Controlling EIRP is a crucial aspect of the actual maximum approach method. The research indicates that the probability of EIRP control is relatively low. However, this reduction can negatively impact the power received by user terminals, potentially affecting their throughput. Optimizing EIRP control is essential to minimize its impact on performance.

To address this challenge, optimization methods are crucial. Existing approaches primarily focus on controlled power reduction and its optimization. This dissertation analyzes EIRP control through power or bandwidth reduction and identifies their optimal SINR regimes.

My research explored an alternative approach by focusing on antenna gain control through optimized beamforming algorithms. Two algorithms were developed: one for 'Grid of Beam' switching methods and another for advanced beamforming methods and EIRP control in sectors. These algorithms aim to minimize system capacity loss when EIRP reduction is necessary. The first technique leverages the angular spread effect on narrow beamwidths and involves designing and analyzing an optimal beam broadening algorithm. The second technique targets advanced beamforming schemes for EIRP control in segments. The designed algorithm selectively reduces EIRP in targeted segments and enhances gain outside those segments to compensate for the total beamforming loss. The results have been submitted to publication [90]. Two patents have been filed.

All the Hypotheses introduced in Chapter 1 (Section 1.6) were validated by the research conducted in that Ph.D. Dissertation.

#### H1. Antenna Array Size

Numerous analyses have shown that actual EMF exposure around the base station decreases as antenna size decreases. This is attributed to the fact that narrower beamwidths reduce the spatial distribution of energy. Additionally, larger antenna arrays provide better resolution, which, in the case of advanced digital beamforming, enables better adaptability to instantaneous radio channel and interference situations. This results in a more spread distribution of energy in space.

This research investigates the actual EMF exposure of planned Extreme Massive MIMO systems, which will utilize significantly larger antenna element counts. These systems are envisioned as part of the next generation 6G networks, where new higher frequency bands in the 7-15 GHz range will be introduced for mobile telecommunications. The study focuses on the impact of large antenna arrays on the power reduction factor. The findings indicate that employing the actual maximum approach for evaluating EMF exposure allows for the preservation of existing compliance areas. This is due to the decrease in the  $F_{PR}$  coefficient as the antenna array size increases, resulting in a consistent compliance distance from the antenna.

The results have been published in [36] and referenced in IEC TR 62669:2025 [15].

#### **H2.** Advanced Beamforming

The research proves that advanced beamforming algorithms, such as eigenbeamforming or eigenbeamforming zero-forcing, through adaptation to radio channel characteristics, result in irregular effective antenna patterns. This irregular pattern, which spreads more energy in space, leads to lower EMF exposure compared to classical beamforming schemes like grids of beams. The research indicates that the power reduction factor decreases from -5 dB to -12 dB, resulting in a significant reduction of the compliance zones surrounding the base station.

The results have been published in [37] and referenced in IEC TR 62669:2025 [15].

#### **H3.** Statistical Modeling of Power Reduction Factor

The dissertation demonstrates that the power reduction factor can be modeled using advanced system simulations that utilize Monte Carlo techniques alongside statistical channel models and user distributions. This statistical modeling of EMF exposure and, consequently,  $F_{PR}$ , provides results that closely align with measurements.

The conclusions drawn in this thesis are applicable to other frequency bands, bandwidth sizes, and subcarrier spacings, as  $F_{PR}$  values primarily depend on antenna size, beamforming scheme, deployment type, UE numbers and distribution, and traffic model.

#### 9.2 Achievements

My Ph.D. Dissertation makes several significant contributions to the field of radio frequency electromagnetic field exposure analysis for Massive MIMO base stations. These contributions address key gaps in the current research landscape and advance the understanding of EMF exposure in future 6G networks.

#### **Original Achievements:**

#### • Introduction of a Moving UE Model:

This work introduces a dynamic UE moving model, replacing the static UE models commonly used in research. This allows for a more realistic assessment of actual RF exposure from Massive MIMO base stations serving mobile terminals. The study provides statistical analysis of the resulting exposure levels.

#### • Comprehensive Beamforming Analysis:

This research provides a comprehensive analysis of the impact of three main beamforming schemes on actual EMF exposure. It utilizes system-level simulations with statistical methods, offering a more realistic and detailed assessment compared to previous studies. Previous research in this area has primarily focused on comparing beamforming algorithms in simplified deployment scenarios using ray-tracing models. This work expands upon this limited research by considering a wider range of beamforming schemes and employing a more sophisticated simulation approach.

#### • Analysis of Extreme Massive MIMO Systems:

The work investigates the RF exposure characteristics of extreme Massive MIMO systems planned for future 6G networks operating in the 7-15 GHz frequency bands. This analysis is novel and fills a gap in the current literature.

- **Optimal EIRP Control Algorithm:** The research proposes a novel algorithm for optimal EIRP control through beam broadening, leveraging channel angular spread. This approach differs from existing research, which primarily focuses on transmit power control.
- Advanced Beamforming Algorithm for Selective EIRP Control: The work introduces a novel algorithm for advanced beamforming with selective EIRP control in segments. This algorithm optimizes EIRP reduction by targeting only the segments requiring control, unlike existing techniques that reduce EIRP across all segments. This approach compensates for the loss in total beamforming gain by increasing gain in other directions outside controlled segments.

#### **Publications**

The following publications represent the author's key contributions:

1. <u>Marcin Rybakowski</u>, Kamil Bechta, "Analiza Symulacyjna Rzeczywistej Ekspozyji na Promieniowanie Electromagnetyczne od Systemów Wieloantenowych 5G", Krajowa Konferencja Radiokomunikacji, Radiofonii i Telewizji, Warszawa, 08.09.2022,

published in Przegląd Telekomunikacyjny - Wiadomości Telekomunikacyjne, numer 4, 2022

- 2. <u>Marcin Rybakowski</u>, Kamil Bechta, Christophe Grangeat, Paweł Kabacik, "*Impact of Beamforming Algorithms on the Actual RF EMF Exposure From Massive MIMO Base Stations*", IEEE Access, Volume 11, December 2023
- 3. <u>Marcin Rybakowski</u>, Kamil Bechta, Christophe Grangeat, Paweł Kabacik, "Evaluation of the Actual EMF Exposure from Extreme Massive MIMO Base Stations around 10 GHz using Channel Modelling", 25th International Microwave and Radar Conference, 1-4 July 2024, Wroclaw
- 4. <u>Marcin Rybakowski</u>, Kamil Bechta, Christophe Grangeat, Paweł Kabacik, "Statistical Analysis of the Actual RF Exposure from Massive MIMO Base Stations Serving Moving User Equipment", IEEE Access, Volume 12, 2024
- 5. <u>Marcin Rybakowski</u>, Kamil Bechta, Christophe Grangeat, Azra Zejnilagic, Paweł Kabacik, "Optimization of Actual EIRP Control for Massive MIMO Base Stations Leveraging Beam Broadening and Angular Spread", submitted to EuCNC (European Conference on Networks and Communications) and 6G Summit, planned for 3-6 June 2025, Poznan

#### **Additional Relevant Publications:**

The author has also contributed to the following publications, which are relevant to the thesis topics:

- 1. Kamil Bechta, Christophe Grangeat, Jinfeng Du, <u>Marcin Rybakowski</u>, "Analysis of 5G Base Station RF EMF Exposure Evaluation Methods in Scattering Environments", IEEE Access, Volume 10, January 2022
- 2. P. Bieńkowski, B. Zubrzak, P. Sobkiewicz, K. Bechta and M. Rybakowski, "Simplified Methodology of Electromagnetic Field Measurements in the Vicinity of 5G Massive MIMO Base Station for Environmental Exposure Assessment," IEEE Access, Volume 12, 2024
- 3. K. Bechta, J. Du and M. Rybakowski, "Rework the Radio Link Budget for 5G and Beyond", IEEE Access, Volume 8, 2020

#### **Patent Applications:**

The author has contributed to the development of novel EIRP control algorithms, which are currently being pursued as patent applications:

- 1. "EIRP CONTROL BY BEAM BROADENING FOR RADIO CHANNEL WITH ANGULAR SPREAD"
  - o Main inventor: Marcin Rybakowski

- o Co-inventors: Kamil Bechta, Christophe Grangeat, Azra Zejnilagic
- o Status: Accepted by Patent Department in Nokia and filed for patenting.
- o Finnish Patent Application Number: 20246502 (filling date: 19.12.2024)

### 2. "SELECTIVE EIRP CONTROL FOR SPATIAL SEGMENTS"

- o Main inventor: Marcin Rybakowski
- o Co-inventors: Kamil Bechta, Christophe Grangeat, Azra Zejnilagic
- o Status: Currently under analysis by Patent Department in Nokia.

#### **Potential Impact:**

These innovative actual EIRP control algorithms hold significant potential for future Massive MIMO base stations. Nokia is planning to conduct a feasibility study to evaluate their practical implementation and assess their suitability for integration into future base station designs.

#### **Contribution to standards:**

This research has directly contributed to the development of international standards for radio frequency exposure evaluation. This research has made important contributions to the International Electrotechnical Commission (IEC) Technical Committee 106 (TC106):

#### • IEC TC106 MT3 Contribution:

The author contributed to the IEC TC106 MT3 committee, providing technical input based on research conducted for the thesis. These contributions were incorporated into relevant IEC documents.

#### • Reference in IEC TR 62669:

The author's publications [37][45][36] are referenced in IEC TR 62669, "Case studies supporting IEC 62232 - Determination of RF field strength, power density and SAR in the vicinity of radiocommunication base stations for the purpose of evaluating human exposure" [14]. This technical report provides practical guidelines for implementing the actual maximum approach in Massive MIMO base stations, ensuring compliance with RF exposure standards.

#### • Alignment with IEC 62232:

The research aligns with the principles outlined in IEC 62232:2025 [15], which allows for the use of  $F_{PR}$  values obtained through computational modeling in RF EMF exposure evaluation. These values can be configured in the base station to ensure that the EIRP threshold is not exceeded during operation.

This research demonstrates a strong commitment to advancing the field of RF exposure assessment and contributing to the development of robust and practical standards for future wireless technologies.

#### **Industry Workshops:**

The author participated in industry workshops with electromagnetic field exposure sessions. These sessions featured presentations and discussions by industry representatives on current issues related to EMF exposure:

- 1. Paweł Bieńkowski, <u>Marcin Rybakowski</u>, "*Nowoczesne systemy radiokomunikacyjne 5G z antenami wielowiązkowymi*", XIII Krajowe Warsztaty Kompatybilności Elektromagnetycznej EMC 2022, Politechnika Wrocławska, Wrocław, 28.06.2022
- 2. <u>Marcin Rybakowski</u> "Walidacja funkcji monitorowania i kontroli EIRP dla systemów Massive MIMO zgodnie z IEC62232", XIV Krajowe Warsztaty Kompatybilności Elektromagnetycznej EMC 2024, Politechnika Wrocławska, Wrocław 27.06.2024

# 9.3 Outlook for future research on electromagnetic field exposure in multiantenna systems

The intricate nature of complex beamforming and spatial multiplexing, influenced by radio propagation conditions, user distributions, and scheduling algorithms, necessitates further research in this area.

Multiantenna systems, introduced in the 5G standard, will become a core technology for future wireless communication standards, such as 6G. The following research areas within Massive MIMO, which could significantly impact EMF exposure evaluation and control methods, warrant further investigation:

#### 1) Extreme and Gigantic Massive MIMO planned in 6G

The number of antenna elements embedded in base stations is expected to increase significantly due to the potential for improved system performance through high-resolution spatial multiplexing. The use of higher frequency bands in the mmWave and sub-THz ranges necessitates large antenna arrays, making extreme or gigantic Massive MIMO a prominent research area [44][57][43][42].

The utilization of very large arrays with advanced beamforming techniques, potentially incorporating machine learning algorithms, could be studied for accurate prediction of power reduction factors and optimal EIRP control in relation to EMF exposure. While initial research in this area has been conducted by author in this thesis, further exploration is needed [58].

#### 2) Integrated Communication and Sensing (ISAC)

The integration of communication and sensing is a new paradigm planned for 6G systems. The multiantenna systems and large bandwidths employed in wireless communications provide significant potential for effective sensing capabilities in future communication systems [59].

While ISAC holds promise for various applications and use cases, its impact on EMF exposure remains unexplored. Sensing requires high power and focused energy through

beamforming for accurate localization, necessitating research into the impact of sensing on actual EMF exposure levels.

#### 3) Reconfigurable Intelligent Surfaces (RIS):

RIS is a programmable surface structure that can control the reflection of electromagnetic waves by adjusting the electric and magnetic properties of the surface. These surfaces can be strategically positioned in the radio channel between a transmitter and receiver to influence signal reflection during propagation. RIS can be used to steer signals towards the receiver, resulting in improved reception or link quality [60].

Initial research has explored the potential of RIS technology for mitigating EMF exposure around base stations [61][62][63]. However, further research in this area is highly recommended.

#### 4) Near field beamforming

The increasing size of antenna arrays and the use of higher frequency bands lead to an expanding near-field area around base station deployments. The operation of Massive MIMO base stations in the near-field allows for the implementation of near-field beamforming techniques, which provide beam-spotting capabilities. This results in beams with finite depth compared to the infinite focus of far-field beamforming [64].

This type of precoding in the near field offers a novel approach to managing EMF exposure around base stations. Beam spots have the potential to utilize high power and high gain from larger antenna arrays while mitigating exposure in areas close to the base station. This potential requires detailed exploration and study by the EMF exposure community.

#### 5) New frequency bands

The introduction of new frequency bands in mobile communication is ongoing. Research for 6G is even considering sub-THz bands around 140 GHz [39].

These extremely high frequencies necessitate the use of very large arrays to compensate for propagation loss. The application of these new bands and antennas requires attention from the EMF exposure perspective, particularly as very large antennas are also required on the terminal side.

#### 6) Multi system and multi technology

The increasing number of wireless communication systems, standards, and technologies necessitates the study of total EMF exposure from all these systems. Evaluation methods need to be developed, especially for systems deployed in the same or close locations and by different vendors.

## 10. References

- [1] X. Lin, "3GPP Evolution from 5G to 6G: A 10-Year Retrospective", https://arxiv.org/abs/2412.21077, 2024
- [2] T. Marzetta, E. G. Larsson, H. Yang, and H. Q. Ngo, "Fundamentals of Massive MIMO", Cambridge University Press, 2016
- [3] E. Björnson, Ö. Tuğfe Demir, "Introduction to Multiple Antenna Communications and Reconfigurable Surfaces" Boston-Delft, 2024
- [4] E. Björnson, E. G. Larsson and T. L. Marzetta, "Massive MIMO: ten myths and one critical question", IEEE Communications Magazine, vol. 54, no. 2, pp. 114-123, February 2016
- [5] E. Björnson, L. Sanguinetti, H. Wymeersch, J. Hoydis, T. L. Marzetta, "Massive MIMO is a reality—What is next?: Five promising research directions for antenna arrays", Digital Signal Processing, Volume 94, November 2019
- [6] P. Baracca, A. Weber, T. Wild, and C. Grangeat, "A statistical approach for RF exposure compliance boundary assessment in massive MIMO systems", 22nd International ITG Workshop on Smart Antennas, March 2018
- [7] International Electrotechnical Commission, IEC 62232:2022 "Determination of RF field strength, power density and SAR in the vicinity of base stations for the purpose of evaluating human exposure", October 2022
- [8] International Electrotechnical Commission, "IEC TR 62669:2019 Case studies supporting IEC 62232 Determination of RF field strength, power density and SAR in the vicinity of radiocommunication base stations for the purpose of evaluating human exposure", Edition 2.0, April 2019
- [9] T. L. Marzetta, "Massive MIMO: An Introduction", Bell Labs Technical Journal, vol. 20, pp. 11-22, 2015
- [10] T. L. Marzetta, "Noncooperative Cellular Wireless with Unlimited Numbers of Base Station Antennas", IEEE Transactions on Wireless Communications, vol. 9, no. 11, pp. 3590-3600, November 2010
- [11] EMF Policy, GSMA: <a href="https://www.gsma.com/solutions-and-impact/connectivity-for-good/public-policy/regulatory-environment/emf-and-health/emf-policy/">https://www.gsma.com/solutions-and-impact/connectivity-for-good/public-policy/</a>
- [12] International Commission on Non-Ionizing Radiation Protection, "Guidelines for limiting exposure to electromagnetic fields (100 kHz to 300 GHz)", Health Phys., vol. 118, no. 5, March 2020, pp. 483–524
- [13] International Electrotechnical Commission, IEC 62232:2022 "Determination of RF field strength, power density and SAR in the vicinity of base stations for the purpose of evaluating human exposure", October 2022
- [14] International Electrotechnical Commission, "IEC TR 62669:2025 Case studies supporting IEC 62232 Determination of RF field strength, power density and SAR in the vicinity of radiocommunication base stations for the purpose of evaluating human exposure", Edition 3.0, 2025
- [15] International Electrotechnical Commission, IEC 62232:2025 "Determination of RF field strength, power density and SAR in the vicinity of base stations for the purpose of evaluating human exposure", March 2025
- [16] International Electrotechnical Commission, IEC 62232:2017 "Determination of RF field strength, power density and SAR in the vicinity of base stations for the purpose of evaluating human exposure", August 2017
- [17] Bo Xu at al. "A Summary of Actual Maximum Approach Studies on EMF Compliance of 5G Radio Base Stations", 16th European Conference on Antennas and Propagation EuCAP, March 2022
- [18] K. I. Pedersen et al., "A Tutorial on Radio System-Level Simulations with Emphasis on 3GPP 5G-Advanced and Beyond", IEEE Communications Surveys & Tutorials, vol. 26, no. 4, pp. 2290-2325, 2024
- [19] 3GPP Radio Access Network Working Group, "Study on Channel Model for Frequencies from 0.5 to 100 GHz (Release 15)", 3GPP TR 38.901 V15.1.0.
- [20] B. Thors, A. Furuskar, D. Colombi, and C. Tornevik, "Time-averaged realistic maximum power levels for the assessment of radio frequency exposure for 5G radio base stations using massive MIMO", IEEE Access, vol. 5, pp. 19711-19719, September 2017

- [21] S. Shikhantsov, A. Thielens, S. Aerts, L. Verloock, G. Torfs, L. Martens, P. Demeester and W. Joseph "Ray Tracing-Based Numerical Assessment of the Spatiotemporal Duty Cycle of 5G Massive MIMO in an Outdoor Urban Environment", MDPI Applied Science, October 2020
- [22] B. Mondal *et al.*, "3D channel model in 3GPP", IEEE Communications Magazine, vol. 53, no. 3, pp. 16-23, March 2015
- [23] B. Xu, D. Colombi, C. Törnevik, F. Ghasemifard and J. Chen, "On Actual Maximum Exposure From 5G Multicolumn Radio Base Station Antennas for Electromagnetic Field Compliance Assessment", IEEE Transactions on Electromagnetic Compatibility, vol. 63, no. 5, pp. 1680-1689, Oct. 2021
- [24] Differences between the ICNIRP (2020) and previous guidelines, https://www.icnirp.org/en/differences.html
- [25] M. Rybakowski, K. Bechta, "Analiza Symulazyjna Rzeczywistej Ekspozycji na Promieniowanie Elektormagnetyczne od Systemow Wieloantenowych 5G", Krajowa Konferencja Radiokomunikacji, Radiofonii i Telewizji, Warszawa, 08.09.2022, published in Przeglad Telekomunikacyjny - Wiadomosci Telekomunikacyjne, numer 4, 2022
- [26] D. Pinchera, M. Migliore, and F. Schettino, "Compliance boundaries of 5G massive MIMO radio base stations: A statistical approach", IEEE Access, vol. 8, October 2020, pp. 182 787-182 800
- [27] K. Bechta, M. Rybakowski, J. Du "Impact of Effective Antenna Pattern on Millimeter Wave System Performance in Real Propagation Environment", 13th European Conference on Antennas and Propagation (EuCAP), April 2019
- [28] K. Bechta, J. Du, M. Rybakowski, "Rework the Radio Link Budget for 5G and Beyond", IEEE Access, vol. 8, pp. 211585 211594, 2020
- [29] Institute of Electrical and Electronics Engineers, "IEEE Standard for Safety Levels with Respect to Human Exposure to Electric, Magnetic, and Electromagnetic Fields, 0 Hz to 300 GHz", 2019
- [30] Bundesamt für Kommunikation BAKOM, "Elektrische Feldstärken im Wirkbereich adap-tiver und konventioneller Mobilfunkantennen", December 2022.
- [31] W. Joseph, "5G EMF emissions fall well within safety limits", 5G Technology World, January 2022.
- [32] C.R. Bhatt et al. "Micro-environmental personal radio-frequency electromagnetic field exposures in Melbourne: A longitudinal trend analysis", Elsevier, Environmental Research, Volume 251, Part 2, June 2024
- [33] A. Fernandes Veludo et al., "Exploring RF-EMF levels in Swiss microenvironments: An evaluation of environmental and auto-induced downlink and uplink exposure in the era of 5G", Environmental Research, Volume 266, 2025
- [34] P. De Giudici et al., "Radiofrequency exposure of people living near mobile-phone base stations in France", Environmental Research, Volume 194, 2021
- [35] M. Leeman, R. Wydeaeghe, J. van der Straeten, S. Goegebeur, G. Vermeeren and W. Joseph, "City-Scale Spatio-Temporal Modeling of 5G Downlink Exposure of Users and Non-Users by Ray-Tracing in a Real Urban Environment", IEEE Access, vol. 13, pp. 30894-30906, 2025
- [36] M. Rybakowski, K. Bechta, Ch. Grangeat, P. Kabacik, "Statistical Analysis of the Actual RF Exposure from Massive MIMO Base Stations Serving Moving User Equipment", IEEE Access, Volume 12, 2024
- [37] M. Rybakowski, K. Bechta, Ch. Grangeat, P. Kabacik, "Impact of Beamforming Algorithms on the Actual RF EMF Exposure From Massive MIMO Base Stations", IEEE Access, Volume 11, December 2023
- [38] GSMA "Spectrum Policy Trends 2023", February 2023
- [39] M. V. Katwe et al., "CmWave and Sub-THz: Key Radio Enablers and Complementary Spectrum for 6G", https://arxiv.org/abs/2406.18391, 2024
- [40] S. Kang et al., "Cellular Wireless Networks in the Upper Mid-Band", IEEE Open Journal of the Communications Society, vol. 5, pp. 2058-2075, 2024
- [41] Nokia White Paper, "Coverage evaluation of 7–15 GHz bands from existing sites", 2024
- [42] H. Holma, H. Viswanathan and P. Mogensen, "Extreme massive MIMO for macro cell capacity boost in 5G-Advanced and 6G", Nokia White Paper, 2023

- [43] E. Björnson et al., "Enabling 6G Performance in the Upper Mid-Band by Transitioning From Massive to Gigantic MIMO", https://arxiv.org/abs/2407.05630, 2024
- [44] H. Holma, H. Viswanathan, P. Mogensen "Extreme massive MIMO for macro cell capacity boost in 5G-Advanced and 6G", Nokia Bell Labs White Paper, 2023
- [45] M. Rybakowski, K. Bechta, Ch. Grangeat, P. Kabacik, "Evaluation of the Actual EMF Exposure from Extreme Massive MIMO Base Stations around 10 GHz using Channel Modelling", 25th International Microwave and Radar Conference, 1-4 July 2024, Wroclaw
- [46] B. Xu et al., "Directional Power Control of 5G Radio Base Stations for EMF Compliance Part I: Design Principles and Feature Validation" IEEE Transactions on Antennas and Propagation, Early Access, 2024
- [47] F. Michler, R. Reese, B. Scheiner, E. Radermacher, J. A. G. Correal and B. Xu, "Directional Power Control of 5G Radio Base Stations for EMF Compliance Part II: Comparisons with Cell-Wide Power Control in a Live Network in Germany", IEEE Transactions on Antennas and Propagation, Early Access, 2024
- [48] S. Mandelli, L. Maggi, B. Zheng, A. Zejnilagic and C. Grangeat, "EMF Exposure Mitigation via MAC Scheduling" IEEE 25th International Workshop on Signal Processing Advances in Wireless Communications (SPAWC), Lucca, Italy, 2024
- [49] C. Tornevik, T. Wigren, S. Guo, and K. Huisman, "Time averaged power control of a 4G or a 5G radio base station for RF EMF compliance", IEEE Access, vol. 8, pp. 211 937–211 950, 2020
- [50] L. Maggi, A. Herzog, A. Zejnilagic and C. Grangeat, "Smooth Actual EIRP Control for EMF Compliance With Minimum Traffic Guarantee,", IEEE Wireless Communications Letters, vol. 13, no. 10, pp. 2817-2821, October 2024
- [51] M. Kohli et al., "Outdoor-to-Indoor 28 GHz Wireless Measurements in Manhattan: Path Loss, Environmental Effects, and 90% Coverage", IEEE/ACM Transactions on Networking, vol. 32, no. 3, pp. 2463-2478, June 2024
- [52] D. Shakya et al. "Urban Outdoor Propagation Measurements and Channel Models at 6.75 GHz FR1(C) and 16.95 GHz FR3 Upper Mid-Band Spectrum for 5G and 6G", (submitted) IEEE International Conference on Communications (ICC), Montreal, Canada, https://arxiv.org/abs/2410.17539, 2025
- [53] J. Du, M. Rybakowski, K. Bechta, R. A. Valenzuela, "Matching in the Air: Optimal Analog Beamforming under Angular Spread", https://arxiv.org/abs/1910.11054, 2019
- [54] D. Chizhik et al., "Directional Measurements and Propagation Models at 28 GHz for Reliable Factory Coverage", IEEE Transactions on Antennas and Propagation, vol. 70, no. 10, pp. 9596-9606, Oct. 2022
- [55] L. J. Greenstein and V. Erceg, "Gain reductions due to scatter on wireless paths with directional antennas," Gateway to 21st Century Communications Village. VTC 1999-Fall. IEEE VTS 50th Vehicular Technology Conference (Cat. No.99CH36324), Amsterdam, Netherlands, 1999, pp. 87-91 vol.1
- [56] R. M. Dreifuerst and R. W. Heath, "*Massive MIMO in 5G: How Beamforming, Codebooks, and Feedback Enable Larger Arrays*", IEEE Communications Magazine, vol. 61, no. 12, pp. 18-23, December 2023
- [57] W. Chen, X. Lin, J. Lee, A. Toskala, S. Sun, C. F. Chiasserini, L. Liu, "5G-Advanced Toward 6G: Past, Present, and Future", IEEE Journal on Selected Areas in Communications, Vol. 41, No. 6, June 2023
- [58] Patsouras, Ioannis et al, "Beyond 5G/6G EMF Considerations", 5G PPP Test, Measurement and KPIs Validation Working Group, EMF Task Force, 14/07/2023
- [59] H. Li, J. Xu, C. Sun, S. Wang, X. Wang and H. Zhang, "Integrated Sensing and Communication: 3GPP Standardization Progress" 21st International Symposium on Modeling and Optimization in Mobile, Ad Hoc, and Wireless Networks (WiOpt), Singapore, Singapore, 2023
- [60] E. Björnson, Ö. T. Demir and L. Sanguinetti, "A Primer on Near-Field Beamforming for Arrays and Reconfigurable Intelligent Surfaces", 55th Asilomar Conference on Signals, Systems, and Computers, Pacific Grove, CA, USA, 2021
- [61] N. Awarkeh, D. -T. Phan-Huy and R. Visoz, "Electro-Magnetic Field (EMF) aware beamforming assisted by Reconfigurable Intelligent Surfaces", IEEE 22nd International Workshop on Signal Processing Advances in Wireless Communications (SPAWC), Lucca, Italy, 2021, pp. 541-545

- [62] N. Awarkeh, D. -T. Phan-Huy and M. D. Renzo, "A Novel RIS-Aided EMF Exposure Aware Approach using an Angularly Equalized Virtual Propagation Channel", Joint European Conference on Networks and Communications & 6G Summit (EuCNC/6G Summit), Grenoble, France, 2022
- [63] H. Guo, D. -T. Phan-Huy and T. Svensson, "Electromagnetic Field Exposure Avoidance thanks to Non-Intended User Equipment and RIS", IEEE Globecom Workshops, Rio de Janeiro, Brazil, 2022
- [64] Parisa Ramezani, Emil Björnson, "Near-Field Beamforming and Multiplexing Using Extremely Large Aperture Arrays", Fundamentals of 6G Communications and Networking, X. Lin, J. Zhang, Y. Liu, J. Kim (eds), Chapter 12, pp. 317-349, 2023
- [65] Joshi, P.; Colombi, D; Xu, B.; Di Paola, C.; Eilers Bischoff, J; Zhekov, S. and Törnevik, C., "Long-term network-based assessment of the actual output power of base stations in a 5G network", 18th European Conference on Antennas and Propagation (EuCAP), 2024
- [66] E. Björnson, Ö. T. Demir and L. Sanguinetti, "A Primer on Near-Field Beamforming for Arrays and Reconfigurable Intelligent Surfaces", 55th Asilomar Conference on Signals, Systems, and Computers, Pacific Grove, CA, USA, 2021
- [67] K. Bechta, C. Grangeat, J. Du, M. Rybakowski, "Analysis of 5G Base Station RF EMF Exposure Evaluation Methods in Scattering Environments", IEEE Access, vol. 10, pp. 7196-7206, January 2022
- [68] R. Werner, P. Knipe; S. Iskra., "A comparison between measured and computed assessments of the RF exposure compliance boundary of an in-situ radio base station massive MIMO antenna", IEEE Access 2019, 7, 170682-170689
- [69] P. Bienkowski, B. Zubrzak, P. Sobkiewicz, K. Bechta and M. Rybakowski, "Simplified Methodology of Electromagnetic Field Measurements in the Vicinity of 5G Massive MIMO Base Station for Environmental Exposure Assessment", IEEE Access, vol. 12, pp. 8071-8080, 2024
- [70] E. Björnson, Y. C. Eldar, E. G. Larsson, A. Lozano and H. V. Poor, "Twenty-Five Years of Signal Processing Advances for Multiantenna Communications: From theory to mainstream technology", IEEE Signal Processing Magazine, vol. 40, 2023
- [71] P. Bienkowski, M. Rybakowski, "Nowoczesne systemy radiokomunikacyjne 5G z antenami wielowiazkowymi", XIII Krajowe Warsztaty Kompatybilności Elektromagnetycznej EMC 2022, Politechnika Wrocławska, Wrocław, 28.06.2022
- [72] M. Rybakowski "Walidacja funkcji monitorowania i kontroli EIRP dla systemów Massive MIMO zgodnie z IEC62232", XIV Krajowe Warsztaty Kompatybilności Elektromagnetycznej EMC 2024, Politechnika Wrocławska, Wrocław 27.06.2024
- [73] C. D. Paola et al., "Network-Based Assessment of Actual EIRP of 5G Base Stations in a Stadium With 100 000 People and Implications on EMF Compliance", IEEE Antennas and Wireless Propagation Letters, vol. 24, no. 1, pp. 242-246, Jan. 2025
- [74] A. -M. Schiffarth, T. T. Julian Ta, L. -M. Schilling, C. Bornkessel, M. Hein and D. Heberling, "Characterization of Typical Instantaneous Exposure and Usage Scenarios in the Vicinity of 5G Massive-MIMO Base Stations", 18th European Conference on Antennas and Propagation (EuCAP), Glasgow, United Kingdom, 2024
- [75] C. Bornkessel, A. Pikushina, L. -M. Schilling, T. Struck and M. A. Hein, "Reproducibility Studies of Instantaneous and 6-Minute Average Exposure Measurements Around 5G Massive-MIMO Base Stations", 18th European Conference on Antennas and Propagation (EuCAP), Glasgow, United Kingdom, 2024
- [76] A. Villaescusa-Tebar, A. Najera, J. Gonzalez-Rubio and C. Garcia-Pardo, "Instantaneous vs Theoretical Maximum Exposure Under Real Traffic Conditions: Example in the City of Valencia", 18th European Conference on Antennas and Propagation (EuCAP), Glasgow, United Kingdom, 2024
- [77] C. Davide et al. "Implications of ICNIRP 2020 Exposure Guidelines on the RF EMF Compliance Boundary of Base Stations", Frontiers in Communications and Networks, Volume 3, 2022
- [78] F. Héliot, T. H. Loh, D. Cheadle, Y. Gui and M. Dieudonne, "An Empirical Study of the Stochastic Nature of Electromagnetic Field Exposure in Massive MIMO Systems", IEEE Access, vol. 10, pp. 63100-63112, 2022

- [79] S. Aerts et al., "In Situ Assessment of 5G NR Massive MIMO Base Station Exposure in a Commercial Network in Bern, Switzerland", MDPI Appl. Sci. 2021, 11, 3592
- [80] B. Thors, D. Colombi, Z. Ying, T. Bolin and C. Törnevik, "Exposure to RF EMF From Array Antennas in 5G Mobile Communication Equipment", IEEE Access, vol. 4, pp. 7469-7478, 2016
- [81] A. Hirata et al., "Assessment of Human Exposure to Electromagnetic Fields: Review and Future Directions", IEEE Transactions on Electromagnetic Compatibility, vol. 63, no. 5, pp. 1619-1630, Oct. 2021
- [82] E. Degirmenci, B. Thors and C. Törnevik, "Assessment of Compliance with RF EMF Exposure Limits: Approximate Methods for Radio Base Station Products Utilizing Array Antennas With Beam-Forming Capabilities", IEEE Transactions on Electromagnetic Compatibility, vol. 58, no. 4
- [83] X. Bo et al. "A Monte Carlo Analysis of Actual Maximum Exposure From a 5G Millimeter-Wave Base Station Antenna for EMF Compliance Assessments", Frontiers in Public Health, Volume 9, 2022
- [84] M. D. Migliore and F. Schettino, "Power Reduction Estimation of 5G Active Antenna Systems for Human Exposure Assessment in Realistic Scenarios", IEEE Access, vol. 8
- [85] T. Jiang and A. K. Skrivervik, "Assessment of the Electromagnetic Field Exposure due to 5G Base Stations using a Monte-Carlo Method: Initial Results", 15th European Conference on Antennas and Propagation (EuCAP), Dusseldorf, Germany, 2021
- [86] Y. S. Lee, S. B. Jeon, A. -K. Lee, K. Kim, J. -K. Pack and H. -D. Choi, "Study on the Appropriate Measurement Spacing for EMF Installation Compliance Assessments of a 3.5 GHz 5G Base Station", IEEE Access, vol. 9, pp. 88167-88176, 2021
- [87] R. Werner, P. Knipe and S. Iskra, "A Comparison Between Measured and Computed Assessments of the RF Exposure Compliance Boundary of an In-Situ Radio Base Station Massive MIMO Antenna", IEEE Access, vol. 7, pp. 170682-170689, 2019
- [88] D. Colombi, P. Joshi, B. Xu, F. Ghasemifard, V. Narasaraju, C, Törnevik., "Analysis of the Actual Power and EMF Exposure from Base Stations in a Commercial 5G Network", Applied Sciences, 2020
- [89] B. Xu et al., "A Directional Power Monitoring and Control Feature for EMF Product Compliance of Base Stations", IEEE International Symposium on Antennas and Propagation and INC/USNC-URSI Radio Science Meeting (AP-S/INC-USNC-URSI), Firenze, Italy, 2024
- [90] M. Rybakowski, K. Bechta, Ch. Grangeat, A. Zejnilagic, P. Kabacik, "Optimization of Actual EIRP Control for Massive MIMO Base Stations Leveraging Beam Broadening and Angular Spread", submitted to EuCNC (European Conference on Networks and Communications) and 6G Summit, Poznan planned for 3-6 June 2025
- [91] Y. Khorsandmanesh, E. Björnson, J. Jaldén and B. Lindoff, "Beam Coherence Time Analysis for Mobile Wideband mmWave Point-to-Point MIMO Channels", IEEE Wireless Communications Letters, vol. 13, no. 6, pp. 1546-1550, June 2024
- [92] S. Adda et al., "A Methodology to Characterize Power Control Systems for Limiting Exposure to Electromagnetic Fields Generated by Massive MIMO Antennas", IEEE Access, vol. 8
- [93] D. Shakya, D. Chizhik, J. Du, R. A. Valenzuela and T. S. Rappaport, "Dense Urban Outdoor-Indoor Coverage from 3.5 to 28 GHz" ICC 2022 - IEEE International Conference on Communications, Seoul, Korea, Republic of, 2022
- [94] J. Du et al., "Directional Measurements in Urban Street Canyons From Macro Rooftop Sites at 28 GHz for 90% Outdoor Coverage", IEEE Transactions on Antennas and Propagation, vol. 69, no. 6, pp. 3459-3469, June 2021
- [95] J. Du, D. Chizhik and R. A. Valenzuela, "Minimum Per-Element Power of Phased Array for Gbps Mobile Access in mmWaves", IEEE Global Communications Conference (GLOBECOM), Waikoloa, HI, USA, 201